ABSTRACT

Title of Thesis: GENETICS, AGES, AND CHEMICAL COMPOSITIONS OF THE GROUP IIIE IRON METEORITES AND THE IRON METEORITE LIEKSA

Emily M. Chiappe, Master of Science, 2022

Thesis directed by: Professor Richard J. Walker, Department of Geology

Siderophile element concentrations, genetic isotopic data, and chronological data for ten group IIIE iron meteorites and the recently found iron meteorite Lieksa were determined. The modeling of siderophile element abundances shows that the IIIE irons can be related to one another through a common fractional crystallization process. Highly siderophile element data, however, indicate that the anomalous IIIE iron meteorite Aletai does not sample the same crystallization sequence as the bona fide IIIE irons. The bulk chemical characteristics of Lieksa are distinct from that of the established iron meteorite groups, indicating that, if it is an iron meteorite, it should be classified as an ungrouped iron meteorite. Isotopic data shows that, while the IIIE iron meteorites, Lieksa, and Aletai exhibit different HSE abundances, they exhibit similar genetic characteristics, indicating that they likely originated from the same nebular reservoir. Additionally, isotopic data indicate that all irons analyzed here sample parent bodies that differentiated within the first ~2 Myr of solar system history, which is consistent with other NC-type bodies.

GENETICS, AGES, AND CHEMICAL COMPOSITIONS OF GROUP IIIE IRON METEORITES AND THE UNGROUPED IRON LIEKSA

by

Emily M. Chiappe

Thesis submitted to the Faculty of the Graduate School of the
University of Maryland, College Park, in partial fulfillment
of the requirements for the degree of
Master of Science
2022

Advisory Committee:

Professor Richard J. Walker, Chair
Research Scientist Richard D. Ash
Associate Professor Ricardo Arévalo, Jr.

Table of Contents

List of Tables

List of Figures

Chapter 1: Introduction and Research Goals

1.1 Iron Meteorite Classification

Iron meteorites are characterized by high concentrations of iron and nickel and typically contain little to no silicate. Iron meteorites fall into one of two broad categories, magmatic and nonmagmatic, depending on the processes believed to be involved in their formation. Magmatic iron meteorites are commonly inferred to represent remnants of asteroidal cores, forming via parent body differentiation, then crystal-liquid fractionation of their respective cores, a process fueled primarily by the decay of the now extinct ^{26}Al. Nonmagmatic iron meteorites represent a more complex crystallization history, and have been suggested to form from processes other than simple crystal-liquid fractionation of a parent melt, such as from the crystallization of impact-induced melt pockets on undifferentiated, chondritic precursors (Wasson et al., 1980; Choi et al., 1995; Wasson and Kallemeyn, 2002). These contrasting formation histories lead to more varied chemical compositions among nonmagmatic iron meteorite groups when compared to magmatic iron groups.

Magmatic and nonmagmatic iron meteorite groups are further divided into subcategories I-IV based on their volatile siderophile element concentrations (e.g., Ga and Ge), with group IV iron meteorites being the most depleted in volatile siderophile elements relative to refractory siderophile elements (e.g., W, Mo, Ni), and group I irons being the least depleted (Lovering et al., 1957; Scott and Wasson, 1975). These categories have been further divided into lettered groups based on observed chemical similarities among irons, leading to the present recognition of eleven magmatic iron meteorite groups, with each

corresponding to an individual parent body. The major magmatic iron meteorite groups are: IC, IIAB, IIC, IID, IIF, IIG, IIIAB, IIIE, IIIF, IVA, and IVB. Iron meteorite groups are commonly characterized based on their highly siderophile element concentrations. Highly siderophile elements (HSE), which are comprised of Re and Au, along with the platinum group elements Ru, Rh, Pd, Os, Ir, and Pt, have extremely high metal-silicate partition coefficients ($>10^4$), although these vary with pressure, temperature, and fO_2 (Walker, 2016). Because of their tendency to partition into metal and their somewhat predictable behavior during crystal-liquid fractionation of metal, HSE prove useful in the study of iron meteorites and can provide insight into the processes involved in a group's formation history.

Additionally, over 100 iron meteorites are currently classified as "ungrouped" due to their lack of shared chemical characteristics with any of the established groups. These ungrouped irons likely sample numerous parent bodies that remain poorly characterized. Thus, better defining the chemical, genetic, and chronological characteristics of ungrouped iron meteorites will aid in understanding the full genetic and chemical composition of the protoplanetary disk.

1.2 Meteorite Genetics

The various isotopes present in the solar system were produced via a variety of nucleosynthetic processes, including the *s*-, *r*-, and *p*-processes, or slow neutron capture, rapid neutron capture, and photodisintegration/proton capture, respectively (Burbidge et al., 1957). All meteorites, including iron meteorites, can be further classified using a set of "genetic" isotopes that have revealed a heterogenous distribution of nucleosynthetic

components throughout the protoplanetary disk. Some of these heterogeneities are characterized by mass independent variations in the isotopic compositions of extraterrestrial materials (Dauphas and Schauble, 2016). These anomalies have been observed across a number of elements and have provided insight into the distribution and mixing of presolar materials in the protoplanetary disk (e.g., Trinquier et al., 2007; Regelous et al., 2008; Warren, 2011; Burkhardt et al., 2011; Bermingham et al., 2016; Worsham et al., 2019). These observations have revealed at least two isotopically distinct regions in the solar nebula and have led to the establishment of the carbonaceous chondrite (CC) and non-carbonaceous (NC) meteorite classification by Warren (2011), based on previously reported differences in the Cr, Ti, and O isotopic compositions of various meteorites.

Isotopic compositions of the siderophile elements Mo, Ru, and W have proven particularly useful in assessing iron meteorite parent body genetics. Molybdenum, for example, has seven stable isotopes produced through varying contributions of the *s*-, *r*-, and *p*-processes, making isotopic compositions of this element useful in tracing nucleosynthetic components within the protoplanetary disk (e.g., Dauphas et al., 2002, Burkhardt et al., 2011, Budde et al., 2016). Carbonaceous chondrite-type meteorites have been shown to display an enrichment in nuclides produced through *r*-process (such as ^{95}Mo) when compared to NC-type material, and both groups show variable *s*- and *p*-process heterogeneity (Kruijer et al., 2017; Worsham et al., 2019). Heterogeneities such as these, thus, allow for characterization of the two distinct nebular domains through the study of iron meteorites and other metal-rich meteorites.

1.3 Iron Meteorite Chronology

1.3.1 Re-Os Chronology

Multiple long- and short-lived chronometers have been employed to constrain the timescales of various early solar system processes, such as planetary accretion, core formation, and mantle differentiation (Kleine and Rudge, 2011). The ^{187}Re-^{187}Os ($t_{1/2}$ = 41.6 Gyr) chronometer allows for broad temporal constraints to be placed on core crystallization of an iron meteorite parent body. This system is also used to assess the closed-system behavior of siderophile elements (e.g., Smoliar et al., 1996; Shen et al., 1996; Walker et al., 2008). This is done by plotting Re-Os isotopic compositions for an iron meteorite group and comparing to a primordial reference isochron. Data plotting significantly off of the isochron are presumed to reflect some degree of open-system behavior.

1.3.2 Hf-W Chronology and Metal-Silicate Segregation

The ^{182}Hf-^{182}W ($t_{1/2}$ = 8.9 Myr; Vockenhuber et al., 2004) chronometer is commonly applied to iron meteorites as a means of assessing the core formation history of a parent body. Application of the system is based on the lithophile nature of Hf and the siderophile nature of W. Because of their respective partitioning behaviors, Hf remains in the silicate portion of a differentiated parent body, while W partitions primarily into the metallic core. The ^{182}W composition recorded in iron meteorites, therefore, reflects the ^{182}W composition at the time of metal-silicate segregation, as no more ^{182}W can be

produced in the core due to the absence of ^{182}Hf. Measured ^{182}W compositions can then be used to determine a model core formation age using the following equation:

$$\Delta T_{CAI} = -\frac{1}{\lambda} \ln \left[\frac{(\mu^{182}W)_{sample} - (\mu^{182}W)_{chondrite}}{(\mu^{182}W)_{CAI} - (\mu^{182}W)_{chondrite}}\right] \quad \text{(Eq. 1.1)}$$

where λ is the ^{182}Hf decay constant of 0.078 ± 0.002 Myr^{-1} (Vockenhuber et al., 2004). The μ notation represents the deviation in parts per million of an isotopic ratio, in this case ^{182}W/^{184}W, from a laboratory standard. The present-day chondritic μ^{182}W value, based on an assumption of a carbonaceous chondrite-like precursor composition, is assumed to be -191 ± 8 (Kleine et al., 2004). This provides a model metal-silicate segregation age relative to calcium-aluminum-rich inclusions (CAI), which record the initial solar system μ^{182}W value of -349 ± 7 (Kruijer et al., 2014). Variable μ^{182}W compositions have been observed in NC and CC iron meteorites, reflecting different timescales of metal-silicate segregation (Kruijer et al., 2017).

1.4 Research Goals

Most major magmatic iron meteorite groups have been assessed in regard to their siderophile element concentrations, crystallization sequences, projected parental melt compositions, and genetic isotopic compositions (e.g. Scott and Wasson, 1973; Pernicka and Wasson, 1987; Dauphas et al., 2002; Walker et al., 2008; McCoy et al., 2011). One goal of this research is to similarly chemically and genetically characterize the group IIIE iron meteorites, a magmatic iron group that currently consists of sixteen individual irons (*Meteoritical Bulletin*, 2022). The group is characterized by moderate depletions in volatile

siderophile elements, and members of the group are structurally classified as coarse octahedrites (Scott and Wasson, 1973). They are chemically similar to the much larger IIIAB group in terms of Ni, Ga, and Ge concentrations, but are distinguished based their coarser kamacite bandwidths, as the IIIAB irons are structurally classified as medium octahedrites, thus having slightly smaller kamacite bands than the IIIE irons. The IIIE irons also contain the C-rich minerals haxonite ($[Fe, Ni]_{23}C_6$) and graphite, which are not found in the group IIIAB irons (Scott and Wasson, 1973). Previous isotopic investigation into the group IIIE iron meteorites has shown them to be NC-type meteorites (Kruijer et al., 2017; Worsham et al., 2019). The group also displays evidence of alteration due to shock-induced heating in the form of melted troilite, the decomposition of haxonite to graphite, and recrystallized kamacite, possibly indicating one or more major impacts to the group IIIE parent body (Breen et al., 2016).

Chemical modeling has not previously been attempted for the group IIIE iron meteorites. While some prior isotopic investigations have been conducted on the IIIE irons, this work expands on them through the analysis of additional meteorites from the group, including the anomalous IIIE iron, Aletai. It has been noted, based on W isotopic compositions, that the IIIE parent body, along with most other iron meteorite parent bodies, differentiated within the first few million years of solar system history, meaning that additional compositional constraints placed on the IIIE parent body core will provide further insight into the chemical composition of the early solar system (Kruijer et al., 2017).

An additional goal of this work is to characterize the ungrouped iron meteorite Lieksa. Found in 2017, the meteorite has yet to be thoroughly analyzed, and as such, has not been classified. An appropriate classification will be proposed through assessment of

Lieksa's siderophile element concentrations and nucleosynthetic isotope compositions. Gaining insight into the chemical, genetic, and chronological characteristics of Lieksa, as well as of the group IIIE irons, will advance understanding of the structure, composition, and evolution of the protoplanetary disk.

Chapter 2: Age, Genetics, and Crystallization Sequence of the Group IIIE Iron Meteorites

2.1 Abstract

Highly siderophile element (HSE) concentrations were obtained for ten iron meteorites that are currently classified as IIIE irons. Molybdenum, Ru, and W isotopic data were also collected to assess nucleosynthetic, mass-independent isotopic anomalies, as well as the timescale of differentiation of the IIIE parent body. Highly siderophile element concentrations indicate that the anomalous IIIE iron, Aletai, does not sample the same crystallization sequence as the other irons analyzed here. The remaining nine irons exhibit broadly similar bulk chemical characteristics, and can be related to one another through fractional crystallization of a parental melt with initial S, P, and C concentrations of 12 wt.%, 1.8 wt.%, and 0.15 wt.%, respectively. The modeled parental melt composition is ~4 times more enriched in HSE than a non-carbonaceous (NC) chondrite-like parent body, suggesting a core size of ~22% of the mass of the body. Cosmic ray exposure-corrected nucleosynthetic Mo, Ru, and W isotopic compositions of the IIIE irons and Aletai indicate that they originated from the NC isotopic domain within the solar nebula. Tungsten-182 isotopic data for the IIIE irons and Aletai yield model metal-silicate segregation ages of 1.6 ± 0.8 Myr and 1.2 ± 0.8 Myr after calcium aluminum-rich inclusion (CAI) formation, respectively. These ages are consistent with those of all other NC-type iron meteorite parent bodies.

2.2 Introduction

Magmatic iron meteorites are interpreted to be fragments of asteroidal cores, with members within each group related through solid metal-liquid metal fractionation processes (e.g., Scott, 1972). The group IIIE meteorites comprise a magmatic iron group with sixteen currently recognized members. Two irons within the group, Aletai and Aliskerovo, are currently classified as anomalous, based on slight differences in siderophile element content (*Meteoritical Bulletin*, 2022). The IIIE irons are characterized by moderate depletions in the volatile siderophile elements (e.g., Ga and Ge) and are structurally classified as coarse octahedrites (Scott and Wasson, 1973; Scott and Wasson, 1975). The IIIE irons exhibit similar Ga, Ge, and Ni concentrations as the much larger group IIIAB irons, but are distinguished by their coarser kamacite bandwidths, as well as by the presence of the C-rich minerals haxonite ($[Fe, Ni]_{23}C_6$) and graphite, which are absent in the IIIAB irons (Scott and Wasson, 1973).

Magmatic iron meteorite groups can be further characterized through the utilization of so-called "genetic" isotopes, which have revealed nucleosynthetic isotope heterogeneity among bulk planetary materials, suggesting the presence of at least two isotopically distinct nebular domains. This dichotomy likely reflects the heterogeneous distribution of nucleosynthetic components throughout the protoplanetary disk, and therefore, heterogeneous accretion of material to parent bodies in each domain. This nucleosynthetic heterogeneity has been identified in meteorites across several elements, including Ti, Cr, Ni, Mo, W, and Ru (e.g., Trinquier et al., 2007; Trinquier et al., 2009; Warren, 2011; Fisher-Gödde et al., 2015; Budde et al., 2016; Kruijer et al., 2017), and has led to the recognition of the carbonaceous chondrite (CC) and non-carbonaceous (NC) meteorite

classification scheme (Warren, 2011). It has been suggested that these two domains were initially isolated from one another by the formation of proto-Jupiter, which has led to the interpretation of NC- and CC-type meteorites sampling the inner and outer solar system, respectively (Warren, 2011; Budde et al., 2016; Kruijer et al., 2017).

The siderophile nature of Mo, Ru, and W makes these elements especially useful in the study of nucleosynthetic variability recorded in iron meteorites. Most magmatic iron meteorite groups have been classified as NC (IC, IIAB, IIIAB, IIIE, IVA) or CC (IIC, IID, IIF, IIIF, IVB). Recent study into the Mo, W, and Ru compositions of the group IIIE irons has shown them to be NC-type meteorites (Kruijer et al., 2017; Worsham et al., 2019).

The ^{182}Hf-^{182}W system ($t_{1/2}$ = 8.9 Myr; Vockenhuber et al., 2004) is often applied to iron meteorites in the assessment of the thermal evolution, accretion age, and core formation age of their respective parent bodies (Kruijer et al., 2017; Tornabene et al., 2020). Variable ^{182}W isotopic compositions have been observed in NC and CC iron meteorites, reflecting different timescales of metal-silicate segregation and accretion. Non-carbonaceous type iron meteorite groups (IC, IIAB, IIIAB, IIIE, IVA) underwent core formation at ~0.3 to ~1.8 Myr after calcium aluminum rich inclusion (CAI) formation, while CC-type groups (IIC, IID, IIF, IIIF, IVB) segregated later in solar system history, from ~2.2 to ~2.8 Myr after CAI formation (Kruijer et al., 2017). However, recent work has indicated that NC and CC iron meteorite parent body precursor material may have evolved with variable Hf/W ratios, with ratios of NC bodies being slightly lower than that of CC bodies (Hellmann et al., 2019). This would suggest that model ages obtained using the Hf-W chronometer for NC bodies may be somewhat younger than previously thought, by up to ~0.7 Myr (Hellmann and Walker, 2022).

A meteorite's Mo, Ru, and W isotopic composition can be modified by neutron capture reactions triggered by cosmic ray exposure (CRE; Wittig et al., 2013; Kruijer et al, 2013). The degree to which an isotopic composition is altered is dependent on the duration of cosmic ray flux and the depth of a sample from the surface (Markowski et al., 2006). In order to obtain meaningful genetic data, these effects must be monitored and corrected for where necessary, ideally using the same meteorite piece used for genetic analysis. Here, Pt is utilized as a dosimeter, as $^{196}Pt/^{195}Pt$ ratios are sensitive to CRE effects and become increasingly positive with CRE flux (Kruijer et al., 2013; Worsham et al., 2019).

The object of this study is to utilize highly siderophile element concentrations to assess the possible relationship between ten group IIIE iron meteorites through crystal-liquid fractionation modeling, to assess Mo, Ru, and W genetic characteristics, and to further constrain the thermal history and timing of metal-silicate segregation of the IIIE parent body core.

2.3 Samples

Seven group IIIE iron meteorite samples were obtained from the Smithsonian Institution National Museum of Natural History: Coopertown (USNM 1003), Kokstad (USNM 488), Paloduro (USNM 6877), Rhine Villa (USNM 272), Staunton (USNM 2204), Tanokami Mountain (USNM 1456), and Willow Creek (USNM 900). Burlington (ASU 978) and Colonia Obrera (ASU 1032) were obtained from Arizona State University. Aletai was obtained from KD Meteorites, Kansas. This meteorite is currently classified as an anomalous IIIE iron due to its reportedly high Au and Ir concentrations relative to the other IIIE irons (Bouvier et al., 2017).

2.4 Analytical Methods

2.4.1 Laser Ablation Inductively Coupled Plasma Mass Spectrometry

Each sample was cut into a 100-200 mg piece using a water-cooled *Leco Vari-cut* saw equipped with a diamond sawblade. Cross-contamination between samples was avoided by cleaning the sawblade with water and replacing the cooling water after each cut. A piece of carborundum was also cut in between each sample to further clean the blade. Samples were then polished with sandpapers of various grit to ensure that flat surfaces were removed of blade markings and rust. Immediately prior to analysis, samples were ultrasonicated in ethanol to remove any additional contaminants. Concentrations of 18 siderophile elements (Re, Os, W, Ir, Mo, Ru, Pt, Rh, Ni, Co, Fe, Pd, Cr, P, As, Au, Ga, Ge) were obtained using a *New Wave UP213* ultraviolet laser coupled to a *Thermo Finnigan Element 2* inductively coupled mass spectrometer (ICP-MS). Data were processed using *LAMTRACE* (Rusk, 2009), using known concentrations of in-house laboratory reference iron meteorites Hoba, Coahuila, and Filomena. Iron concentrations were used as an internal standard using accepted concentrations from the literature (Buchwald, 1975). Multiple bulk ~5 mm long laser ablation tracks were averaged in order to obtain a representative composition of each sample.

2.4.2 ^{187}Re-^{187}Os and Highly Siderophile Element Analysis

Concentrations of Re, Os, Ir, Ru, Pt, and Pd, as well as ^{187}Re-^{187}Os data were obtained via isotope dilution of bulk samples, following the procedures outlined in Walker et al. (2008). The highly siderophile elements Rh and Au were not included in this analysis

due to their monoisotopic nature. Approximately 70-250 mg pieces of each sample were cut and polished. Each piece, along with appropriate amounts of a mixed spike containing ^{185}Re-^{190}Os and a separate mixed spike of ^{191}Ir-^{99}Ru-^{194}Pt-^{105}Pd was added to a *Pyrex*® Carius tube, along with 2.5 mL of concentrated HCl and 5 mL of concentrated HNO_3. Each tube was sealed and heated at ~220ºC for 24-48 hours to obtain complete dissolution and sample-spike equilibrium. This high temperature digestion oxidizes Os to a +8 valence, forming osmium tetroxide (OsO_4). After dissolution, Os was separated via the carbon tetrachloride (CCL_4) solvent extraction technique outline in Cohen and Waters (1996) and further purified by microdistillation as described in Birck et al. (1997). The purified Os was loaded onto a Pt filament with a Ba hydroxide activator and analyzed using a *Thermo Fisher Triton* thermal ionization mass spectrometer (TIMS). Osmium isotopic data were corrected for instrumental mass fractionation by normalizing ^{190}Os/^{188}Os to 3.08271 (Allègre and Luck, 1980).

The residual acid containing the remaining HSE was evaporated to dryness, and the residue redissolved in 1M HCl. This was repeated once more to ensure removal of any remaining HNO_3. The samples were then loaded onto anion exchange columns in 1M HCl (Rehkämper and Halliday, 1997). Rhenium and Ru were eluted with 12 mL of 6M HNO_3, Pt and Ir were eluted with 13 mL of concentrated HNO_3, and Pd was eluted with 14 mL of concentrated HCl. The Re and Ru aliquots were further purified using a secondary anion exchange column and eluted with 7 mL of 6M HNO_3. Rhenium, Ru, Ir, Pt, and Pd were analyzed using a *Thermo Fisher Neptune Plus* multi-collector ICP-MS. Tungsten was added to the Re aliquots to correct for mass fractionation effects. Blanks for these procedures (n = 3) average 3, 4, 4, 43, 33, and 40 pg for Re, Os, Ir, Ru, Pt, and Pd,

respectively. Blank corrections were made but had negligible impact on final concentrations. Estimated measurement uncertainties for Re and Os are < 0.1% and < 2% for the other HSE.

2.4.3 Molybdenum, Ru, W, and Pt Isotopic Measurements

Isotopic analyses of Mo, Ru, W, and Pt were achieved on approximately 2-5 g pieces of the samples. All isotopic compositions in this study will be reported using the μ notation (e.g., Mo):

$$\mu^{94}\mathrm{Mo} = \left(\frac{^{94}_{96}\mathrm{Mo}_{\mathrm{sample}}}{^{94}_{96}\mathrm{Mo}_{\mathrm{standard}}} - 1\right) * 10^6 \qquad \text{(Eq. 2.1)}$$

Each meteorite chunk was dissolved in 8M HCl at ~140º for at least 48 hours in *Teflon*® beakers. The resulting solution was separated into two aliquots to be processed separately. One aliquot was processed for Mo, W, and Pt using a scaled-up version of the anion exchange column procedure described by Nagai and Yokoyama (2014). Following this procedure, W was eluted with 100 mL of 9M HCl + 1M HF, Mo with 50 mL of 6M HNO_3 + 3M HF, and Pt with 75 mL of concentrated HNO_3.

After the initial primary column, the resulting Mo aliquots were dried, redissolved in 0.5 mL of 6M HCl, and loaded onto a secondary anion exchange column with ~0.3 mL AG 1 x 8 200-400 mesh resin, following the chemical separation techniques outlined in Worsham et al. (2016a). Molybdenum was then eluted with 12.5 mL of 1M HCl. This secondary column elution scheme was repeated once more to ensure sufficient purification. The Mo aliquots were dried, redissolved in a 2:1 mixture of concentrated HNO_3 and HCl (100 μL), and dried again. This was repeated two more times to ensure removal of any

resin-derived organics. Samples were then redissolved in 6M HCl. Approximately 1000 ng of Mo from each sample were loaded onto outgassed Re filaments along with 2 µL of a 5 µg/µL $La(NO_3)_3$ activator solution. Following the double filament assembly described in Worsham et al. (2016a), a second filament was also prepared for each sample with 2 µL of a 5 µg/µL $La(NO_3)_3$ activator. Molybdenum was analyzed as MoO^-_3 using a *Thermo Fisher Triton Plus* TIMS using a 3-peak jump, multi-dynamic method (Worsham et al., 2016a). Isotopic data were corrected for instrumental mass fractionation by normalizing $^{98}Mo/^{96}Mo$ to 1.453171 (Lu and Masuda, 1994). Analytical uncertainties were assessed by repeatedly measuring standards during the measurement campaign and determining their external reproducibility (2SD), which was ±36, ±12, ±8, ±4, and ±22 ppm for $\mu^{92}Mo$, $\mu^{94}Mo$, $\mu^{95}Mo$, $\mu^{97}Mo$, and $\mu^{100}Mo$, respectively (n = 10).

Tungsten aliquots from the initial primary column were dried, redissolved in 0.6 mL of 0.4M HCl + 0.5M HF, and loaded onto a secondary column with ~0.2 mL AG 1 x 8 200-400 mesh resin, following procedures outlined in Nagai and Yokoyama (2014). Tungsten was eluted with 2.4 mL of 9M HCl + 3M HF. This column procedure was repeated once more to ensure W separation. The purified W aliquots were dried and redissolved in 0.4M HCl + 0.5 M HF. Approximately 1000 ng of W from each sample was loaded onto an outgassed Re filament along with 1 µL of 5 µg/µL La- 5 µg/µL Gd activator solution and measured as WO^-_3 using a *Thermo Fisher Triton* TIMS. Isotopic data were corrected for instrumental mass fractionation by normalizing $^{186}W/^{184}W$ to 0.92767 (Völkening et al., 1991). The 2SD external precision for this analytical campaign, as defined by repeated analyses of the standard, was ± 6 ppm for $\mu^{182}W$ and ± 3 ppm for $\mu^{183}W$ (n = 5).

Platinum aliquots were dried, redissolved in a 2:1 mixture of concentrated HNO_3 and HCl, and refluxed overnight at 100ºC, following the clean-up procedure described in Hunt et al. (2017). Samples were then dried and refluxed overnight in 1M HCl, then diluted with ascorbic acid and loaded onto an anion exchange column with ~1 mL AG 1 x 8 200-400 mesh resin. Platinum was eluted with 15 mL of concentrated HNO_3. This column procedure was repeated once more to ensure complete Pt-Ir separation. Solutions were dried, treated with $HClO_4$, and refluxed overnight in 2:1 HNO_3 and HCl. Samples were dried once more and taken up in 5% HNO_3 to be analyzed on a *Thermo Fisher Neptune Plus* multi-collector ICP-MS. Isotopic data were corrected for instrumental mass fractionation by normalizing $^{198}Pt/^{195}Pt$ to 0.2145 (Kruijer et al., 2013). The 2SD external precision for this analytical campaign, as defined by repeated analyses of the standard, was ± 8 ppm for $\mu^{196}Pt$ (n = 20).

The second aliquot from the initial 8M HCl digestion was processed for Ru following methods outlined in Bermingham et al. (2016). Ruthenium aliquots were dried, redissolved in 0.15M HCl, and loaded onto a primary cation column with 10 mL AG50W8X 200-400 mesh resin, and eluted with 15 mL of 0.15M HCl. Ruthenium was further purified via microdistillation using 0.2 g/mL CrO_3 in 0.5M H_2SO_4 and 4M HBr. After microdistillation, samples were taken up in 5% HNO_3 and analyzed using a *Thermo Fisher Neptune Plus* multi-collector ICP-MS. Isotopic data were corrected for instrumental mass fractionation by normalizing $^{99}Ru/^{101}Ru$ to 0.745075 (Chen et al., 2010). The 2SD external precision for this analytical campaign, as defined by repeated analyses of the standard, was ± 8 ppm for $\mu^{100}Ru$ (n = 15).

2.5 Results

2.5.1 Bulk Composition by Laser Ablation ICP-MS

Bulk compositional data for the IIIE iron meteorites determined via laser ablation ICP-MS along with their two-standard deviation (2SD) for each element are given in Table 2.1. Rhenium concentrations were below detection limits for all samples except Kokstad, Colonia Obrera, and Aletai. Substantial variations in signal intensities along some measured tracks were observed for several elements (e.g., Cr and P) due to the intersection of the ablation tracks with non-metal phases, such as chromites and phosphides. Thus, the variations do not reflect heterogeneity in the metal phase itself. Nickel concentrations obtained here are within 15% of those reported by Scott and Wasson (1973). Gallium and Ge concentrations are within 10%, and Ir concentrations are within 20% of reported concentrations (Scott and Wasson, 1973).

Bulk siderophile element data, normalized to CI-chondrites, reveal broadly similar patterns for most of the IIIE irons (Fig. 2.1). The data show moderate depletions in the volatile siderophile elements (e.g., Ga and Ge) relative to the more refractory siderophile elements (e.g., Mo and W), consistent with their group III classification. The siderophile element abundance pattern for Aletai, however, deviates significantly from the patterns established by the other IIIE irons. This is noticeable, for example, in the higher Au and As contents and lower Ru and Pt contents exhibited by the iron. Thus, as discussed below, the composition of Aletai is inconsistent with it sampling the same crystal-liquid fractionation sequence as the bona fide IIIE irons, and is hereafter treated as separate from the group IIIE irons.

Table 2.1 Average siderophile element concentrations for the group IIIE irons determined by LA-ICP-MS.

	Coopertown	Kokstad	Staunton	Willow Creek	Burlington	Tanokami Mountain	Paloduro	Rhine Villa	Colonia Obrera	Aletai *(an.)*
Re	b.d.	0.05	b.d.	b.d.	b.d.	b.d.	b.d.	b.d.	0.005	0.05
Os	0.18 ± 0.02	0.16 ± 0.01	0.05 ± 0.04	0.01 ± 0.01	0.15 ± 0.04	0.061 ± 0.001	0.05 ± 0.01	0.04 ± 0.01	0.06 ± 0.03	0.26 ± 0.03
W	0.9 ± 0.1	0.9 ± 0.1	0.8 ± 0.2	0.6 ± 0.1	0.9 ± 0.3	1.1 ± 0.7	1.1 ± 0.8	0.6 ± 0.1	0.9 ± 0.8	0.5 ± 0.2
Ir	0.59 ± 0.08	0.56 ± 0.03	0.12 ± 0.04	0.05 ± 0.03	0.51 ± 0.04	0.22 ± 0.08	0.16 ± 0.18	0.11 ± 0.03	0.09 ± 0.04	0.26 ± 0.06
Mo	7.1 ± 0.1	6.1 ± 0.9	7.6 ± 1.2	7.2 ± 0.5	7.0 ± 0.5	10.3 ± 5.6	7.4 ± 1.6	6.0 ± 0.2	8.5 ± 3.0	7.2 ± 4.6
Ru	5.7 ± 1.6	5.7 ± 1.2	4.0 ± .03	3.1 ± 1.2	5.3 ± 1.3	6.4 ± 2.7	3.2 ± 2.4	3.6 ± 0.4	3.2 ± 0.9	1.5 ± 0.6
Pt	8.8 ± 0.6	8.8 ± 0.9	6.2 ± 0.3	5.0 ± 0.3	8.8 ± 0.4	8.5 ± 3.6	6.0 ± 0.8	5.8 ± 0.4	6.2 ± 2.1	2.5 ± 0.5
Rh	1.3 ± 0.2	1.2 ± 0.1	1.2 ± 0.1	1.1 ± 0.3	1.3 ± 0.1	1.8 ± 0.9	1.2 ± 0.4	1.2 ± 0.2	1.4 ± 0.2	0.9 ± 0.2
Ni	6.8 ± 2.1	4.4 ± 7.4	8.0 ± 1.3	8.3 ± 3.4	7.6 ± 0.6	3.7 ± 0.01	4.9 ± 4.8	5.1 ± 6.1	5.4 ± 2.3	6.2 ± 1.1
Co	0.52 ± 0.04	0.49 ± 0.01	0.51 ± 0.03	0.52 ± 0.06	0.51 ± 0.01	0.56 ± 0.17	0.49 ± 0.11	0.51 ± 0.03	0.50 ± 0.08	0.57 ± 0.05
Fe*	91.0	91.0	91.0	91.0	91.0	91.0	91.0	91.0	91.0	91.0
Pd	2.3 ± 0.8	2.4 ± 0.4	2.7 ± 0.2	2.9 ± 0.4	2.3 ± 0.2	3.9 ± 0.6	3.2 ± 2.1	2.5 ± 0.4	5.9 ± 5.9	5.5 ± 3.7
Cr	170.1 ± 191.6	64.5 ± 20.6	25.1 ± 17.0	30.9 ± 44.3	14.2 ± 3.0	28.7 ± 19.5	25.6 ± 6.8	15.2 ± 5.6	21.5 ± 20.2	37.2 ± 31.5
P	0.2 ± 0.1	0.2 ± 0.2	0.2 ± 0.2	0.31 ± 0.03	0.14 ± 0.04	0.17 ± 0.01	0.3 ± 0.2	0.1 ± 0.1	0.2 ± 0.1	0.2 ± 0.1
As	5.2 ± 1.8	4.8 ± 0.2	7.0 ± 1.3	8.9 ± 0.2	6.6 ± 0.7	8.1 ± 2.0	6.3 ± 2.7	6.5 ± 0.7	10.6 ± 2.5	19.4 ± 3.2
Au	0.5 ± 0.1	0.5 ± 0.1	0.7 ± 0.1	1.0 ± 0.3	0.8 ± 0.1	1.0 ± 0.1	1.0 ± 0.6	1.5 ± 2.8	1.1 ± 0.1	1.7 ± 0.8
Ga	17.3 ± 0.3	17.8 ± 1.3	19.3 ± 1.7	18.7 ± 2.9	17.9 ± 1.8	27.0 ± 4.9	19.9 ± 1.5	18.0 ± 1.2	26.2 ± 12.4	18.0 ± 1.5
Ge	35.4 ± 2.9	35.2 ± 1.4	39.6 ± 6.0	40.1 ± 0.9	37.3 ± 2.7	51.7 ± 16.8	37.4 ± 4.9	38.1 ± 0.7	42.9 ± 1.6	33.5 ± 1.6
n	3	3	3	2	2	2	3	3	4	4

Iron, Ni, Co, and P concentrations reported in wt %, all others reported in ppm. 2σ values are also reported.
n is number of lines measured for each sample.
b.d. below detection limits.
* Fe was used as an internal standard.

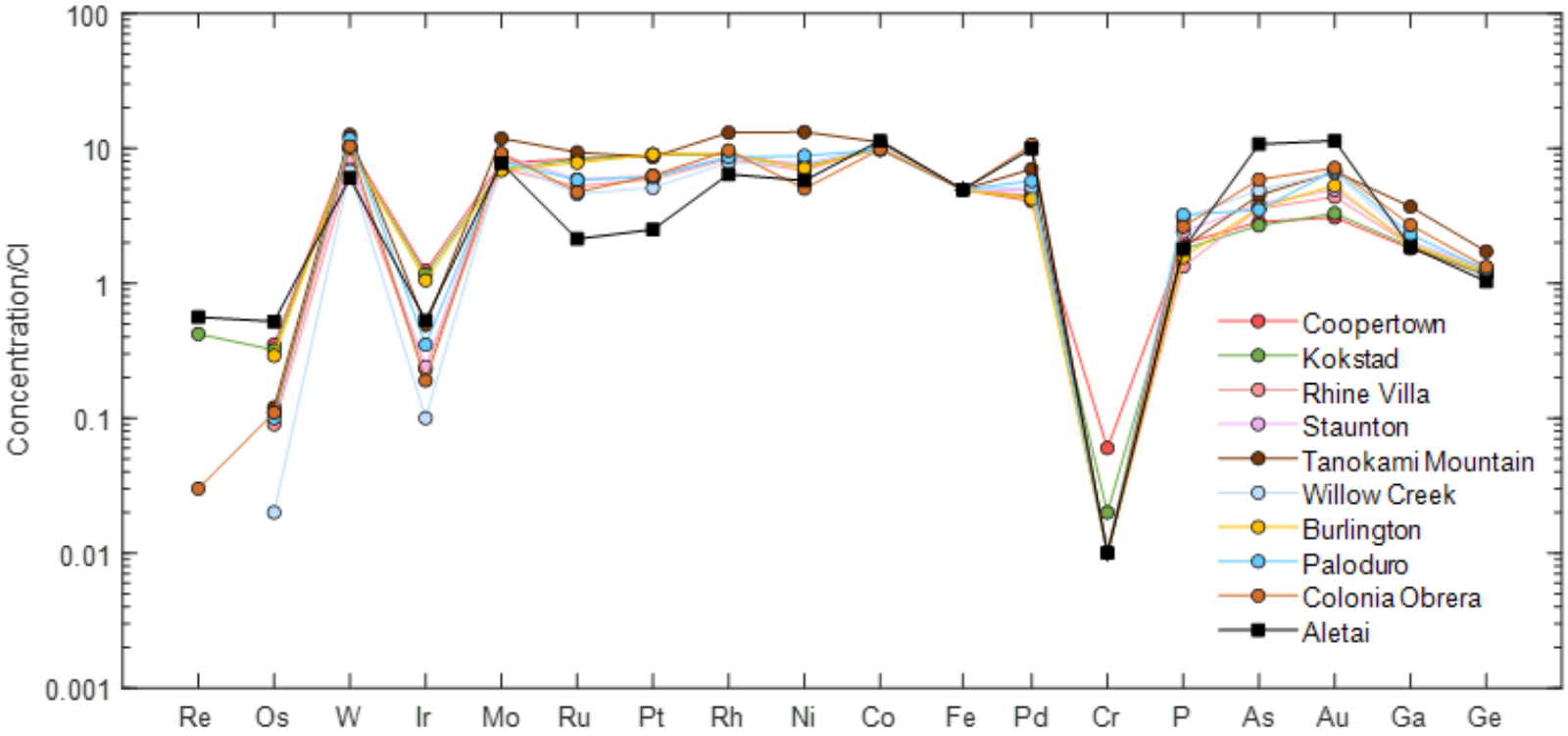

Figure 2.1 CI-chondrite normalized siderophile element abundances for nine group IIIE iron meteorites and Aletai obtained via laser ablation ICP-MS. Normalizing data are from Lodders (2003). Elements are listed in order of decreasing 50% condensation temperature from left to right.

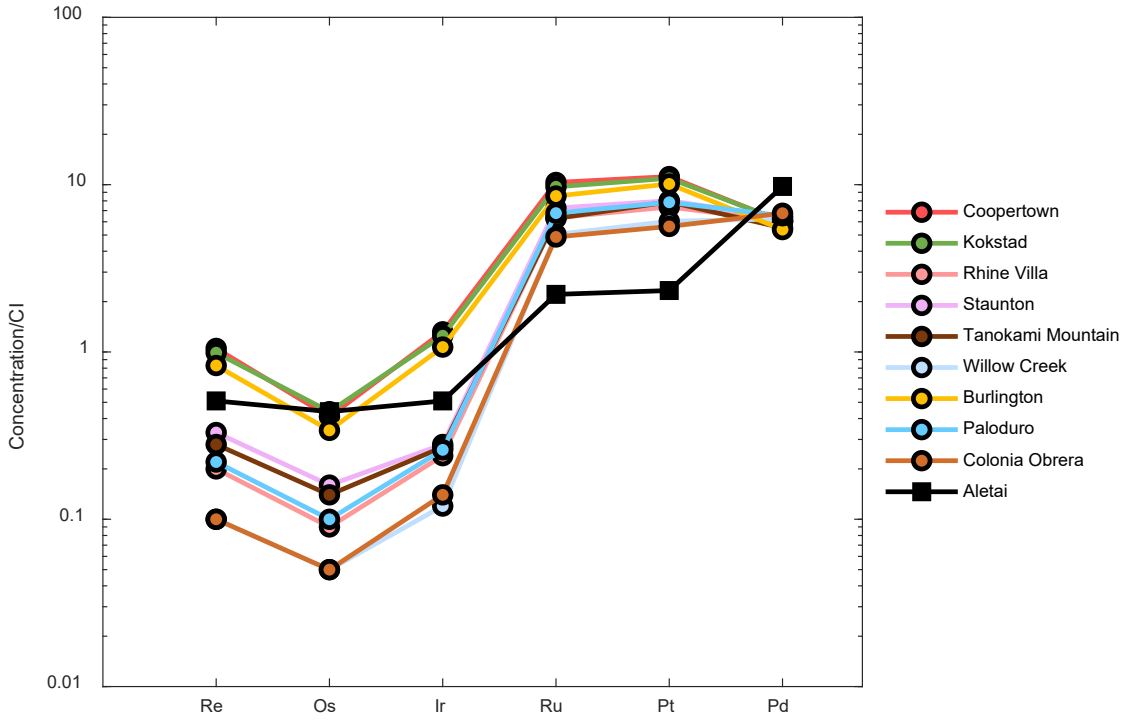

Figure 2.2 Bulk CI-chondrite normalized HSE abundance plot of nine IIIE irons and the anomalous IIIE iron Aletai obtained via isotope dilution. Bulk composition data were normalized to concentrations obtained for the CI-chondrite Orgueil (Horan et al., 2003). Note the pattern obtained for Aletai differs from that of the other IIIE irons. Uncertainties are smaller than symbol sizes.

2.5.2 Highly Siderophile Element Concentrations and Re-Os systematics

Highly siderophile element concentrations obtained via isotope dilution are reported in Table 2.2. Chondrite-normalized data for bulk samples define nested HSE patterns that, for the most part, do not cross one another (Fig. 2.2). All of the irons analyzed here exhibit depletions in the strongly compatible elements Re, Os, and Ir, relative to Ru, Pt, and Pd. The anomalous IIIE iron Aletai has Ni, Ga, and Ge concentrations similar to those of the other group IIIE irons, consistent with its original classification. The HSE abundances reported here, however, differ substantially from the other IIIE irons. Aletai exhibits similar depletions in Re and Ir, but stronger depletions in Ru and Pt, relative to the other irons. The Os abundance of Aletai is also slightly enriched relative to most of the other irons and is inconsistent with the trend being established.

Rhenium-Os isotopic data for the IIIE irons are provided in Table 2.2 and are plotted relative to a 4.56 Ga reference isochron in Figure 2.3. The IIIE irons are characterized by a moderate range of $^{187}Re/^{188}Os$ and $^{187}Os/^{188}Os$ of 0.7542 to 1.0278 and 0.15678 to 0.17662, respectively. Willow Creek, Paloduro, and Tanokami Mountain do not plot within uncertainties of the reference isochron, suggesting minor open-system behavior within those meteorites, possibly related to the inferred impacts to the parent body or to terrestrial weathering processes. The remaining IIIE irons plot within uncertainty of the reference isochron, indicating closed-system behavior in those meteorites. Regression of all ^{187}Re-^{187}Os data using ISOPLOT (Ludwig, 2003) yields an imprecise age of 4387 ± 440 Myr and an initial $^{187}Os/^{188}Os$ of 0.0988 ± 0.0069.

Table 2.2 Rhenium-Os isotopic and HSE composition data, obtained by isotope dilution for nine IIIE irons and Aletai.

Sample	Wt.	Re	Os	Ir	Ru	Pt	Pd	$^{187}Re/^{188}Os$	2σ	$^{187}Os/^{188}Os$	2σ
Coopertown	0.0946	40.24	189.8	599.4	6697	9603	3379	1.028	0.0010	0.1766	0.00018
Kokstad	0.0770	38.86	203.1	567.4	6306	9386	3407	0.9004	0.0009	0.1671	0.00017
Staunton	0.1636	12.73	72.17	129.4	4705	6894	3586	0.8544	0.0009	0.1638	0.00016
Willow Creek	0.1196	4.095	22.86	53.08	3273	5192	3518	0.8339	0.0008	0.1629	0.00016
Burlington	0.0999	31.89	153.8	485.2	5555	8673	3033	1.005	0.0010	0.1751	0.00013
Tanokami	0.1366	10.91	65.88	123.9	4080	6786	3107	0.8008	0.0008	0.1582	0.00016
Mountain Paloduro	0.2009	8.267	47.66	119.7	4389	6744	3672	0.8396	0.0008	0.1612	0.00016
Rhine Villa	0.2253	7.608	42.62	110.3	4121	6326	3406	0.8641	0.0009	0.1647	0.00016
Colonia Obrera	0.1664	4.072	23.89	64.18	3165	4837	3798	0.7542	0.0008	0.1568	0.00016
Aletai *(an.)*	0.1491	19.57	201.9	230.4	1432	2001	5491	0.4671	0.0005	0.1321	0.00013

Sample weights reported in g. Elemental concentrations reported in ppb.

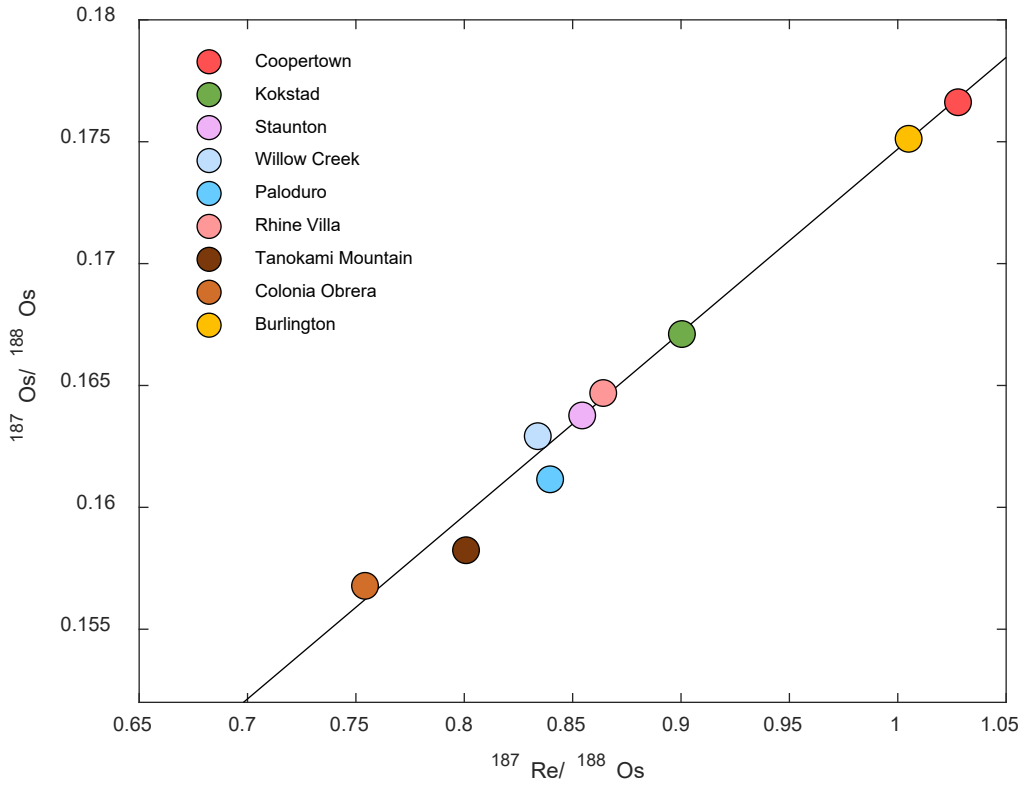

Figure 2.3 $^{187}Re/^{188}Os$ vs. $^{187}Os/^{188}Os$ isochron plot for the group IIIE iron meteorites. Aletai is no longer included. Data are shown relative to a 4.56 Ga chondritic reference isochron. Uncertainties are smaller than symbol size.

2.5.3 Platinum Isotopic Compositions and CRE Correction

The $\mu^{196}Pt$ values for select IIIE irons and Aletai range from 3 ± 8 to 27 ± 8 (Table 2.3). Those that fall within the 2SD reproducibility of the $^{196}Pt/^{195}Pt$ ratio of the laboratory standard (± 8 ppm) are assumed to have been minimally affected by CRE, whereas those that fall outside of this range are interpreted to have isotopic compositions modified by CRE. As all irons analyzed here, apart from Coopertown, fall outside of the range established by the standards, corrections for the Mo, Ru, and W isotopic compositions of these meteorites are necessary.

Table 2.3 Platinum isotopic compositions of select IIIE irons and Aletai.

Sample	*n*	μ^{196}Pt	±
Coopertown	3	3	8
Burlington	3	10	8
Kokstad	3	22	8
Tanokami Mountain	2	26	8
Aletai *(an.)*	3	27	8

n is number of analyses. Uncertainties reflect the 2SD of the standards run during the analytical campaign.

2.5.4 Molybdenum, Ru, and W Isotopic Compositions

Molybdenum, Ru, and W isotopic compositions for select IIIE irons and Aletai are reported in Tables 2.4 through 2.6. The Mo data obtained here are consistent with previously reported Mo isotopic data for group IIIE irons (Table 2.7). The IIIE irons are characterized by CRE-uncorrected μ^{94}Mo values ranging from 80 ± 13 (2SD) to 100 ± 14, μ^{95}Mo values ranging 27 ± 10 to 51 ± 8, and μ^{97}Mo values ranging 19 ± 5 to 25 ± 4. Cosmic ray exposure-corrected group averages are 104 ± 14, 52 ± 10, and 19 ± 5 for μ^{94}Mo, μ^{95}Mo, and μ^{97}Mo, respectively. Molybdenum data for Aletai were corrected using μ^{i}Mo-μ^{196}Pt slopes obtained by Spitzer et al. (2020) for the IIAB iron meteorites, as they are better constrained than the μ^{i}Mo-μ^{196}Pt slopes obtained for this study (Table 2.8). Slopes that were not reported directly in Spitzer et al. (2020) were calculated from their published data via a Model 1 regression using ISOPLOT (Ludwig, 2003). Several iron meteorite groups have been measured with respect to their μ^{i}Mo-μ^{196}Pt variations, and μ^{i}Mo-μ^{196}Pt slopes

are consistent across all groups, thus allowing for the correction of Aletai's isotopic compositions using the better-defined slopes. Cosmic ray exposure-corrected μ^{94}Mo, μ^{95}Mo, and μ^{97}Mo values for Aletai are 121 ± 14, 58 ± 8, and 22 ± 5, respectively. The average CRE-corrected μ^{100}Ru value obtained for the IIIE irons is -47 ± 9, which is consistent with the group average reported by Worsham et al. (2019). The CRE-corrected μ^{100}Ru value obtained for Aletai is -55 ± 8. The average μ^{183}W value obtained for the IIIE irons is 0 ± 3, which overlaps within uncertainty of the group average value of -5 ± 4 reported by Kruijer et al. (2017). The μ^{183}W value obtained for Aletai is -1 ± 3. The CRE-corrected Mo, Ru, and W isotopic data for Aletai are not resolved from the group IIIE averages.

Table 2.4 CRE-uncorrected Mo and Ru isotopic compositions of select IIIE irons and Aletai.

	n	μ^{92}Mo	±	μ^{94}Mo	±	μ^{95}Mo	±	μ^{97}Mo	±	μ^{100}Mo	±	*n*	μ^{100}Ru	±
Coopertown	2	106	41	100	14	51	8	21	6	20	22	3	-42	8
Burlington	2	119	37	97	12	41	8	22	5	17	20	3	-45	8
Kokstad	2	96	37	92	12	37	8	19	5	13	20	3	-34	8
Tanokami Mountain	1	70	42	80	13	27	10	25	4	22	22	2	-28	8
Aletai *(an.)*	3	129	43	113	14	48	8	20	5	29	21	2	-23	8

n is number of analyses. Uncertainties reflect the 2SD of the standards run during the analytical campaign.

Table 2.5 CRE-corrected Mo and Ru isotopic compositions of select IIIE irons and Aletai.

	n	μ^{92}Mo	±	μ^{94}Mo	±	μ^{95}Mo	±	μ^{97}Mo	±	μ^{100}Mo	±	*n*	μ^{100}Ru	±
Coopertown	2	110	41	102	14	53	8	20	6	20	22	3	-44	8
Burlington	2	135	37	105	12	49	8	20	5	17	20	3	-52	8
Kokstad	2	131	37	109	12	55	8	16	5	13	20	3	-49	8
Tanokami Mountain	1	112	42	100	13	51	10	21	4	23	22	2	-46	8
IIIE Average	7	124	40	104	14	52	10	19	5	18	20	11	-47	9
Aletai *(an.)*	3	143	43	121	14	58	8	22	5	26	21	2	-55	8

n is number of analyses. Uncertainties reflect the 2SD of the standards run during the analytical campaign.

Table 2.6 Tungsten isotopic compositions for select IIIE irons and Aletai.

	n	$\mu^{182}W_{Measured\ (6/4)}$	±	$\mu^{183}W_{Measured}$	±	$\mu^{182}W_{Corrected}$	±	ΔT_{CAI}	±
Coopertown	1	-338	6	2	3	-335	8	1.2	0.7
Burlington	2	-335	7	-2	3	-325	10	2.1	1.0
Kokstad	1	-352	6	0	3	-330	8	1.6	0.8
IIIE Average	4	-342	6	0	3	-330	8	1.6	0.8
Aletai *(an.)*	1	-361	6	-1	3	-335	8	1.2	0.8

n is number of analyses. Uncertainties reflect the 2SD of the standards run during the analytical campaign.

Table 2.7 Comparison between literature Mo isotopic data for the group IIIE irons and data reported in this study. All data are uncorrected for CRE effects.

Sample	Reference	*n*	μ^{94}Mo	±	μ^{95}Mo	±	μ^{97}Mo	±
Coopertown								
	Worsham et al. (2019)	4	91	28	51	10	29	6
	This study	1	100	14	51	8	21	6
Burlington								
	Worsham et al. (2019)	4	95	11	52	11	34	7
	This study	1	97	12	41	8	22	5
Kokstad								
	Worsham et al. (2019)	8	86	14	33	13	26	9
	This study	1	92	12	37	8	19	5
Staunton*								
	Burkhardt et al. (2011)	5	81	30	39	12	19	11
	Poole et al. (2017)	8	107	13	45	9	25	7

* not included in this study.

Table 2.8 Comparison of μ^{i}Mo-μ^{196}Pt slopes obtained by Spitzer et al. (2020) for the IIAB irons and slopes obtained in this study for the IIIE irons.

	μ^{92}Mo-μ^{196}Pt	μ^{94}Mo-μ^{196}Pt	μ^{95}Mo-μ^{196}Pt	μ^{97}Mo-μ^{196}Pt	μ^{100}Mo-μ^{196}Pt
This study	-1.6 ± 2.3	-0.76 ± 0.77	-0.81 ± 0.58	0.16 ± 0.27	-0.04 ± 1.1
Spitzer et al. (2020)*	-0.517 ± 0.093	-0.313 ± 0.079	-0.387 ± 0.057	-0.071 ± 0.057	0.118 ± 0.081

*slopes not reported directly were calculated from the published data using ISOPLOT.

2.6 Discussion

2.6.1 Fractional Crystallization Model

2.6.1.1 Modeling Approach

The variations seen in HSE concentrations among the IIIE iron meteorites are broadly consistent with fractional crystallization. With solid metal-liquid metal partition coefficients (D values) greater than 1, Re, Os, Ir, Ru, and Pt concentrations are expected to decrease in evolving solid and liquid metal as crystallization proceeds, while Pd, with a D value of less than 1, normally increases through a crystallization sequence. Similar to previous studies that explored crystallization processes of iron meteorite groups (e.g., McCoy et al., 2011; Hilton et al., 2020; Zhang et al., 2022), the origin of the IIIE irons by fractional crystallization can be further examined through detailed modeling of HSE behavior. To do so, appropriate D_E values for each element were calculated using parameterization methods developed by Jones and Malvin (1990) and advanced by Worsham et al. (2016b), Chabot et al. (2017), and Chabot and Zhang (2021):

$$\frac{1}{D_E} = \frac{[\text{FeDomains}]^{\beta_{SPC}}}{D_o} \qquad \text{Eq. 2.2}$$

where D_o is the solid metal-liquid metal partition coefficient in the light element-free Fe-Ni system from Chabot et al. (2017), and β_{SPC} is a constant specific to the element being fit and determined using Eq. 2.3 from Chabot et al. (2017):

$$\beta_{SPC} = \left[\frac{2X_S}{2X_S + 4X_P + 4X_C}\right]\beta_S + \left[\frac{4X_P}{2X_S + 4X_P + 4X_C}\right]\beta_P + \left[\frac{4X_C}{2X_S + 4X_P + 4X_C}\right]\beta_C \quad \text{Eq. 2.3}$$

where X_S, X_P, and X_C are the mole fractions of S, P, and C in the metallic liquid, respectively, and β_S, β_P, and β_C are constants specific to the element being fit and determined by Chabot et al. (2017). Iron domains, which are defined as the fraction of free atoms available in the liquid metal not being taken up by S, P, and C, are also determined using Eq. 2.4 (Chabot et al., 2017):

$$\text{Fe domains} = \left[\frac{1 - 2X_S - 4X_P - 4X_C}{1 - X_S - 3X_P - 3X_C}\right] \quad \text{Eq. 2.4}$$

where constants are based on the expected speciations for S, P, and C in the system (e.g., FeS, Fe_3P, and Fe_3C). A constant D_o value of 0.1 for P was taken from Chabot et al. (2017) and a constant D_o value of 0.37 for C was taken from Worsham et al. (2016b). Siderophile element partitioning behavior is strongly influenced by S, P, and C concentrations in the parental melt, and thus the abundance of the lighter elements must be constrained for the model.

At the start of the model, the metallic core is given a defined composition and is assumed to be completely liquid. As crystallization proceeds, solid metal is produced and the composition of the remaining liquid changes. For the purpose of this study, Eq. 2.5 is used to calculate the concentration of an element in the evolving liquid:

$$C_{L(n)} = \frac{C_{L(n-1)}}{F_{(n-1)} + (1 - F_{(n-1)})(D_{(n-1)})} \quad \text{Eq. 2.5}$$

where F_n is the fraction of liquid in the system, $C_{L(n)}$ is the concentration of a given element in the liquid at F_n, and D_n is the partition coefficient of that element in that moment of

fractional crystallization. Element concentrations in the crystallizing solids (C_s) are calculated using Eq. 2.6.

$$C_S = C_{L(n)} D_n \quad \text{Eq. 2.6}$$

An additional calculation outlined in Chabot and Zhang (2021) was employed in order to track the influence of trapped melt on the model. This addition takes into consideration the possibility that metal may have formed not only as a result of fractional crystallization, but also by the crystallization of trapped melt pockets containing troilite, which can affect the composition of the remaining solid metal in the system, and has been shown to have a strong influence in the formation of some magmatic iron groups (Chabot and Zhang, 2021; Zhang et al., 2022). Troilite takes in little of the HSE, and its increasing volumetric presence in the trapped liquid leads to enrichment of HSE in the remaining metallic liquid relative to the entirety of the trapped liquid. Solid compositions that crystallized from the trapped melt are calculated as follows:

$$C_{S(trap)} = \frac{C_L}{1 - x} \quad \text{Eq. 2.7}$$

where *x* is the concentration of S in the liquid at each F_n increment divided by the weight concentration of S (36.5%). Concentrations of liquids, solids, and trapped melt, β_{SPC} values, Fe domains, and D values were calculated at 0.1 increments of crystallization for each modeled element.

2.6.1.2 Modeling Results

Concentrations of S, P, and C can greatly affect the partitioning behavior of siderophile elements during the crystallization of metallic liquids, and therefore must be constrained in order to produce a successful crystallization model. An initial P concentration for the IIIE meteorites was estimated by dividing the P concentration of the least evolved IIIE analyzed here, Coopertown (0.18%), by a D_o value of 0.1 (Chabot et al., 2017), giving an initial P concentration of 1.8 wt.%. Carbon content was first estimated following a similar method. The measured C concentration of Coopertown (285 ppm) from Moore et al. (1969) was divided by a D_o of 0.37 (Worsham et al., 2016b), suggesting an initial C concentration of 0.08 wt.%. However, the analyses conducted by Moore et al. (1969) were targeted primarily on the metallic phase of the meteorites, thereby excluding larger carbide inclusions present in the samples, and consequently underestimating their overall C content. Thus, a higher C concentration of 0.15 wt.% was used here. This concentration is similar to that used for the modeling of other C-rich iron meteorite groups, such as the IAB complex irons (Worsham et al., 2016b; Hirschmann et al., 2021). In practice, starting concentrations of P and C have only a minor effect on HSE partitioning behavior relative to the effect of S.

An initial S content was estimated by following a similar method to that of Chabot et al. (2004) and Zhang et al. (2022), in which fractionation trends of Ga, Ge, and Ir were modeled under different starting S concentrations to achieve a best fit to the data. Gallium, Ge, and Ir were chosen due to the distinct non-linear trends they produce through a crystallization sequence that are particularly sensitive to starting S concentration. The elements were plotted against As because As typically has a relatively large range of

concentrations within an iron meteorite group (Wasson, 1999; Wasson and Richardson, 2001; Chabot et al., 2004). Further, the partitioning behavior of As is better understood than that of other elements, particularly Au, making it useful when modeling iron meteorite crystallization sequences (Chabot et al., 2017). Best fits to Ga, Ge, and Ir suggest an initial S concentration of 9 to 14 wt.% (Figure 2.4). There is considerable scatter across the group, and Tanokami Mountain in particular noticeably deviates from the Ga-As, Ge-As, and Ir-As trends established by the rest of the IIIE irons, possibly as a consequence of terrestrial weathering processes experienced by the iron. All three trends are otherwise best fit using the 12 wt.% S model, meaning that the most favorable light-element concentrations determined for this model are 12 wt.% S, 1.8 wt.% P, and 0.15 wt.% C.

Highly siderophile element concentrations of the parental melt were then treated as free parameters and varied until a model crystallization sequence was produced that matched the HSE abundances of the IIIE irons, while also ensuring that modeled HSE ratios of the initial liquid remained within the range established by chondrites. The preferred model presented here is not a unique solution, as there are countless parent melt compositions that can be modeled to produce a specific iron meteorite composition. The goal of the modeling conducted here is to maximize the number of IIIE irons that can be generated via a common fractional crystallization process. Modeled solid and liquid evolution tracks for Re (ppb) versus Re/Os ratio are shown in Figure 2.5 along with data

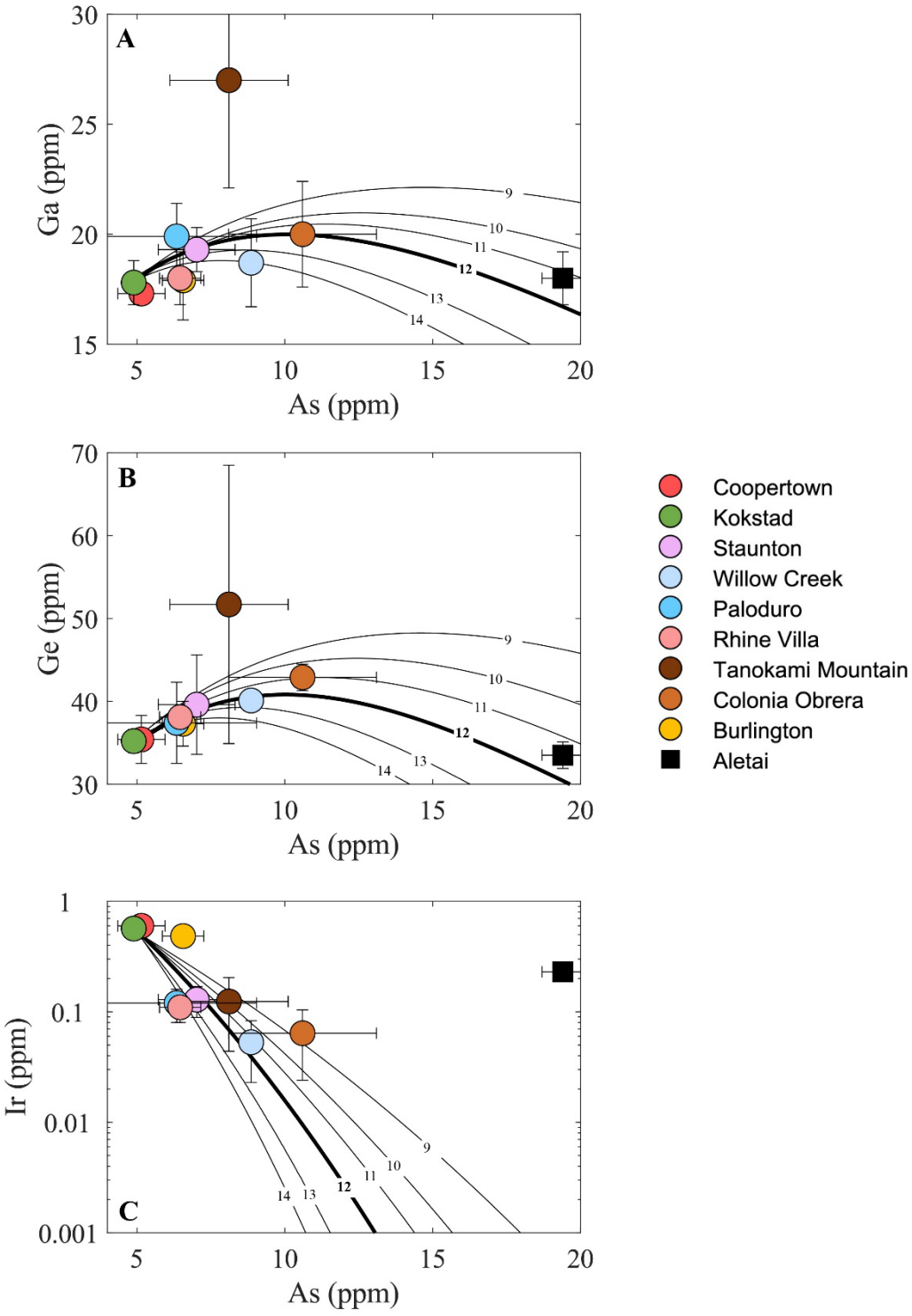

Figure 2.4 Plots of Ga (ppm), Ge (ppm), and Ir (ppm) vs. As (ppm). Solid black lines represent modeled S concentrations (9-14 wt.%).

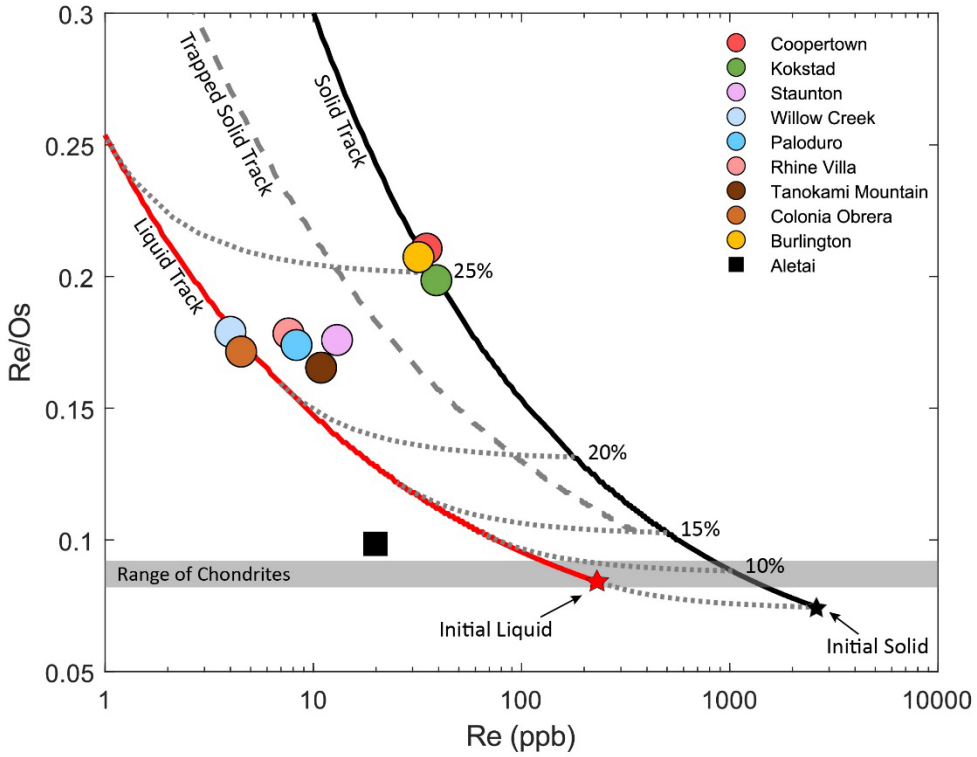

Figure 2.5 Best-fit fractional crystallization model for Re (ppb) vs. Re/Os systematics for the IIIE iron meteorites and Aletai. Small dotted gray lines represent solid metal-liquid metal curves for the labeled increments of fractional crystallization.

Table 2.9 Calculated HSE concentrations for the model discussed in the text, and proposed parental melt compositions for the IIIAB, IIAB, IVA, IVB, IIC, and South Byron Trio (SBT) systems for comparison.

	Re	Os	Ir	Ru	Pt	Pd
IIIE	235	2800	2500	3600	5600	3600
IIIAB[a]	260	2800	2800	4400	5900	3100
IIAB[a]	260	2900	2900	4800	6500	2100
IVA[b]	295	3250	2700	3900	5900	4500
IVB[c]	1410	21600	17500	19600	29800	10900
IIC[d]	280	3350	3050	4340	6070	5300
SBT[e]	770	9400	8500	13000	16000	84000

all concentrations are in ppb.
[a] Data from Hilton et al. (2022). [b] Data from McCoy et al. (2011). [c] Data from Walker et al. (2008). [d] Data from Tornabene et al. (2020). [e] Data from Hilton et al. (2019b).

for the IIIE irons and Aletai. The initial parental melt HSE concentrations for this model are provided in Table 2.9. The crystallization of all nine IIIE irons can be accounted for under the conditions of this model. Coopertown, Burlington, and Kokstad plot directly on the solid track, representing equilibrium solids at ~25% fractional crystallization. The remaining six IIIE irons plot either directly on the liquid track or between the solid and liquid tracks, indicating that these irons could have formed via fractional crystallization with mixing of various amounts of trapped material. Aletai plots outside of the bounds of this model, further indicating that it does not sample the same crystallization sequence as the IIIE irons. The incorporation of other HSE systematics under the same starting conditions can again account for the formation of all nine IIIE irons, with all irons plotting near or directly on the solid track (Figure 2.6). This is consistent with the more limited variation in measured concentrations seen in elements like Pt and Ru when compared to Re and Os. This is also observed in the evolution of the modeled HSE patterns under these parental melt conditions (Figure 2.7). Consistent with their crystallization as equilibrium solids, Coopertown, Burlington, and Kokstad follow the modeled HSE pattern at 25% fractional crystallization with minimal deviation. The other six IIIE irons deviate from the modeled patterns, most noticeably in their Re, Os, and Ir concentrations, indicating that a process other than simple fractional crystallization was involved in their formation. Discrepancies between the modeled and measured HSE concentrations could be a result of solid-metal liquid-metal mixing, with influence from a more S-rich trapped melt. They could also be a result of the partition coefficients utilized here not matching the actual partitioning behavior of elements in the IIIE parent body core.

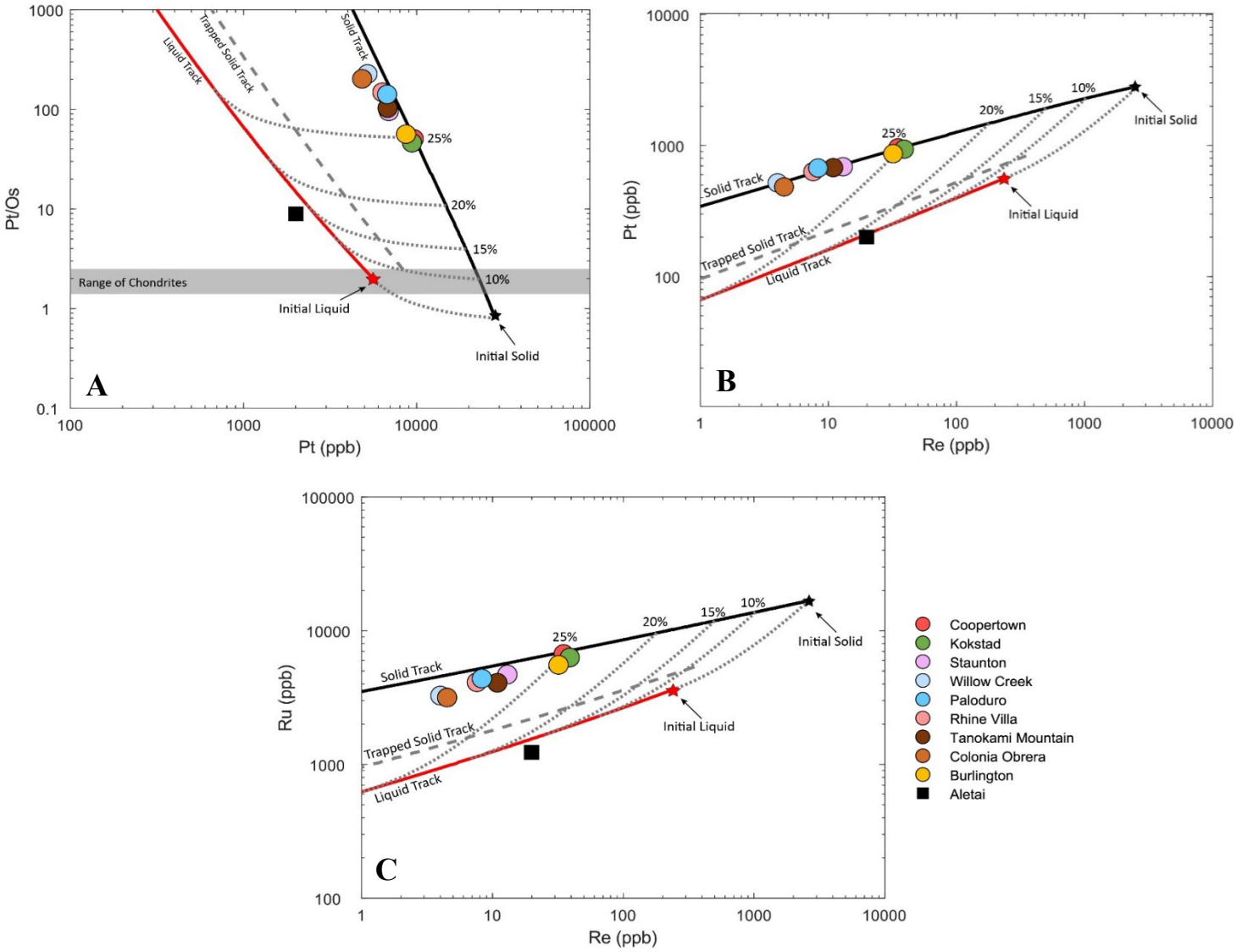

Figure 2.6 Best-fit fractional crystallization model for Pt (ppb) vs. Pt/Os (a), Re (ppb) vs. Pt (ppb) (b), and Re (ppb) vs. Ru (ppb) (c) systematics for the IIIE iron meteorites and Aletai. Small dotted gray lines represent solid metal-liquid metal mixing curves for the labeled increments of fractional crystallization.

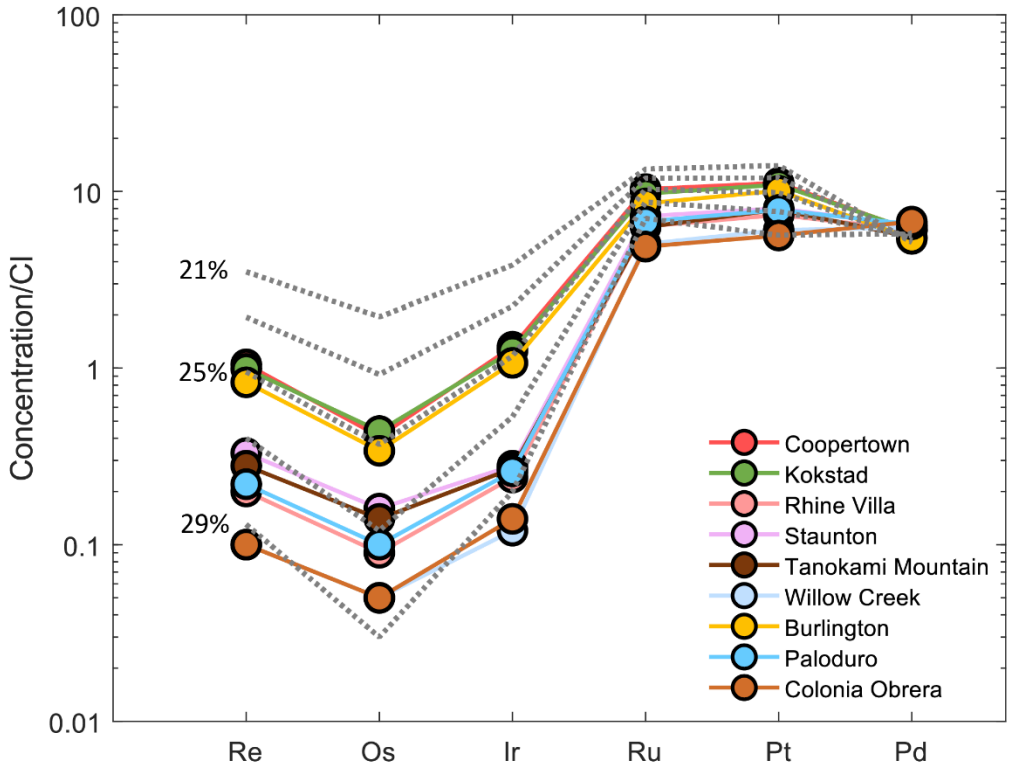

Figure 2.7 Bulk CI-chondrite normalized equilibrium solid compositions at 2 wt.% increments under the conditions of the proposed fractional crystallization model compared to the measured HSE concentrations of the IIIE irons.

The initial melt concentrations for HSE calculated for this model are shown in Figure 2.8 compared to estimated HSE concentrations for other magmatic iron meteorite groups. The estimated HSE concentrations of the IIIE parent body core are ~4 times higher than that of an NC chondrite-like parent body, consistent with modeled parent melt compositions of other NC-type iron meteorite parent bodies, and corresponding to a core size that is ~22% of the mass of the entire parent body.

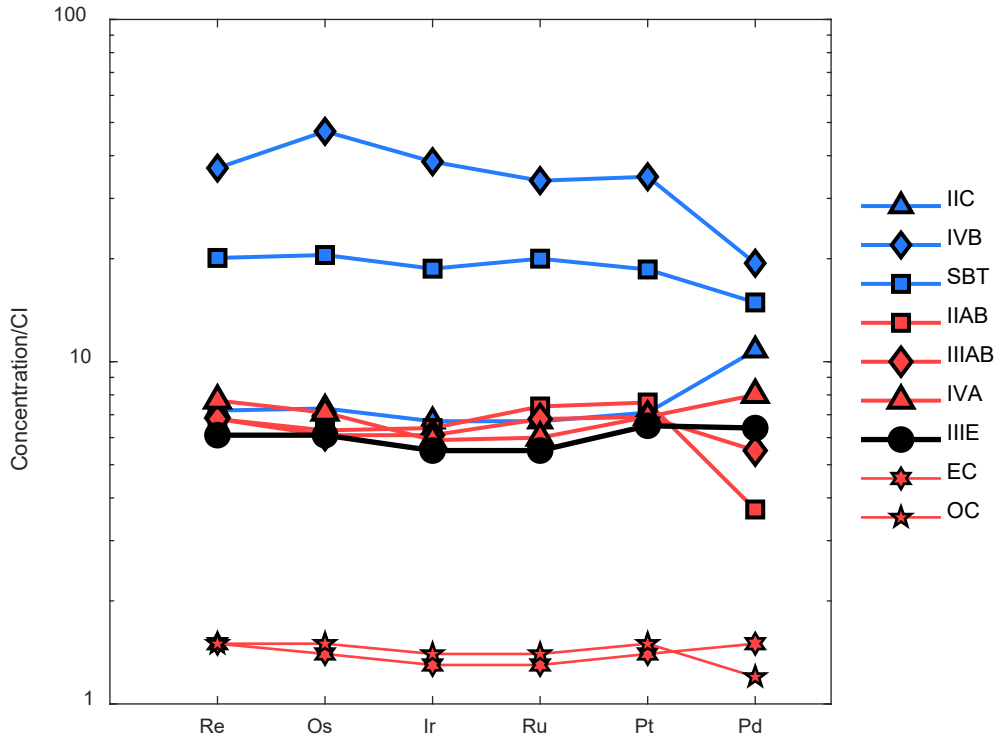

Figure 2.8 CI-chondrite normalized calculated HSE parental melt composition of the IIIE iron meteorites. CI-chondrite normalized parent melt compositions for the IIC irons (Tornabene et al., 2020), IVB irons (Walker et al., 2008), South Byron Trio (Hilton et al., 2019b), IIAB irons (Hilton et al., 2022), IIIAB irons (Hilton et al., 2022), and IVA irons (McCoy et al., 2011) are included for comparison. Average compositions for ordinary (OC) and enstatite (EC) chondrites are included as well. Red lines and symbols correspond to NC-type iron meteorites, and blue lines and symbols correspond to CC-type iron meteorites.

2.6.2 Genetics

The incorporation of varying amounts of *r-, s-,* and *p*-process nuclides between the NC and CC reservoirs of the early solar system have allowed for the "genetic" comparison of extraterrestrial materials. For example, CC-type meteorites have been shown to exhibit *s*-process depletions and *r*-process enrichments relative to NC-type meteorites (Budde et al, 2019; Spitzer et al., 2020). These signatures define two distinct mixing lines, as commonly illustrated on plots of μ^{94}Mo vs. μ^{95}Mo values of various extraterrestrial

materials. Additionally, variations in $\mu^{92,94,97}$Mo relative to μ^{100}Ru have revealed a linear relationship among NC-type meteorites that is not observed in CC-type materials (Dauphas et al., 2004; Fischer-Gödde et al., 2015; Worsham et al., 2019). Instead, a correlation is seen in the μ^{183}W value of CC-type meteorites relative to their Mo isotopic compositions (Worsham et al., 2019). This correlation is absent in NC-type meteorites.

The IIIE irons have been previously shown to fall under the NC-type classification (Kruijer et al., 2017; Worsham et al., 2019). The CRE-corrected Mo data obtained here are in agreement with this assessment (Figure 2.9). There are no resolved differences in the CRE-corrected Mo isotopic compositions of the IIIE irons analyzed here, providing further evidence that they sample the same parent body. There is also no resolved difference between the CRE-corrected Mo isotopic composition of Aletai from the group IIIE average, indicating that while Aletai likely does not sample the same crystallization sequence as the other IIIE irons, it does sample the same nebular reservoir. The CRE-corrected Ru isotopic data reported here further support their NC classification, with the IIIE irons and Aletai falling within the correlation established by other NC-type irons (Figure 2.10). This is the same observation for the μ^{183}W values obtained for Aletai and the IIIE irons, which fall within the narrow range established by other NC bodies (Figure 2.11).

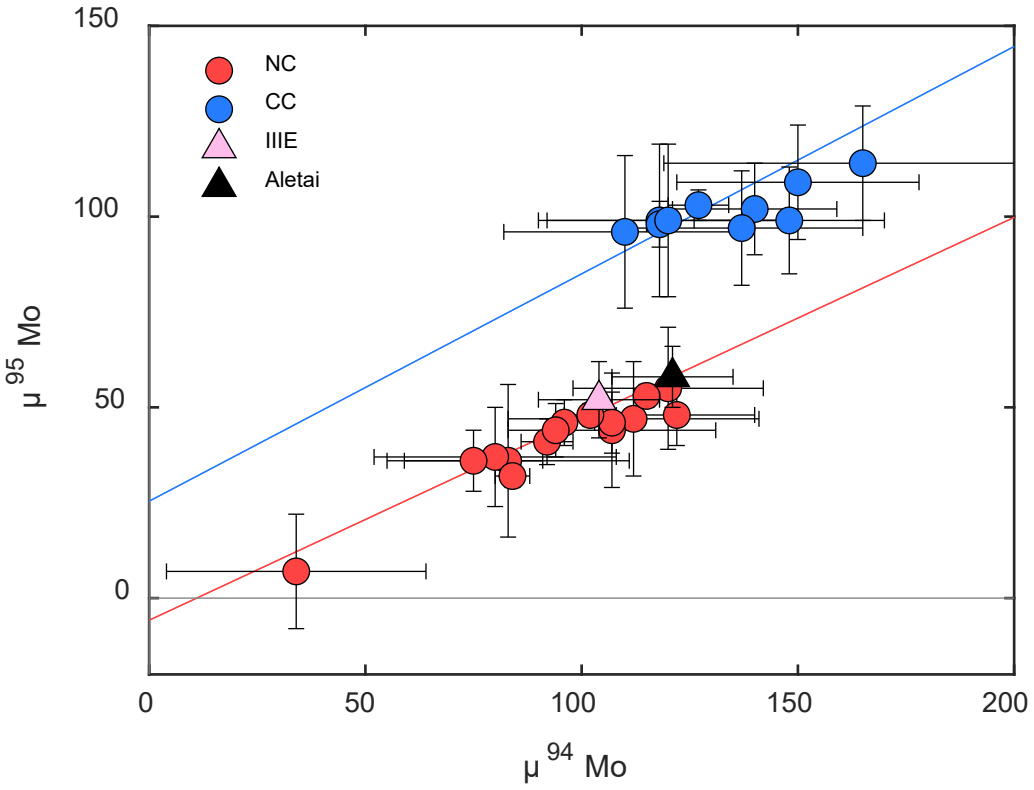

Figure 2.9 Compilation of μ^{94}Mo vs. μ^{95}Mo data for iron meteorites. Data compiled from Poole et al. (2017), Bermingham et al. (2018), Worsham et al. (2019), Hilton et al. (2019b), and Tornabene et al. (2020). Blue symbols represent CC-type iron meteorites (IID, IIF, IIIF, IVB, South Byron Trio, and the ungrouped iron meteorites Dronino, Tishomingo, and Chinga). Red symbols represent NC-type iron meteorites (IC, IIAB, IIIAB, IVA, and the ungrouped iron meteorite Gebel Kamil). Red and blue lines represent NC and CC lines reported by Spitzer et al. (2020) and Budde et al. (2019), respectively. Data from this study for the IIIE irons and Aletai are also plotted, represented by the pink and black triangles, respectively.

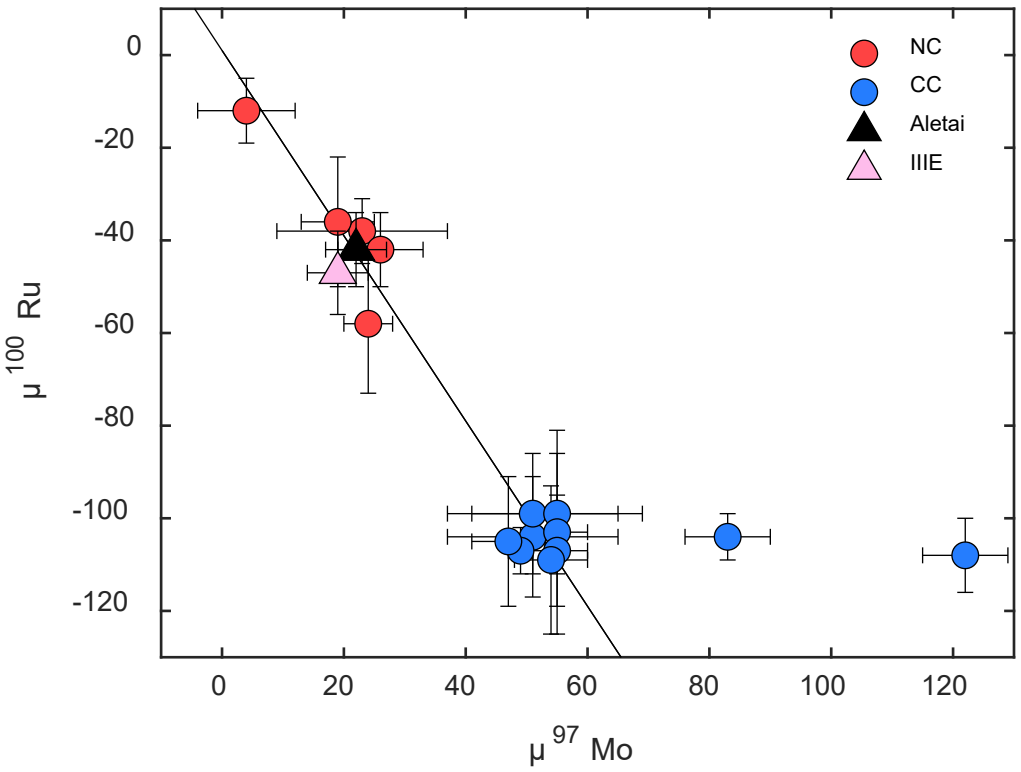

Figure 2.10 Plot of μ^{97}Mo and μ^{100}Ru for iron meteorites. Data compiled from Worsham et al. (2019), Bermingham et al. (2018), and Hilton et al. (2019b). Blue symbols represent CC-type iron meteorites (IID, IIF, IIIF, IVB, South Byron Trio, and the ungrouped iron meteorites Dronino, Tishomingo, and Chinga). Red symbols represent NC-type iron meteorites (IC, IIAB, IIIAB, IVA, and the ungrouped iron meteorite Gebel Kamil). The black line represents the regression of the Mo-Ru correlation from Bermingham et al. (2018). Data from this study for the IIIE irons and Aletai are also plotted, represented by the pink and black triangles, respectively.

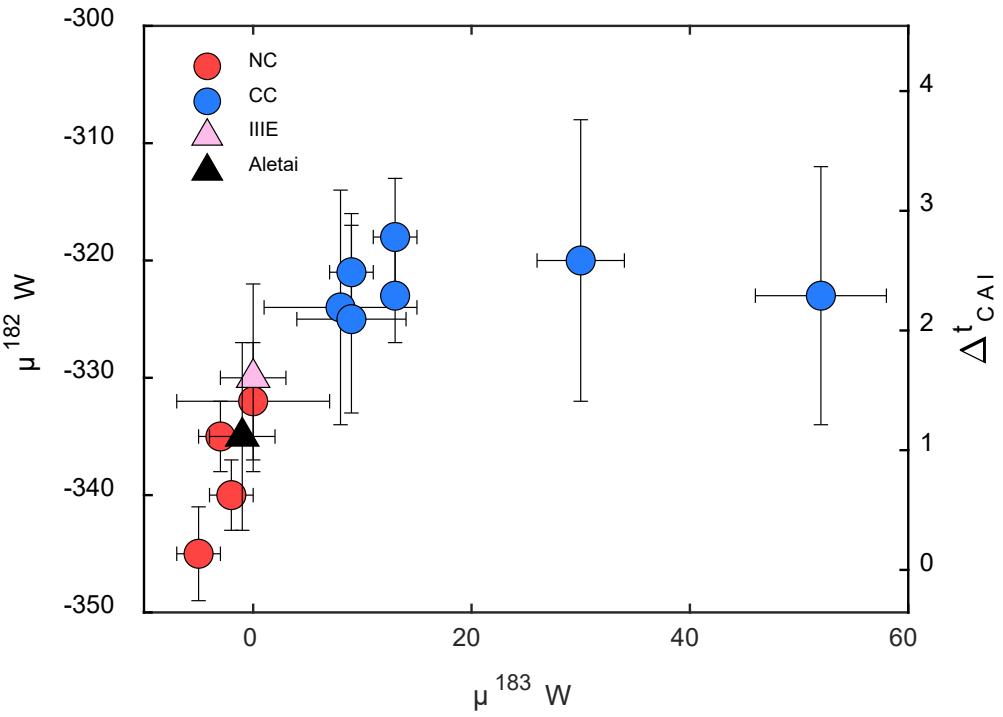

Figure 2.11 Plot of $\mu^{183}W$ vs. $\mu^{182}W$ values of magmatic iron meteorite groups. Right y-axis represents time of metal-silicate segregation, relative to CAI formation, in Myr. Data compiled from Kruijer et al. (2017) and Hilton et al. (2019b). Blue symbols represent CC-type iron meteorites (IIC, IID, IIF, IIIF, IVB, South Byron Trio, and Wiley). Red symbols represent NC-type iron meteorites (IC, IIAB, IIIAB, and IVA). Data from this study for the IIIE irons and Aletai are also plotted, represented by the pink and black triangles, respectively.

2.6.3 Hf-W Chronology

The similar Mo, Ru, and W isotopic compositions of the IIIE irons and their relation through a shared fractional crystallization process provides evidence for their origin from a common parent body core. The W isotopic composition of the IIIE irons can therefore provide temporal constraints on metal-silicate segregation of the IIIE parent body. Metal-silicate segregation ages are calculated using Eq. 2.8, in which the present-day chondritic $\mu^{182}W$ value is assumed to be -191 ± 8 (Kleine et al., 2004), and the $\mu^{182}W$ value of CAI, which represents the W isotopic composition of the initial solar system, is assumed to be -349 ± 7 (Kruijer et al., 2014).

$$\Delta T_{CAI} = -\frac{1}{\lambda} \ln \left[\frac{(\mu^{182}W)_{sample} - (\mu^{182}W)_{chondrite}}{(\mu^{182}W)_{CAI} - (\mu^{182}W)_{chondrite}}\right] \quad \text{Eq. 2.8}$$

The average CRE-corrected $\mu^{182}W$ composition of the group IIIE irons is -330 ± 8, and yields a model core formation age of 1.6 ± 0.8 Myr after CAI formation (Figure 2.5). Both the average $\mu^{182}W$ composition and metal-silicate segregation age reported here are consistent with those reported for the group IIIE iron meteorites by Kruijer et al. (2014). The $\mu^{182}W$ value obtained for Aletai corresponds to a model core formation age that overlaps that of the IIIE irons, at 1.2 ± 0.8 Myr after CAI.

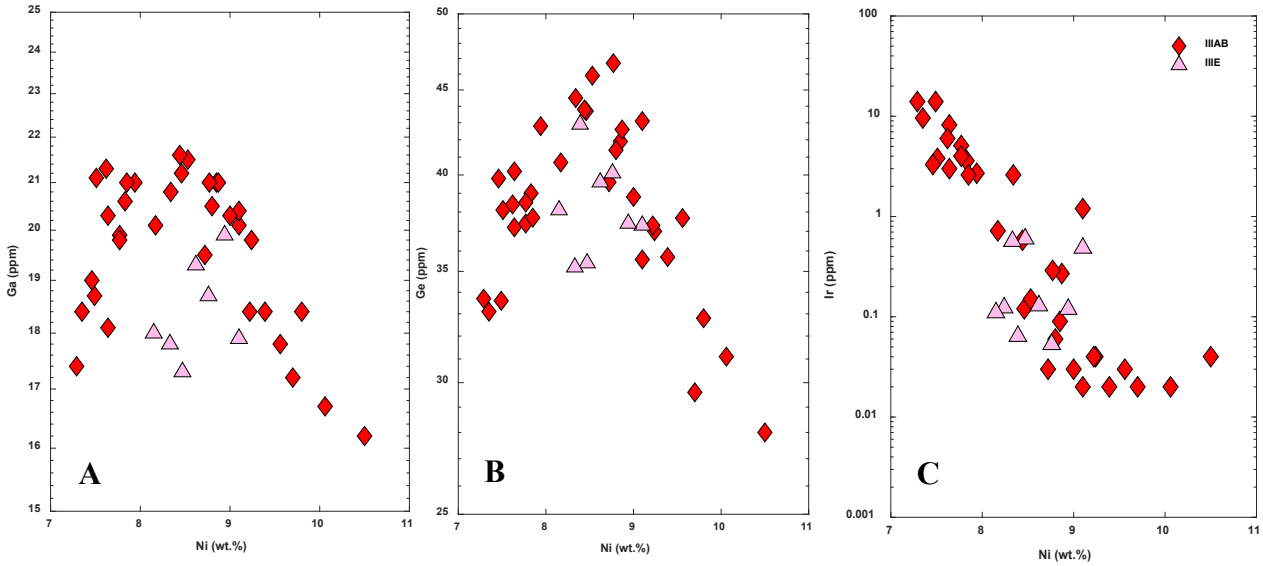

Figure 2.12 Ir (ppm) vs. Ni (wt.%) (a), Ga (ppm) vs. Ni (wt.%) (b), and Ge (ppm) vs. Ni (wt.%) (c) comparisons for the group IIIE and group IIIAB irons. Group IIIAB data are from Scott and Wasson (1973). Group IIIE data are from this study.

2.6.4 Comparison to Group IIIAB

The chemical similarities between the IIIE and IIIAB irons were first noted by Scott and Wasson (1973). The IIIE irons exhibit similar Ga, Ge, Ir, and Ni abundances (Fig. 2.7) as the IIIAB irons, but were designated as a separate group due to their wider kamacite bandwidths, as well as by the presence of C-rich minerals that have not been observed in the IIIAB irons. The two groups were marginally resolved from one another by Malvin et al. (1984) based on Co-, Cu-, As-, Au-, and W-Ni trends. The groups are not resolved from one another in terms of N isotopic compositions, but exhibit slight differences in their C isotopic compositions (Sugiura et al., 2000). The Mo, Ru, and W isotopic compositions of the two groups are within uncertainty of one another, as well as with Aletai (Fig. 2.8 – 2.11). The IIIE and IIIAB irons also reveal broadly similar HSE abundances, with the IIIE irons exhibiting HSE patterns similar to those of the moderately fractionated IIIAB irons (Fig. 2.12). When included in the fractional crystallization model discussed here, all IIIAB

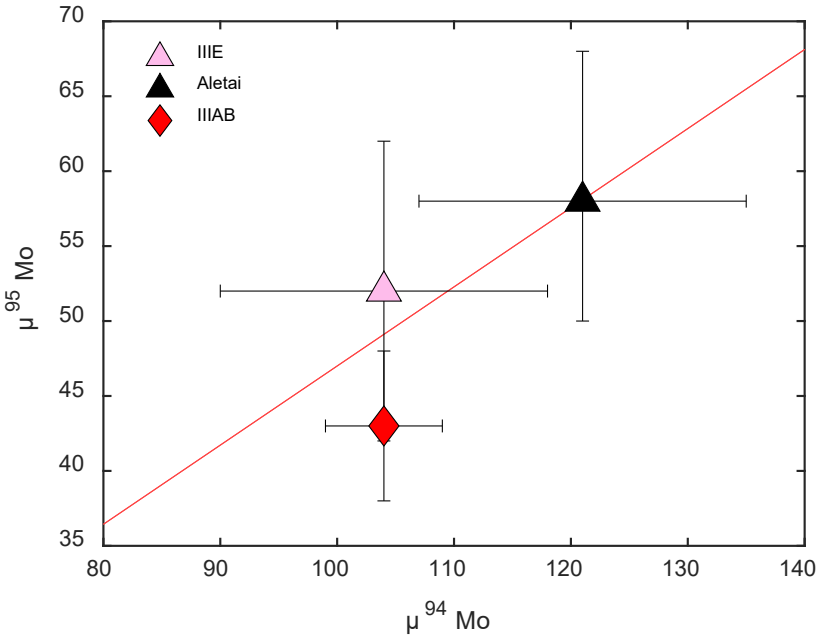

Figure 2.13 Compilation of μ^{94}Mo vs. μ^{95}Mo data for the IIIE and IIIAB irons and Aletai. Red line represent NC line reported by Spitzer et al. (2020). Data for the group IIIAB irons is from Poole et al. (2017) and is represented by the red diamond. Data from this study for the IIIE irons and Aletai are also plotted, represented by the pink and black triangles, respectively.

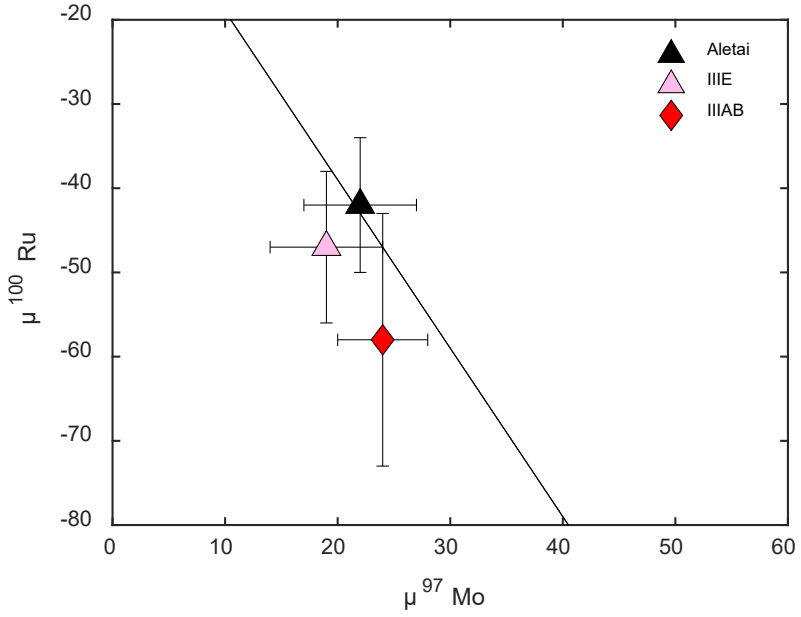

Figure 2.14 Plot of μ^{97}Mo and μ^{100}Ru for the IIIE and IIIAB irons and Aletai. The black line represents the regression of the Mo-Ru correlation from Bermingham et al. (2018). Group IIIAB data is from Bermingham et al. (2018) and is represented by the red diamond. Data from this study for the IIIE irons and Aletai are plotted, represented by the pink and black triangles, respectively.

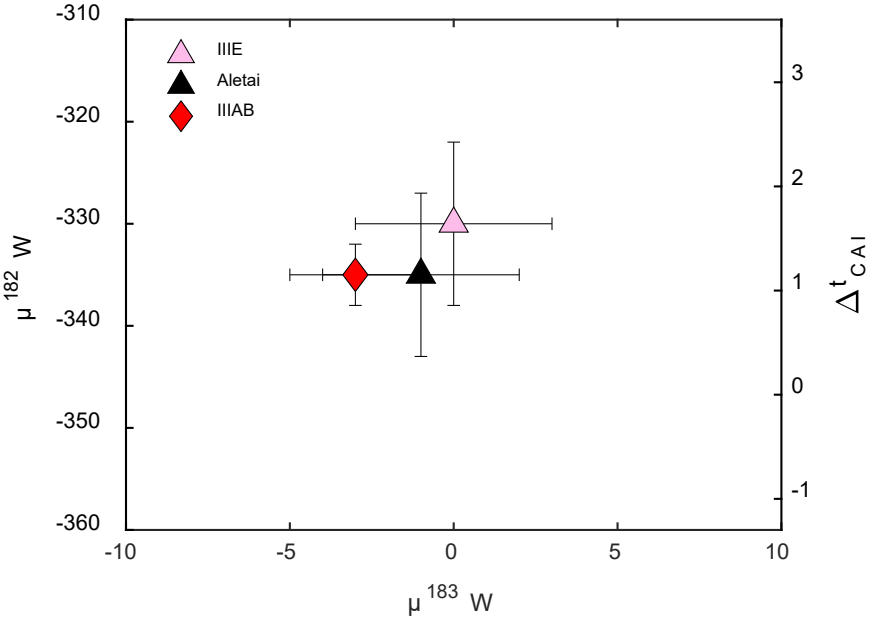

Figure 2.15 Plot of μ^{183}W vs. μ^{182}W values of magmatic iron meteorite groups. Group IIIAB data is from Kruijer et al. (2017) and is represented by the red diamond. Data from this study for the IIIE irons and Aletai are plotted, represented by the pink and black triangles, respectively.

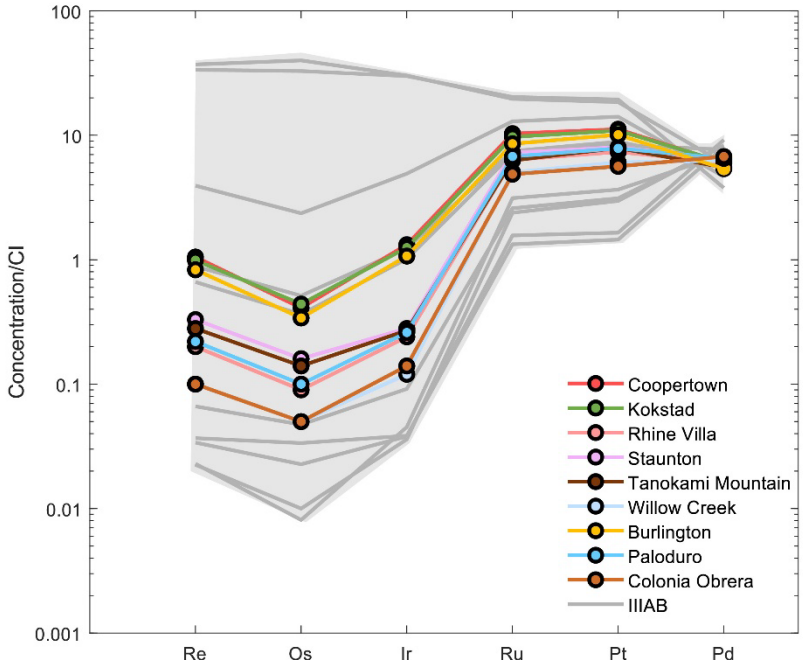

Figure 2.16 Bulk CI-chondrite normalized HSE abundance plot of nine IIIE irons Aletai obtained in this study via isotope dilution. Highly siderophile element abundances for the IIIAB irons are represented by the gray lines and light gray field. Data for the IIIAB irons are from Hilton et al. (2022) and unpublished data. Bulk composition data were normalized to concentrations obtained for the CI-chondrite Orgueil (Horan et al., 2003).

irons for which data was available fall within the bounds established by the model, except in the case of Re/Os vs. Re (ppb), wherein formation of the more fractionated irons are not accounted for (Fig. 2.12). Previous modeling of the IIIAB irons by Hilton et al. (2022) included five minimally fractionated IIIAB irons. These irons (Costilla Peak, Henbury, Charcas, Tamarugal, and Maldyak) are the five IIIAB irons that are accounted for with regard to their Re/Os vs. Re (ppb) systematics in the model discussed here. Further, the model discussed for the IIIAB irons in Hilton et al. (2022) includes parent melt parameters

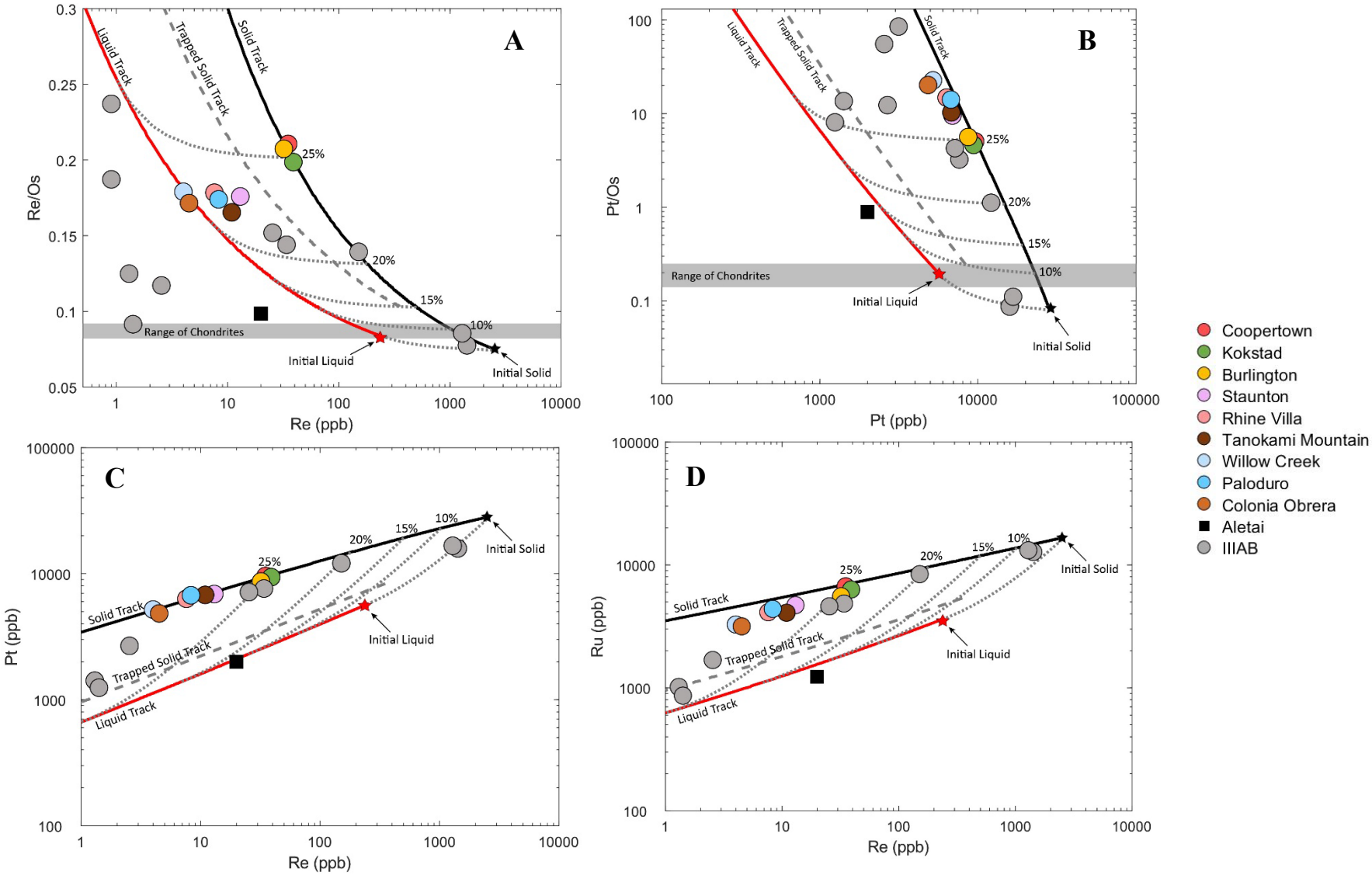

Figure 2.17 Best-fit fractional crystallization model for Re (ppb) vs. Re/Os (a), Pt (ppb) vs. Pt/Os (b), Re (ppb) vs. Pt (ppb) (c), and Re (ppb) vs. Ru (ppb) (d) systematics for the IIIE iron meteorites and Aletai with eight IIIAB irons. Small dotted gray lines represent solid metal-liquid metal mixing curves for the labeled increments of fractional crystallization. Group IIIAB data is from Hilton et al. (2022) and unpublished data.

similar to those of the IIIE model proposed in this study, with the exception of C, which likely did not contribute as much to the formation of the IIIAB irons as it did to the IIIE irons, as evidenced by the mineralogy of the two groups. Despite differences in texture and mineralogy, the bulk chemical characteristics, genetics, and ages of the IIIE and IIIAB irons are permissive of them sampling the same parent body. The two groups could be products of separate crystallization sequences, with the crystallization sequence that produced the IIIE irons richer in C than the crystallization sequence that produced the IIIAB irons. In the case of the two groups forming on separate parent bodies, they must have formed in the NC nebular domain and experienced similar evolutionary processes in order to have produced the remarkably similar geochemical and isotopic compositions observed here.

2.6.5 Aletai

The Ga, Ge, Ir, and Ni concentrations exhibited by Aletai are similar to those of the IIIE irons, explaining its original classification as an anomalous IIIE iron. Additionally, Aletai's mineralogical and textural characteristics are similar to those of the group IIIE irons, further suggesting a common origin (Breen et al., 2016). However, the HSE concentrations exhibited by Aletai do not fit the crystallization trend established by the IIIE irons analyzed here, and instead suggest derivation from a separate crystallization sequence. Despite these differences in HSE abundances, the similarities in isotope genetics, age, and mineralogy between Aletai and the IIIE irons are permissive of a common parent body origin, although likely not via the same crystallization sequence. The formation of Aletai can instead be explained through crystallization of a melt pocket on the IIIE parent

body with a different starting composition and/or different D-values than the composition that produced the IIIE irons, resulting in the different HSE concentration patterns observed for Aletai. As with the IIIAB irons, in the case of Aletai sampling a separate parent body, its formation would had to have occurred in the same nebular domain as the IIIE irons in order to produce isotopic compositions so similar to the group.

2.7 Conclusions

1) The bulk chemical characteristics of the meteorite Aletai are inconsistent with the iron sampling the same crystallization sequence as the other IIIE irons analyzed here. The remaining nine irons can otherwise be related to one another through a common fractional crystallization process, assuming a parent melt containing 12 wt.% S, 1.8 wt.% P, and 0.15 wt.% C.
2) Nucleosynthetic Mo, Ru, and W isotopic compositions indicate that the IIIE irons and Aletai are NC-type meteorites. All genetic data for Aletai overlap with those of the IIIE irons.
3) The Hf-W isotopic system indicates that the IIIE parent body underwent metal-silicate segregation 1.6 ± 0.8 Myr after CAI, and that the parent body Aletai samples differentiated 1.2 ± 0.8 Myr after CAI. These ages are similar to those of other NC-type and CC-type iron meteorite parent bodies.
4) The chemical, genetic, and chronological characteristics shared among the IIIE irons, IIIAB irons, and Aletai are permissive of them sampling the same parent body. Their differences in chemistry, texture, and mineralogy can be explained through their formation via different crystallization sequences.

Chapter 3: Chemical and Genetic Composition of the Ungrouped Iron Meteorite Lieksa

3.1 Abstract

The iron meteorite Lieksa was found in 2017 in Löpönvaara, Finland and later donated to the Finnish Museum of Natural History. Here, we report siderophile and highly siderophile element (HSE) concentrations for Lieksa as well as Mo, Ru, and W isotopic data. Lieksa exhibits a moderate depletion in the volatile siderophile elements Ga and Ge. The iron also exhibits a flat chondrite-normalized HSE pattern, with a slight depletion in Pd, suggesting it formed as a relatively early crystallization product from a melt with chondritic abundances. Lieska's bulk chemical characteristics are distinct from those of the existing iron meteorite groups, suggesting that it cannot be classified as belonging to any of the established groups. Lieksa exhibits an HSE pattern and genetic isotopic composition similar to that of the main group pallasites (PMG). Additional siderophile element and isotopic analyses would be necessary to further explore their relationship, however. Molybdenum, Ru, and W isotopic data indicate that Lieksa formed in the non-carbonaceous (NC) domain of the solar nebula. Radiogenic ^{182}W abundances for Lieksa yield a model metal-silicate segregation age of 1.5 ± 0.8 Myr after calcium aluminum-rich inclusion (CAI) formation, which is within the range established by other NC-type iron meteorite parent bodies.

3.2 Introduction

On May 30, 2017, Pekka Vallimies was hunting for false morel mushrooms in Löpönvaara (63º24.382'N, 30º04.227'E), Finland, approximately 10 km northeast of the town of Lieksa, when he came across what he thought was a potential ore specimen that was heavily coated in rust. Upon removal of some of the rust with a wire brush, Vallimies noted that the find had the metallic sheen and pitted appearance characteristic of some meteorites, leading him to submit the find to the Geological Survey of Finland (GTK). Further examination confirmed the find to be of extraterrestrial origin, and the meteorite Lieksa was subsequently donated by Vallimies to the Finnish Museum of Natural History on May 30, 2018, one year after its original discovery.

Lieksa's main mass was recorded to be 238.3g with the dimensions of 65.9mm by 59.8mm by 29.9mm (Kuva et al., 2017). The meteorite was found to contain approximately 80% metal and 20% silicates, by volume, via x-ray tomography, confirming its status as either an iron meteorite or a pallasite. The silicate phase was determined to consist primarily of olivine, and the metal phase was determined to be 88% Fe and 11% Ni via electron microprobe analysis (Kuva et al., 2017).

Iron meteorites are often characterized with respect to their siderophile element concentrations, which can reveal shared chemical similarities with established groups (e.g., Scott and Wasson, 1973; Pernicka and Wasson, 1987; Dauphas et al., 2002; Walker et al., 2008; McCoy et al., 2011). There are currently 13 iron meteorite groups: IAB-complex, IC, IIAB, IIC, IID, IIE, IIF, IIG, IIIAB, IIIE, IIIF, IVA, and IVB. Each group is further characterized as being "magmatic" or "nonmagmatic", depending on the processes believed to be involved in their formation. Magmatic iron meteorites are largely interpreted

to represent fragments of asteroidal cores, wherein irons within one group can be related through a common crystal-liquid fractionation process. Nonmagmatic iron meteorites have been suggested to form through other processes, such as from the crystallization of localized, impact-induced melts on chondritic precursors (Wasson et al., 1980; Choi et al., 1995; Wasson and Kallemeyn, 2002). Conversely, if an iron meteorite is found to be chemically unrelated to the established groupings, it is therefore considered "ungrouped". There are currently over 100 iron meteorites classified as ungrouped, likely sampling numerous distinct parent bodies.

Both grouped and ungrouped iron meteorites have proven useful in the study of the origins and compositions of the carbonaceous chondrite (CC) and non-carbonaceous (NC) reservoirs of the early solar system. Isotopic heterogeneities have been observed among bulk planetary materials, reflecting a heterogeneous distribution of nucleosynthetic components between the two domains (e.g., Trinquier et al., 2007; Warren, 2011; Fisher-Gödde et al., 2015; Budde et al., 2016; Kruijer et al., 2017). Among these isotopic heterogeneities are those observed in some siderophile elements, particularly Mo, Ru, and W, which have allowed for additional insight into this isotopic dichotomy through the study of iron meteorites (Dauphas et al., 2002; Burkhardt et al., 2011; Fisher-Gödde et al., 2015; Kruijer et al., 2017). As a result, the iron meteorite groups, along with several individual ungrouped irons, have been classified as either NC or CC. Additionally, variable ^{182}W compositions observed between NC and CC iron meteorites have indicated different timescales of metal-silicate segregation and parent body accretion between the two domains (Kruijer et al., 2017). Thus, utilization of the Hf-W chronometer and ^{182}W

compositions in both grouped and ungrouped iron meteorites can provide insight into the accretion and core formation history of a parent body.

The aim of this study is to utilize siderophile element concentrations to assess possible chemical similarities between Lieksa and the established iron meteorite groups in order to accurately classify the find. Additionally, Mo, Ru, and W isotopic compositions are assessed in order to further characterize the meteorite and provide additional insight into the extent of isotopic heterogeneity observed in NC- and CC-type parent bodies, as well as to constrain the timing of metal-silicate segregation on Lieksa's parent body.

3.3 Analytical Methods

3.3.1 Laser Ablation Inductively Coupled Plasma Mass Spectrometry (LA-ICP-MS)

A 13 g chunk of Lieksa was obtained from the Finnish Museum of Natural History. Concentrations of 17 siderophile elements (Re, Os, W, Ir, Mo, Ru, Pt, Rh, Ni, Co, Fe, Pd, As, Au, Cu, Ga, Ge) were obtained on this chunk via laser ablation. The sample was polished with sandpaper of various grit to ensure that one flat surface was removed of rust. Immediately prior to analysis, the sample was ultrasonicated in ethanol to remove any additional contaminants. Siderophile element concentrations were obtained using a *New Wave UP213* ultraviolet laser coupled to a *Thermo Finnigan Element 2* inductively coupled mass spectrometer (ICP-MS). Data were processed using *LAMTRACE* (Rusk, 2009), using known concentrations of in-house laboratory reference iron meteorites Filomena, Hoba, and Coahuila. Five ~5 mm long laser ablation tracks were averaged in order to obtain a

representative composition of the sample, and data normalization was achieved by forcing concentrations of Fe, Ni, and Co to sum to 100% (Walker et al., 2008).

3.3.2 Highly Siderophile Element Analysis

Concentrations of highly siderophile elements (HSE; Re, Os, Ir, Ru, Pt, Pd), as well as ^{187}Re-^{187}Os data were determined following the isotope dilution procedures outlined in Walker et al. (2008). A piece of Lieksa was cut using a *Leco Vari-cut* saw equipped with a diamond sawblade. A piece of carborundum was cut in order to clean the blade prior to sample cutting. The resulting ~70 mg piece was then polished with sandpaper of various grit in order to ensure removal of blade markings and rust. The piece, along with appropriate amounts of a mixed spike containing ^{185}Re-^{190}Os and a separate mixed spike of ^{191}Ir-^{99}Ru-^{194}Pt-^{105}Pd was added to a *Pyrex*® Carius tube, along with 2.5 mL of concentrated HCl and 5 mL of concentrated HNO_3. The tube was sealed and heated at ~220ºC for 48 hours obtain sample-spike equilibrium and oxidation of Os to the higher valence (+8) necessary for extraction. After dissolution, Os was separated using a carbon tetrachloride (CCL_4) extraction method described in Cohen and Waters (1996) and further purified via microdistillation methods outlined in Birck et al. (1997). The resulting purified Os was loaded onto a Pt filament, along with a Ba hydroxide activator, and analyzed by a *Thermo Fisher Triton* thermal ionization mass spectrometer. (TIMS). Osmium isotopic data were corrected for instrumental mass fractionation by normalizing ^{190}Os/^{188}Os to 3.08271 (Allègre and Luck, 1980).

The other HSE within the residual acid were separated and purified via anion exchange column (Rehkämper and Halliday, 1997). Rhenium and Ru were eluted with 12

mL of 6M HNO_3, Pt and Ir were eluted with 13 mL of concentrated HNO_3, and Pd was eluted with 14 mL of concentrated HCl. The Re and Ru aliquot was further purified using a secondary anion exchange column and eluted with 7 mL of 6M HNO_3. Rhenium, Ru, Ir, Pt, and Pd were analyzed using a *Thermo Fisher Neptune Plus* multi-collector ICP-MS. Tungsten was added to the Re aliquots to correct for mass fractionation effects. The blank for this procedure measured 9, 4, 3, 45, 23, and 23 pg for Re, Os, Ir, Ru, Pt, and Pd, respectively. Blank corrections were made but not have a significant impact on final concentrations. Estimated measurement uncertainties for Re and Os are < 0.1% and < 2% for the other HSE.

3.3.3 Molybdenum, Ru, W, Os, and Pt Isotopic Measurements

A ~2 g piece of Lieksa was cut and polished for Mo, Ru, W, Pt, and Os isotopic measurements. The meteorite chunk was dissolved in 8M HCl at ~140ºC for 48 hours in a *Teflon*® beaker. The resulting solution was separated into three aliquots to be processed separately following various methods. One aliquot was processed for Os for the purpose of cosmic ray exposure (CRE) assessment and correction. This was achieved following the same separation and purification techniques described above. Approximately 300 ng of Os was loaded onto a Pt filament along with a Ba hydroxide activator and analyzed using a *Thermo Fisher Triton* TIMS. Osmium isotopic data were corrected for instrumental mass fractionation by normalizing $^{190}Os/^{188}Os$ to 3.08271 (Allègre and Luck, 1980). All isotopic compositions in this study will be reported using the μ notation (e.g., Os):

$$\mu^{189}\mathrm{Os} = \left(\frac{^{189}_{188}\mathrm{Os}_{\mathrm{sample}}}{^{189}_{188}\mathrm{Os}_{\mathrm{standard}}} - 1\right) * 10^6 \qquad \text{(Eq. 3.1)}$$

which corresponds to the part per million deviation of an isotopic ratio of a sample to that of a laboratory standard. Analytical uncertainties were assessed by measuring a standard solution multiple times during the analytical campaign and determining their external reproducibility (2σ). The 2σ for this campaign was ±6 for μ^{189}Os (*n* = 3).

A separate aliquot from the initial dissolution was processed for Mo, W, and Pt isotopic analyses following a scaled-up version of the anion exchange column procedure developed by Nagai and Yokoyama (2014). Tungsten was eluted from the column using 100 mL of 9M HCl + 1M HF, Mo was eluted using 50 mL of 6M HNO_3 + 3M HF, and Pt was eluted using 75 mL of concentrated HNO_3.

After separation via the initial primary column, the Mo aliquot was dried, redissolved in 6M HCl, and loaded onto a secondary primary anion exchange column with ~0.3 mL AG 1 x 8 200-400 mesh resin, following the column procedure described in Worsham et al. (2016). Molybdenum was eluted from the column using 12.5 mL of 1M HCl, dried, and loaded onto the same column a second time to ensure purification. The final Mo aliquot was dried and treated with a 2:1 mixture of concentrated HNO_3 and HCl (100 µL) three times to ensure removal of resin-derived organics. The sample was then redissolved in 6M HCl for loading. Approximately 100 ng of Mo was loaded onto an outgassed Re filament along with 2 µL of a 5 µg/µL $La(NO_3)_3$ activator solution. A second filament was also loaded with 2 µL of the 5 µg/µL $La(NO_3)_3$ activator following the double filament assembly described in Worsham et al. (2016). Molybdenum was analyzed as MoO^-_3 using a *Thermo Fisher Triton Plus* TIMS using a 3-peak jump, multi-dynamic

method (Worsham et al., 2016a). Isotopic data were corrected for instrumental mass fractionation by normalizing $^{98}Mo/^{96}Mo$ to 1.453171 (Lu and Masuda, 1994). The 2σ for this campaign was ±37, ±12, ±8, and ±4 ppm for $\mu^{92}Mo$, $\mu^{94}Mo$, $\mu^{95}Mo$, and $\mu^{97}Mo$, respectively (n = 8).

The W aliquot from the initial primary column was dried, redissolved in 0.6 mL of 0.4M HCl + 0.5M HF, and loaded onto a secondary anion exchange column following methods described in Nagai and Yokoyama (2014), where W is eluted with 2.4 mL of 9M HCl + 3M HF. The eluted solution was dried and treated with HNO_3, HCL, and H_2O_2 multiple times. The purified W aliquot was finally redissolved in 0.4M HCl + 0.5 M HF. Approximately 1000 ng of W was loaded onto an outgassed Re filament along with 1 µL of 5 µg/µL La- 5 µg/µL Gd activator solution and measured as WO^-_3 using a *Thermo Fisher Triton* TIMS. Isotopic data were corrected for instrumental mass fractionation by normalizing $^{186}W/^{184}W$ to 0.92767 (Völkening et al., 1991). The 2σ for this analytical campaign was ± 6 ppm for $\mu^{182}W$ and ± 3 ppm for $\mu^{183}W$ (n = 5).

The Pt aliquot from the same primary column was dried, redissolved in a 2:1 mixture of concentrated HNO_3 and HCl, and refluxed overnight at 100ºC, following the clean-up procedure described in Hunt et al. (2017). The aliquot was then dried and refluxed overnight once more in 1M HCl, then diluted with ascorbic acid and loaded onto an anion exchange column. Platinum was eluted with 15 mL of concentrated HNO_3. This column procedure was repeated once more to ensure complete Pt-Ir separation. Solutions were dried, treated with $HClO_4$, and refluxed overnight in 2:1 HNO_3 and HCl. Samples were dried once more and taken up in 2% HNO_3 to be analyzed on a *Thermo Fisher Neptune Plus* multi-collector ICP-MS. Isotopic data was corrected for instrumental mass

fractionation by normalizing $^{198}Pt/^{195}Pt$ to 0.2145 (Kruijer et al., 2013). The 2σ for this analytical campaign was ± 8 ppm for $\mu^{196}Pt$.

The third and final aliquot from the initial sample digestion was processed for Ru following purification techniques outlined in Bermingham et al. (2016). The aliquot was dried, redissolved in 0.15M HCl, and loaded onto a primary cation column. Ruthenium was eluted with 15 mL of 0.15M HCl and further purified via microdistillation using 0.2 g/mL CrO_3 in 0.5M H_2SO_4 and 4M HBr. The sample was then taken up in 5% HNO_3 and analyzed using a *Thermo Fisher Neptune Plus* multi-collector ICP-MS. Isotopic data were corrected for instrumental mass fractionation by normalizing $^{99}Ru/^{101}Ru$ to 0.745075 (Chen et al., 2010). The 2SD external precision for this analytical campaign, as defined by repeated analyses of the standard, was ± 8 ppm for $\mu^{100}Ru$ (n = 15).

3.4 Results

3.4.1 Bulk Compositional Analysis by LA-ICP-MS and HSE Concentrations

Bulk siderophile element concentrations and their 2σ values determined via LA-ICP-MS are reported in Table 3.1. The siderophile element data, normalized to CI-chondrites, are shown in Figure 3.1. Lieksa exhibits a moderate depletion in the volatile siderophile elements (e.g., Ga and Ge) relative to the more refractory siderophile elements (e.g., Mo and W). Lieksa plots closest to the field defined by the group IVA irons in terms of its Ga concentration (Figure 3.2), but is more similar to the group IID or IIF irons in terms of its Ge concentration (Figure 3.3), indicating that Lieksa cannot be classified as

Figure 3.1 Average siderophile element concentrations for Lieksa obtained via LA-ICP-MS. Iron, Ni, and Co concentrations reported in wt.%. All others reported in ppm.

n	5
Re	0.6 ± 0.1
Os	7.3 ± 0.8
W	1.6 ± 0.9
Ir	7.2 ± 1.3
Mo	13.3 ± 4.3
Ru	9.1 ± 0.8
Pt	12.9 ± 1.5
Rh	1.4 ± 0.2
Ni	10.6 ± 1.6
Co	0.7 ± 0.1
Fe	88.6 ± 2.4
Pd	2.9 ± 1.1
As	4.8 ± 0.6
Au	1.4 ± 1.9
Ga	2.1 ± 0.7
Ge	58.1 ± 0.3

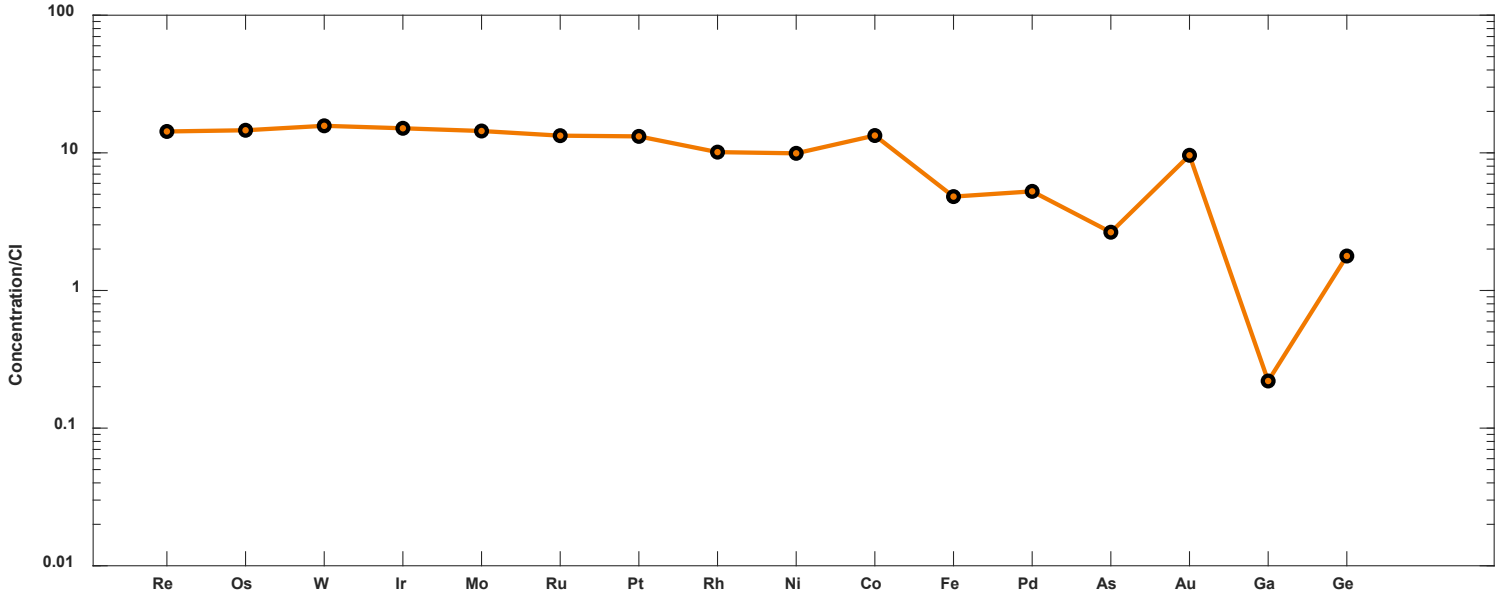

Figure 3.1 Bulk siderophile element concentrations normalized to CI-chondrite for Lieksa obtained via LA-ICP-MS Normalizing data are from Lodders (2003). Elements are listed in order of decreasing condensation temperature from left to right.

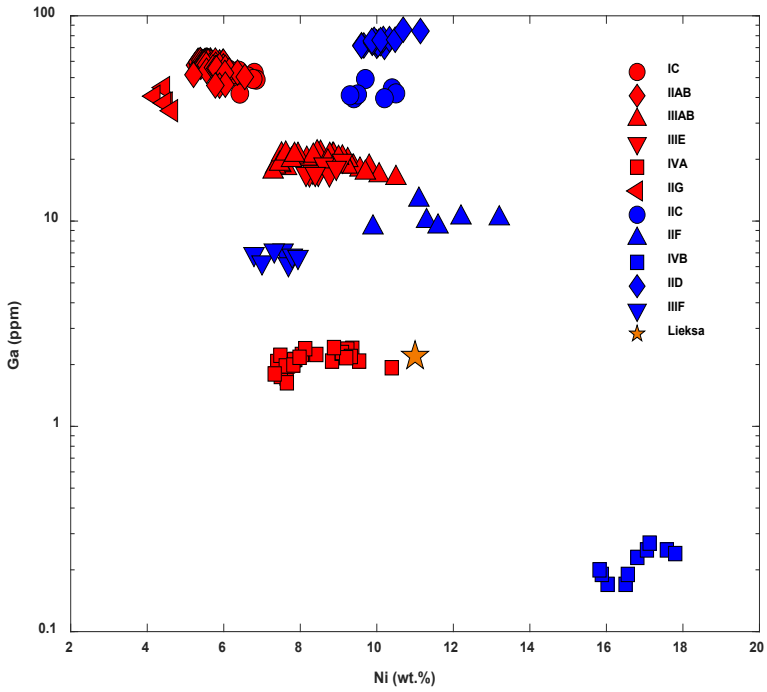

Figure 3.2 Compilation of Ga (ppm) vs. Ni (wt.%) for the magmatic iron meteorite groups and Lieksa. Red symbols are NC-type meteorites and blue symbols are CC-type meteorites. Lieksa is represented with an orange star. Group data compiled from Schaudy et al. (1972), Scott and Wasson (1973), Buchwald (1975), Scott and Wasson (1976), Wasson and Huber (2006), Wasson et al. (2007), Wasson and Choe (2009), Hilton et al. (2020), and Tornabene et al. (2020).

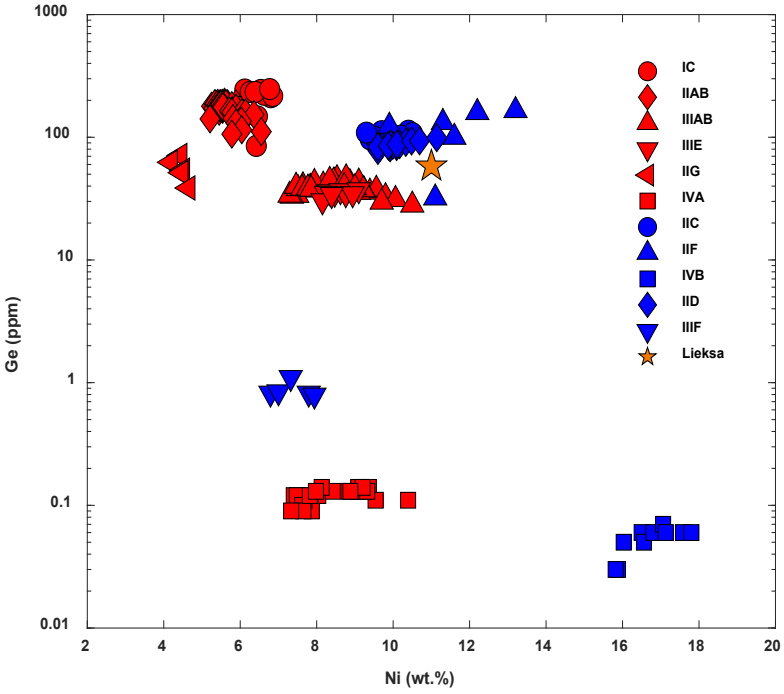

Figure 3.3 Compilation of Ge (ppm) vs. Ni (wt.%) for the magmatic iron groups and Lieksa. Symbology and source materials are the same as in Figure 3.2.

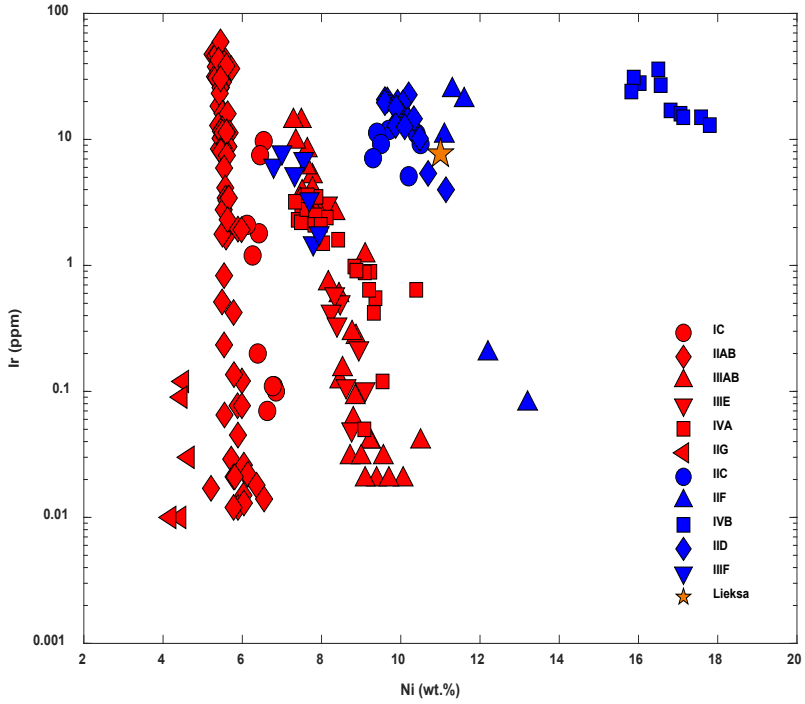

Figure 3.4 Compilation of Ir (ppm) vs. Ni (wt.%) for the magmatic iron groups and Lieksa. Symbology and source materials are the same as in Figure 3.2.

belonging to a magmatic iron group based on its volatile siderophile element concentrations alone. Lieksa plots near the IID and IIF fields in terms of Ir concentration as well (Figure 3.4). Highly siderophile element concentrations and Re-Os isotopic data for a bulk sample of Lieksa are reported in Table 3.2. Lieksa exhibits a flat chondrite-normalized HSE pattern, with a slight depletion in Pd, similar to patterns exhibited by relatively unfractionated irons from some of the established groups (Figure 3.5).

Table 3.2 Highly siderophile element concentrations and Re-Os isotopic data for Lieksa.

	Wt. (g)	Re	Os	Ir	Ru	Pt	Pd	$^{187}Re/^{188}Os$	2σ	$^{187}Os/^{188}Os$	2σ
Lieksa	0.0727	601.6	7991	7768	10240	13760	3445	0.3625	0.0004	0.1245	0.00012

All concentrations are in ppb.

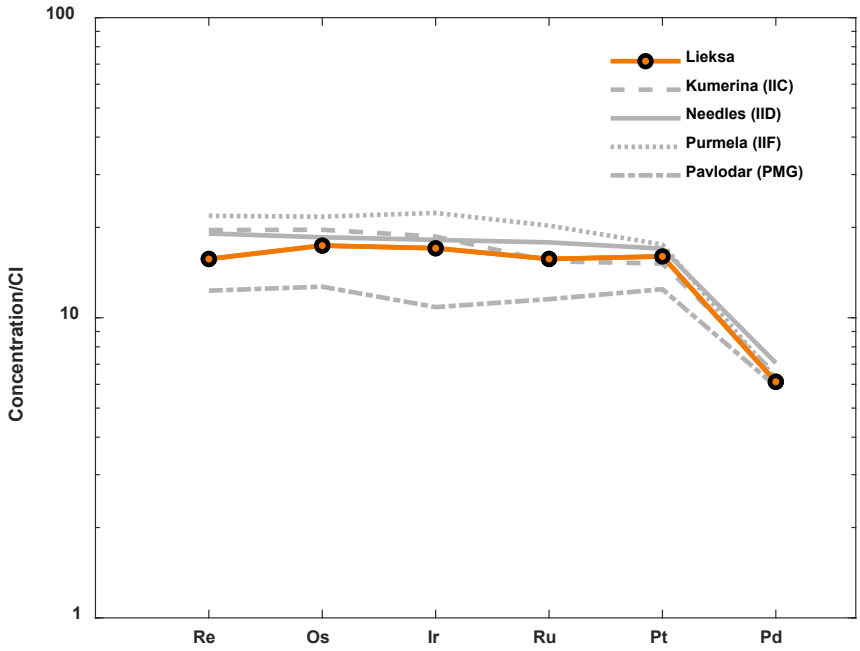

Figure 3.5 CI-chondrite normalized HSE concentrations for Lieksa obtained via isotope dilution. Irons with similar HSE abundances from the IIC, IID, and IIF groups are included for comparison. The main group pallasite (PMG) Pavlodar is also included. Bulk composition data were normalized to concentrations obtained for the CI-chondrite Orguiel (Horan et al., 2003).

3.4.3 Platinum and Os Isotopic Compositions

Platinum and Os isotopic data were obtained in order to correct for possible cosmic ray exposure (CRE) effects. Cosmic ray exposure can result in neutron capture reactions in iron meteorites, thereby modifying a meteorite's Mo, Ru, and W isotopic composition (Wittig et al., 2013; Kruijer et al, 2013). These effects can be monitored and corrected for through utilization of Pt and Os dosimeters, as μ^{196}Pt and μ^{189}Os values are expected to increase and decrease with continued cosmic ray flux, respectively. Platinum and Os isotopic compositions for Lieksa are reported in Table 3.3. Lieksa has a μ^{196}Pt value of 7 ± 8 (n = 3) and a μ^{189}Os value of -3 ± 6 (n = 4). Neither isotopic composition displays resolvable deviation from the laboratory standards, indicating that the isotopic data reported here do not require correction for CRE effects.

Table 3.3 Platinum and Os isotopic compositions of Lieksa.

	n	$\mu^{196}Pt$	±	*n*	$\mu^{189}Os$	±
Lieksa	3	+7	8	4	-3	6

n is number of analyses. Uncertainties reflect the 2SD of the standards run during each analytical campaign.

Table 3.4 Molybdenum and Ru isotopic compositions for Lieksa.

	n	$\mu^{92}Mo$	±	$\mu^{94}Mo$	±	$\mu^{95}Mo$	±	$\mu^{97}Mo$	±	$\mu^{100}Mo$	±	*n*	$\mu^{100}Ru$	±
Lieksa	3	75	37	79	12	37	8	24	4	5	20	3	-55	8

n is number of analyses for Mo and Ru isotopic composition. Uncertainties reflect the 2SD of the standards run during an analytical campaign.

Table 3.5 Tungsten isotopic composition for Lieksa.

	n	$\mu^{182}W_{Measured}$	±	$\mu^{183}W_{Measured}$	±	ΔT_{CAI}	±
Lieksa	2	-332	6	1	3	1.5	0.8

n is number of analyses. Uncertainties reflect 2SD of the standards run during the analytical campaign.

3.4.4 Molybdenum, Ru, and W Isotopic Compositions

Molybdenum, Ru, and W isotopic data for Lieksa are reported in Table 3.4 and Table 3.5. The μ^{92}Mo, μ^{94}Mo, μ^{95}Mo, μ^{97}Mo, μ^{100}Mo values for Lieksa are 75 ± 37, 79 ± 12, 37 ± 8, 24 ± 4, and 5 ± 20 respectively. The μ^{183}W value determined for Lieksa is 1 ± 3, and the μ^{182}W value determined is -332 ± 6. The μ^{100}Ru value determined for Lieksa is -55 ± 8.

3.5 Discussion

3.5.1 Genetics

Molybdenum, Ru, and W isotopic heterogeneities recorded in iron meteorites have been attributed to the heterogenous accretion of isotopically diverse precursor materials, composed of variable amounts of *p-, r-,* and *s*-process nuclides. These heterogeneities are utilized in assessing a meteorite's genetic heritage and in classifying meteorites or meteorite groups as belonging to the NC- or CC-type meteorite classification scheme. These heterogeneities are also useful in relating individual meteorites to already established groups. The Mo isotopic composition obtained for Lieksa falls within the range of compositions established by previously studied NC-type meteorites (Figure 3.6). Noncarbonaceous-type meteorites exhibit Mo isotopic compositions characterized by *s*-process depletions and *r*-process enrichments relative to terrestrial standards, although not as strong as those observed in CC-type meteorites (Budde et al, 2019; Spitzer et al., 2020). Additionally, NC-type meteorites are also characterized by a linear Mo-Ru relationship, as seen on previously published μ^{97}Mo vs. μ^{100}Ru and μ^{92}Mo vs. μ^{100}Ru plots (Dauphas et al., 2004; Fischer-Gödde et al., 2015;

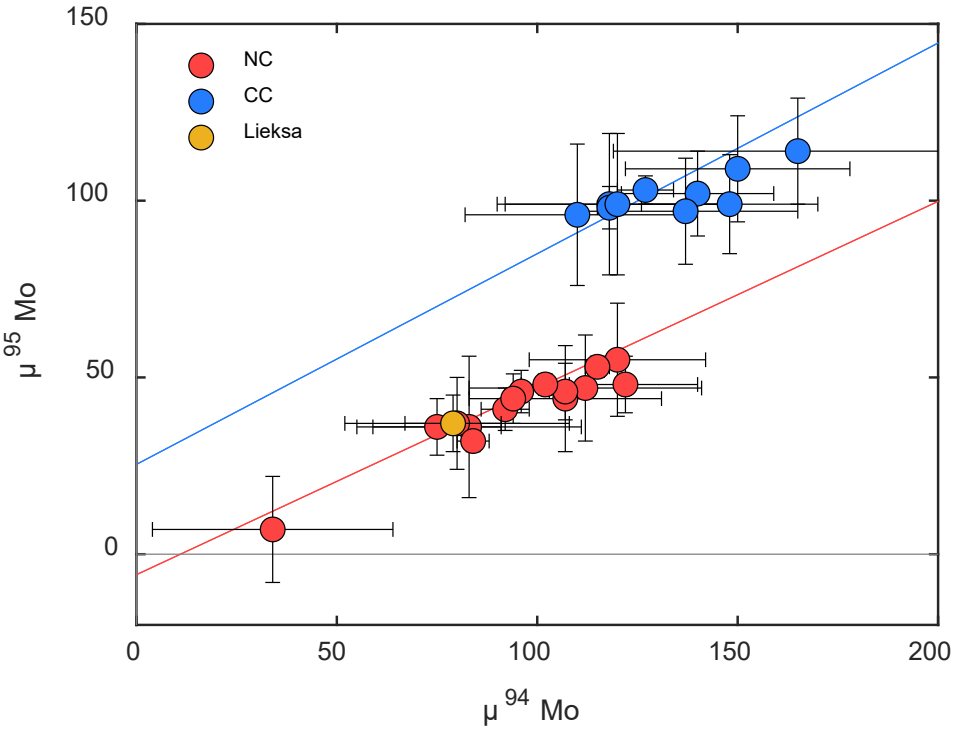

Figure 3.6 Compilation of μ^{94}Mo vs. μ^{95}Mo data for iron meteorites. Data compiled from Bermingham et al. (2018), Worsham et al. (2019), and Hilton et al. (2019b). Blue symbols represent CC-type iron meteorites (IIC, IID, IIF, IIIF, IVB, South Byron Trio, Wiley, Dronino, Tishomingo, and Chinga). Red symbols represent NC-type iron meteorites (IC, IIAB, IIIAB, IIIE, IVA, and Gebel Kamil). Red and blue lines represent NC and CC lines reported by Spitzer et al. (2020) and Budde et al. (2019), respectively. The datum for Lieksa is represented by the orange circle.

Tornabene et al., 2020). By contrast, CC-type meteorites do not exhibit this correlation. The μ^{100}Ru value obtained for Lieksa falls along the trend established by NC-type meteorites (Figure 3.7). Further, the μ^{183}W obtained here is similar to that of the terrestrial standard, which is also characteristic of NC-type meteorites (Figure 3.8; Kruijer et al., 2017). Taken together, the combined Mo, Ru, and W data reported here indicate that Lieksa is an NC-type meteorite.

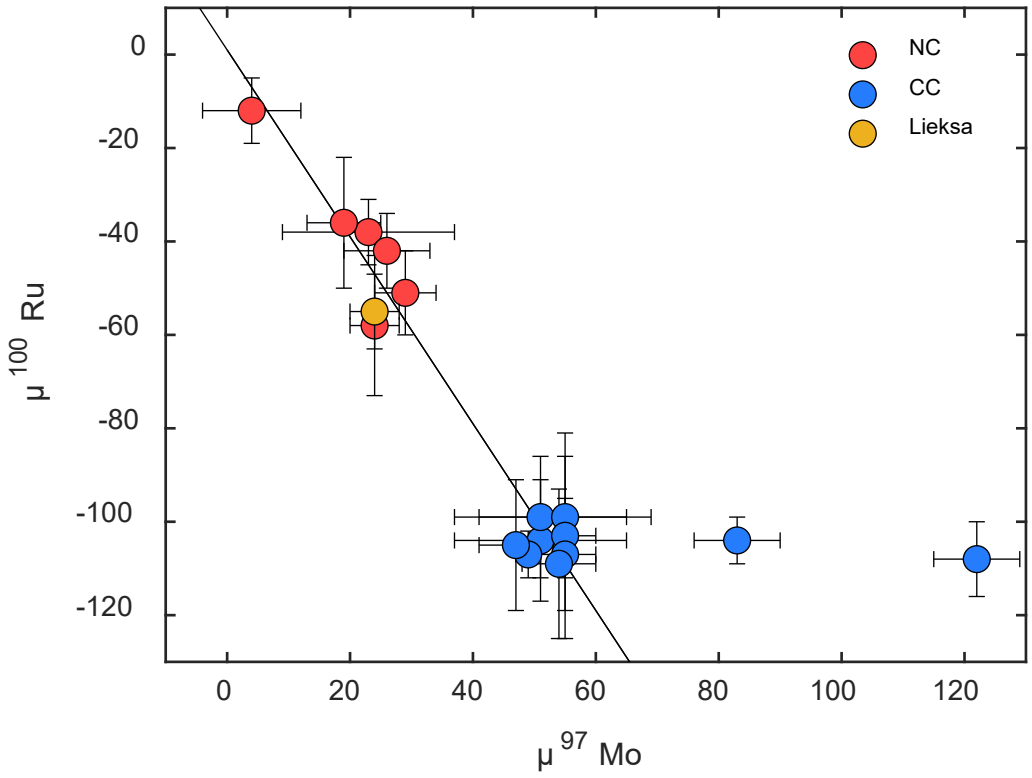

Figure 3.7 Plot of μ^{97}Mo and μ^{100}Ru for iron meteorites. Data compiled from Worsham et al. (2019), Bermingham et al. (2018), and Hilton et al. (2019b). Blue symbols represent CC-type iron meteorites (IID, IIF, IIIF, IVB, South Byron Trio, and the ungrouped iron meteorites Dronino, Tishomingo, and Chinga). Red symbols represent NC-type iron meteorites (IC, IIAB, IIIAB, IVA, and the ungrouped iron meteorite Gebel Kamil). The black line represents the regression of the Mo-Ru correlation from Bermingham et al. (2018). The datum from this study for Lieksa is also plotted, represented by the orange circle.

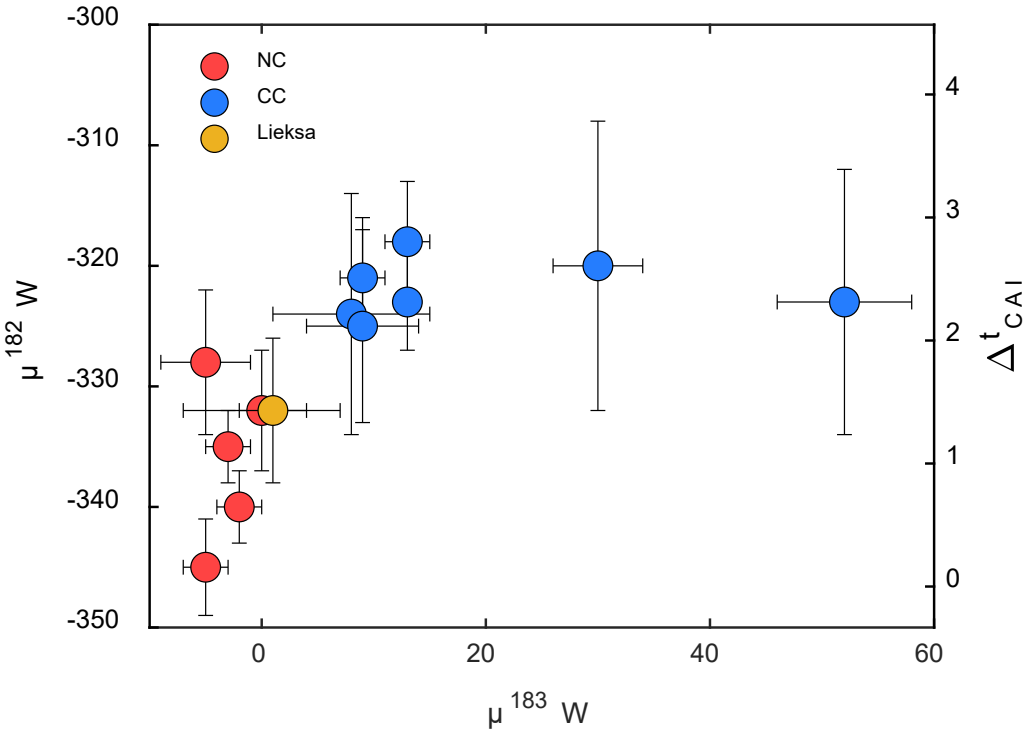

Figure 3.8 Plot of $\mu^{183}W$ vs. $\mu^{182}W$ values of magmatic iron meteorite groups. Right y-axis represents time of metal-silicate segregation, relative to CAI formation, in Myr. Data compiled from Kruijer et al. (2017) and Hilton et al. (2019b). Blue symbols represent CC-type iron meteorites (IIC, IID, IIF, IIIF, IVB, South Byron Trio, and Wiley). Red symbols represent NC-type iron meteorites (IC, IIAB, IIIAB, IIIE, and IVA). Data from this study for the IIIE irons and Aletai are also plotted, represented by the pink and black triangles, respectively. The datum for Lieksa is represented by the orange circle.

3.5.2 Siderophile Element Abundances

Iron meteorites have been commonly classified based on concentrations of Ir and Ni, and the volatile siderophile elements Ga and Ge, as well as textural characteristics and accessory phases (e.g., Scott and Wasson, 1973; Wasson and Wai, 1976). Concentrations of these elements vary widely across iron meteorite groups, and have led to the establishment of four distinct group classifications, numbered I-IV, in order of decreasing volatility (Figures 3.2 and 3.3). In terms of Ga content, Lieksa seems to be a possible extension of the field established by the group IVA irons (Figure 3.2). However, this is not seen in terms of Ge content, where instead Lieksa is most similar to the group IIF and IID irons (Figure 3.3). Similarly, Lieksa exhibits an Ir concentration most like the group IIF and IID irons (Figure 3.4). As Ir concentrations are expected to decrease through a group as fractional crystallization proceeds, the fact that Lieksa plots within the fields established by the IIF and IID irons would allow for Lieksa to sample the same crystallization sequence. Still, Ga, Ge, and Ir concentrations do not indicate a clear group classification on their own.

A comparison of Lieksa's siderophile element abundances to those of the magmatic iron groups and the nonmagmatic IAB complex are provided in Figures 3.9 to 3.13. Laser ablation data for the group IIAB and IIIAB irons, as well as the main group pallasites (PMG), were not readily available and are thus not included. Lieksa shares a number of similarities with some iron meteorite groups. For example, it exhibits refractory siderophile element (e.g., Ni, Co, Mo, W) abundances similar to those of the group IIC, IID, and IIF irons. As these elements have partition coefficients close to 1, they would not be expected to vary dramatically within one group. These similarities also extend to their HSE patterns,

with Lieksa revealing a pattern similar to that of the more minimally fractionated members of the three groups (Figures 3.14 – 3.16). Taken alone, the nested HSE patterns exhibited for the three groups, with the addition of Lieksa, could possibly allow for Lieksa to sample the same crystallization sequence. Further, in addition to having a Ge concentration near that of the IIF irons, Lieksa also exhibits a normalized Ge abundance that is higher than its normalized Ga abundance – a feature that is not seen in any of the magmatic iron groups apart from the IIF irons.

Despite similarities that may be shared with some of the established iron meteorite groups, the overall siderophile element pattern for Lieksa is still noticeably different. Lieksa exhibits a flatter overall pattern across most refractory siderophile elements, as well as a Ge/Ga ratio of 28 compared to the average group ratios of 2, 1, and 12 for the IIC, IID, and IIF irons, respectively. These differences lead to significant crossing between siderophile element and HSE patterns and indicate that Lieksa is too chemically distinct to belong to any of the established iron meteorite groups. Additionally, Lieksa's NC-type genetic heritage does not allow for it to sample CC-type parent bodies, further distinguishing it from the IIC, IID, and IIF groups.

While this study focuses primarily on comparing Lieksa to the established iron meteorite groups, it's classification as a pallasite cannot be ruled out. Lieksa's HSE pattern is similar to that of the main group pallasite (PMG) Pavlodar (Figures 3.5, 3.16). Additionally, the genetic data for Lieksa reported here are consistent with Mo and W isotopic compositions reported by Kruijer et al. (2022) for the PMG. Siderophile element data for the PMG is limited however, and additional siderophile element and isotopic analyses would be necessary to confirm Lieksa's relationship to the PMG.

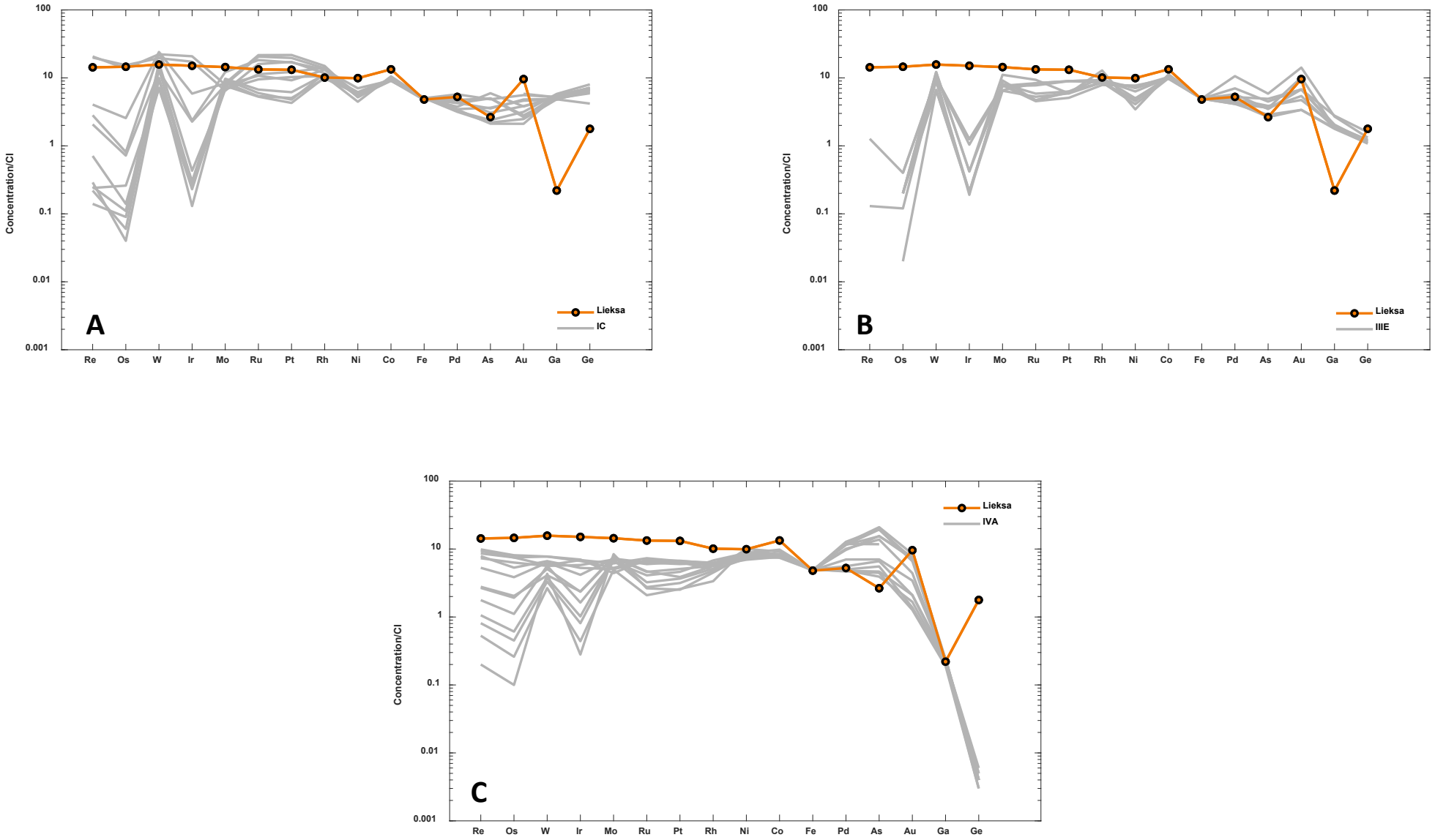

Figure 3.9 CI-chondrite normalized siderophile element abundances of Lieksa compared to group IC (a), IIIE (b), and IVA (c) iron meteorites. All data were obtained via LA-ICP-MS. Elements are arranged in order of decreasing 50% condensation temperature from left to right. Group data compiled from Tornabene et al. (2022; in review), McCoy et al. (2011), and chapter 2 of this thesis.

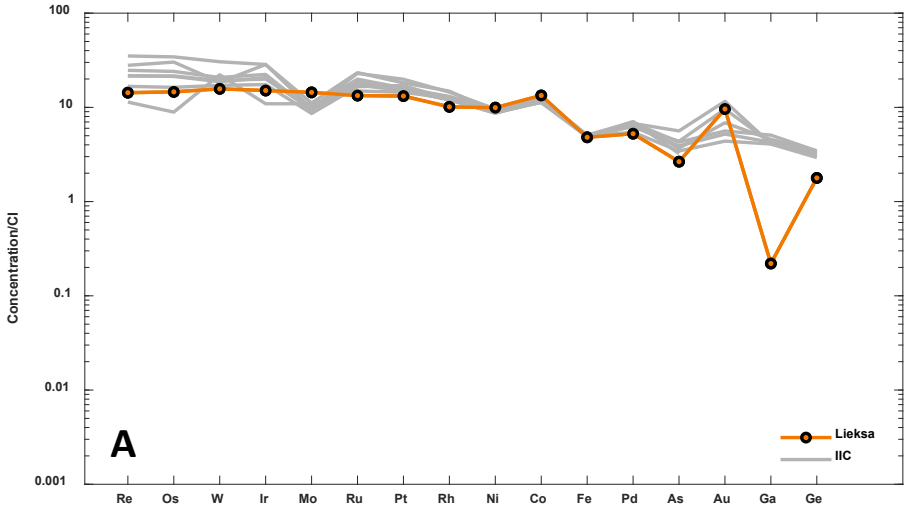

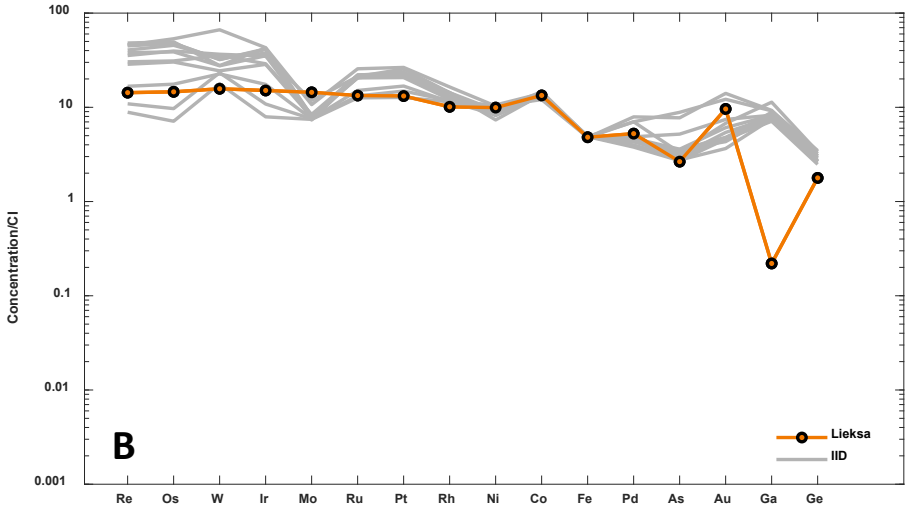

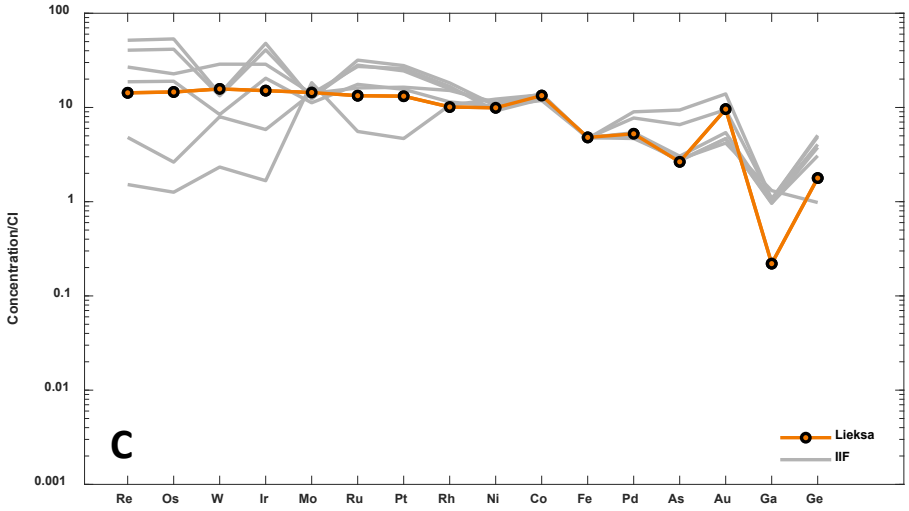

Figure 3.10 CI-chondrite normalized siderophile element abundances of Lieksa compared to group IIC (a), IIID (b), and IIF (c) iron meteorites. All data were obtained via LA-ICP-MS. Elements are arranged in order of decreasing 50% condensation temperature from left to right. Group data compiled from Tornabene et al. (2020), Hilton et al. (2020), and unpublished data.

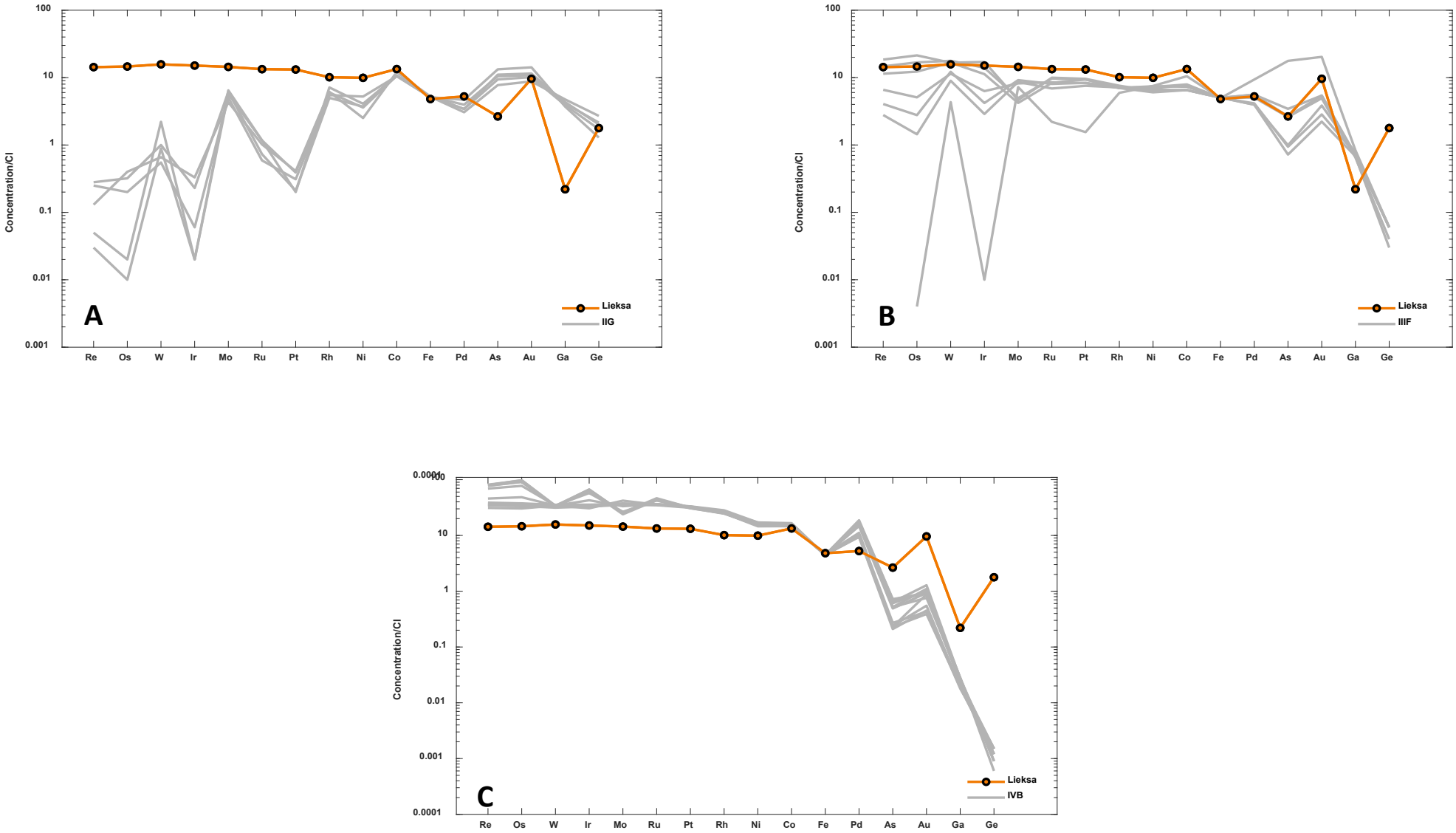

Figure 3.11 CI-chondrite normalized siderophile element abundances of Lieksa compared to group IIG (a), IIIF (b), and IVB (c) iron meteorites. All data were obtained via LA-ICP-MS. Elements are arranged in order of decreasing 50% condensation temperature from left to right. Group data compiled from Walker et al. (2008), Hilton et al. (2019a), and unpublished data. Note different scale for group IVB comparison.

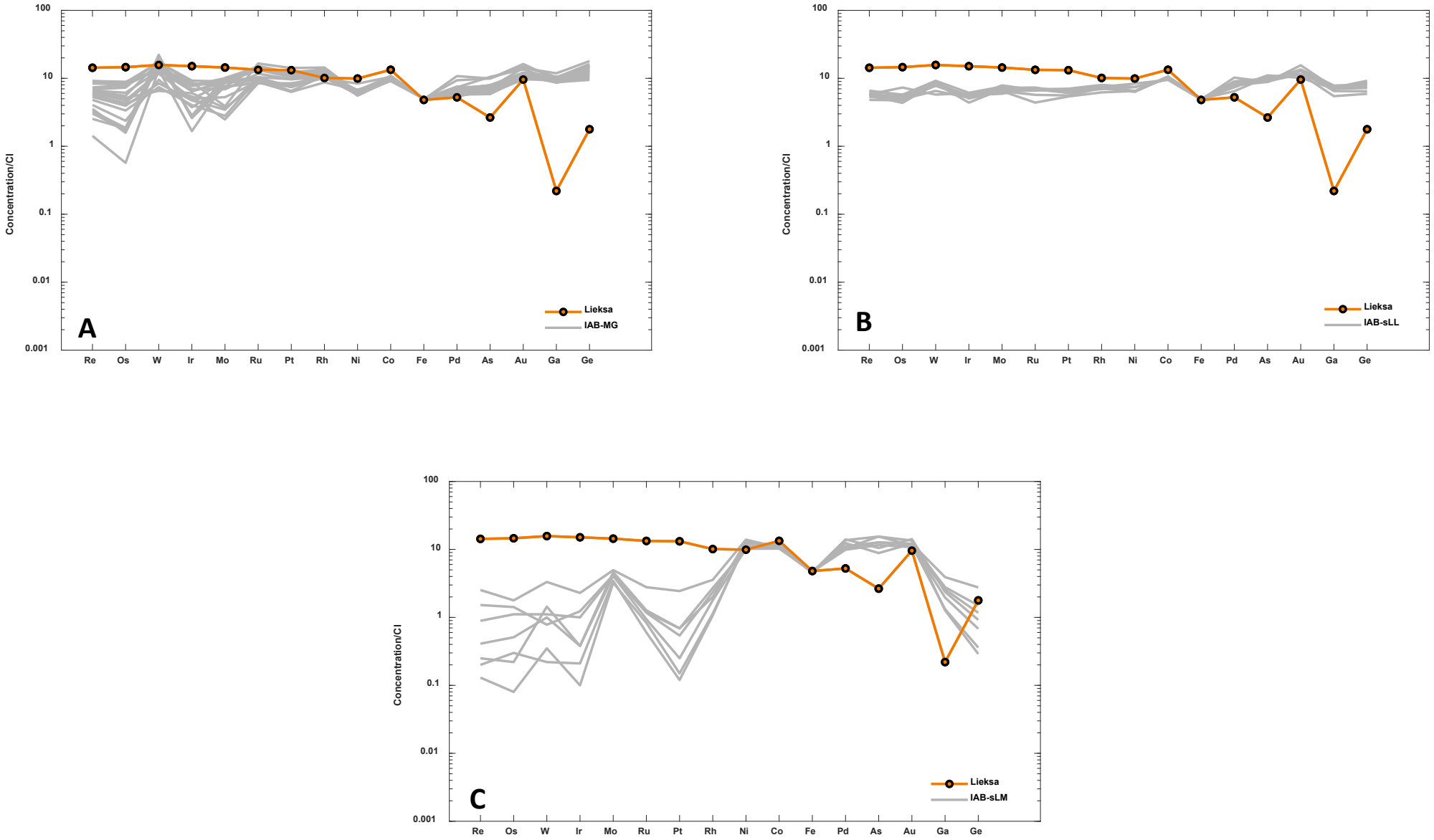

Figure 3.12 CI-chondrite normalized siderophile element abundances of Lieksa compared to IAB complex subgroups MG (a), sLL (b), and sLM (c). All data were obtained via LA-ICP-MS. Elements are arranged in order of decreasing 50% condensation temperature from left to right.

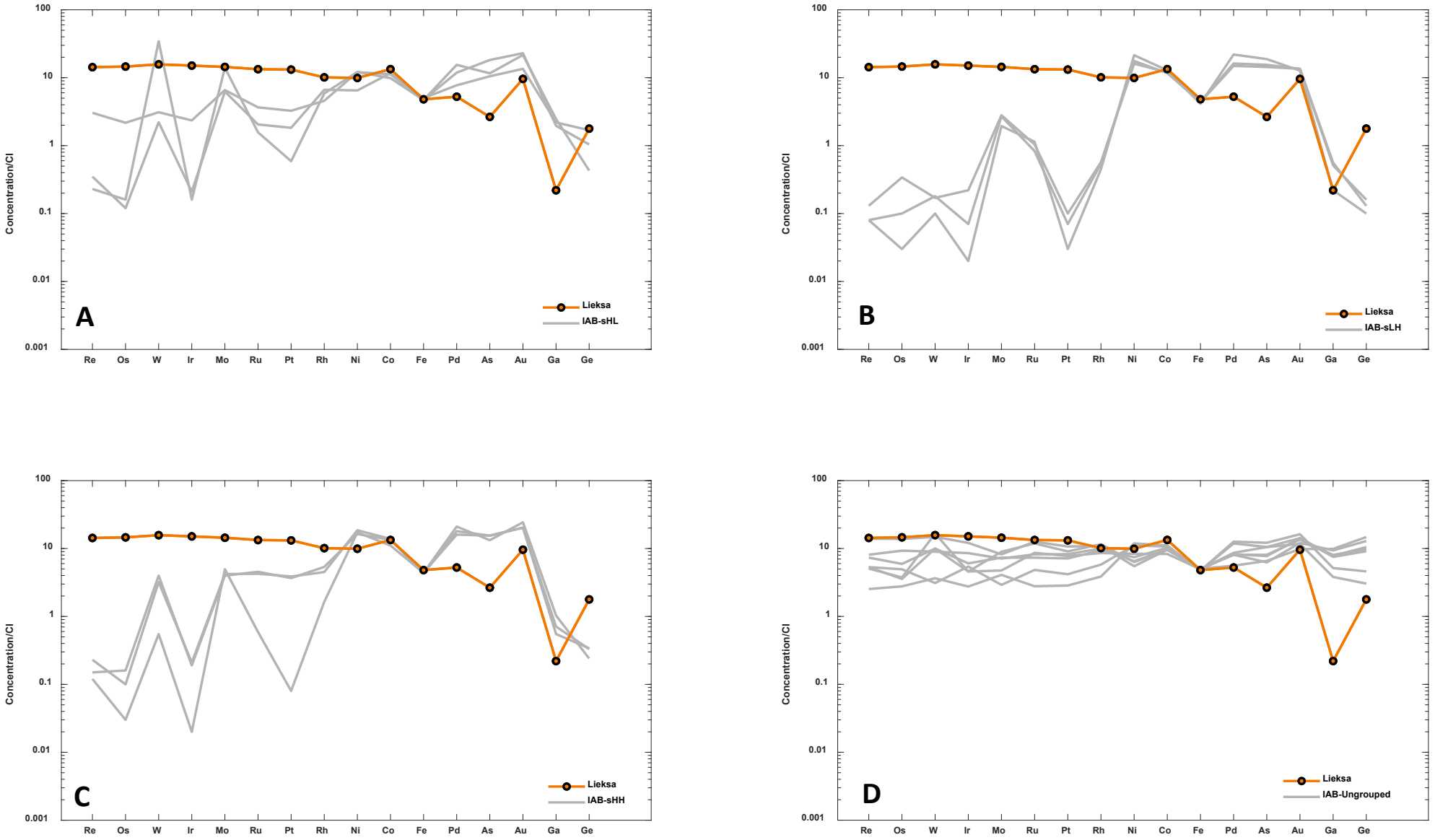

Figure 3.13 CI-chondrite normalized siderophile element abundances of Lieksa compared to IAB complex subgroups sHL (a), sLH (b), sHH (c), and ungrouped (d). All data were obtained via LA-ICP-MS. Elements are arranged in order of decreasing 50% condensation temperature from left to right.

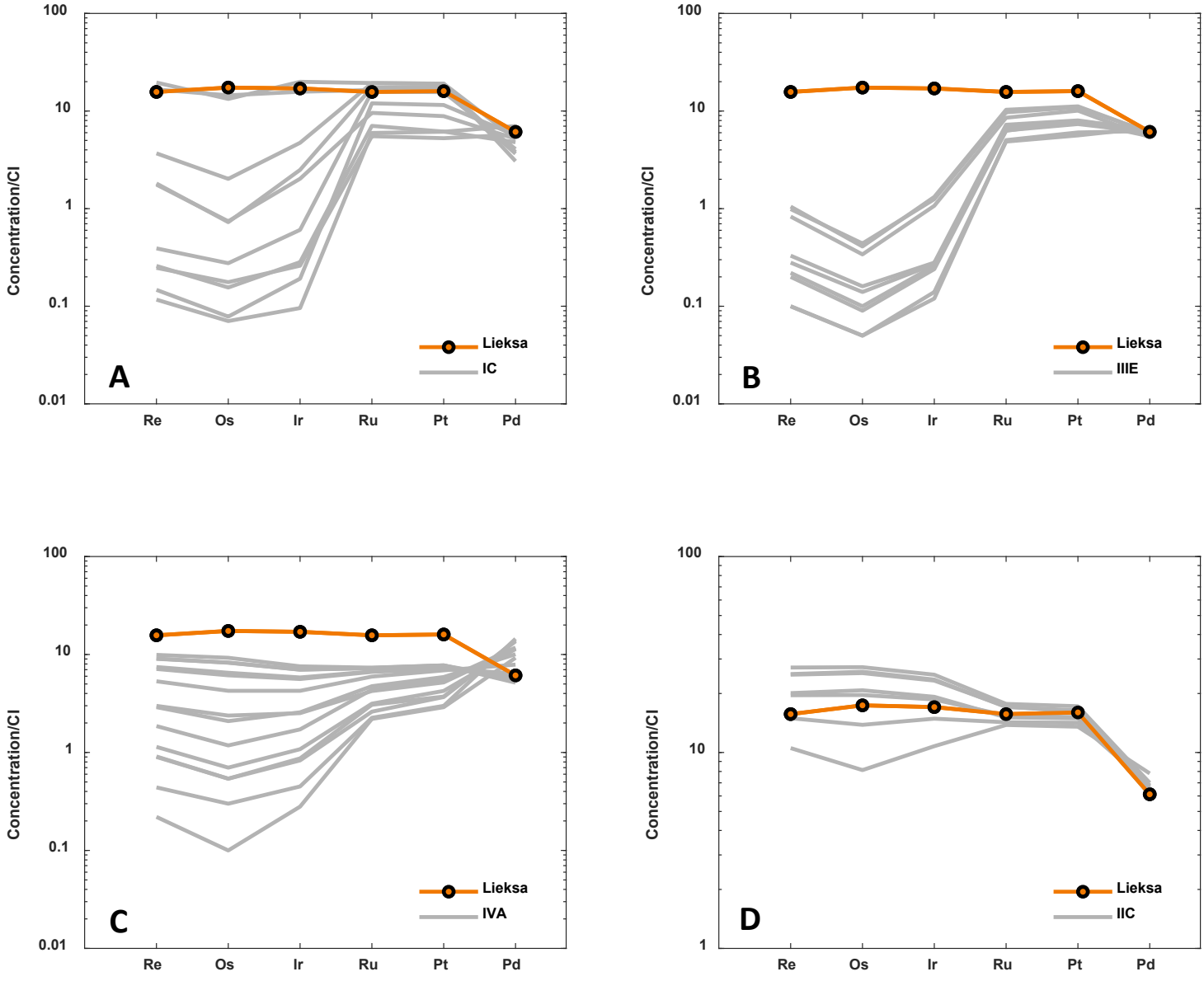

Figure 3.14 CI-chondrite normalized HSE abundances of Lieksa compared to group IC (a), IIIE (b), IVA (c), and IIC (d) iron meteorites. All data were obtained via isotope dilution. Data compiled from McCoy et al. (2011), Tornabene et al. (2020), Tornabene et al. (2022; in review), and chapter 2 of this thesis. Note differences in scale.

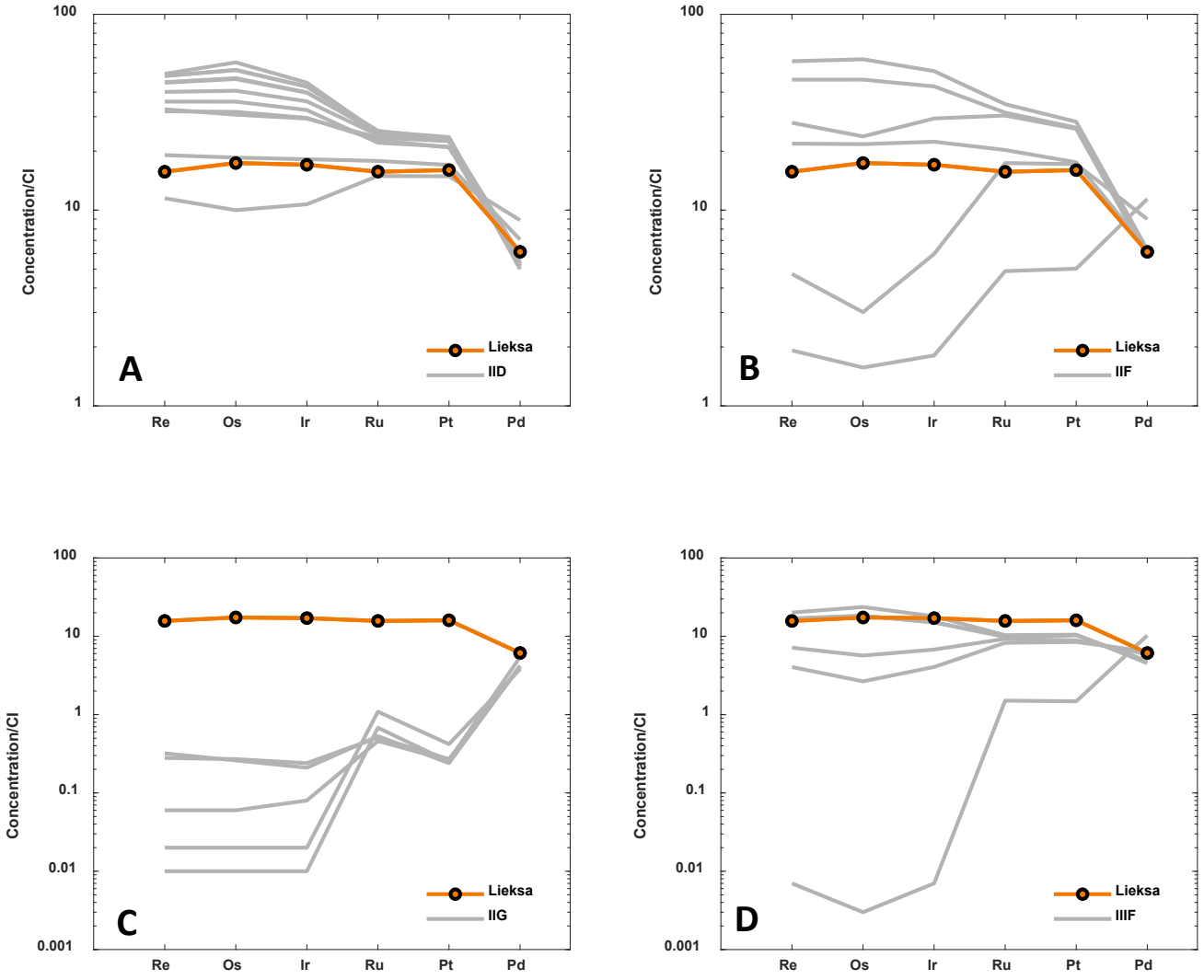

Figure 3.15 CI-chondrite normalized HSE abundances of Lieksa compared to group IID (a), IIF (b), IIG (c), and IIIF (d) iron meteorites. All data were obtained via isotope dilution. Data compiled from Hilton et al. (2020) and Hilton et al. (2022). Note differences in scale.

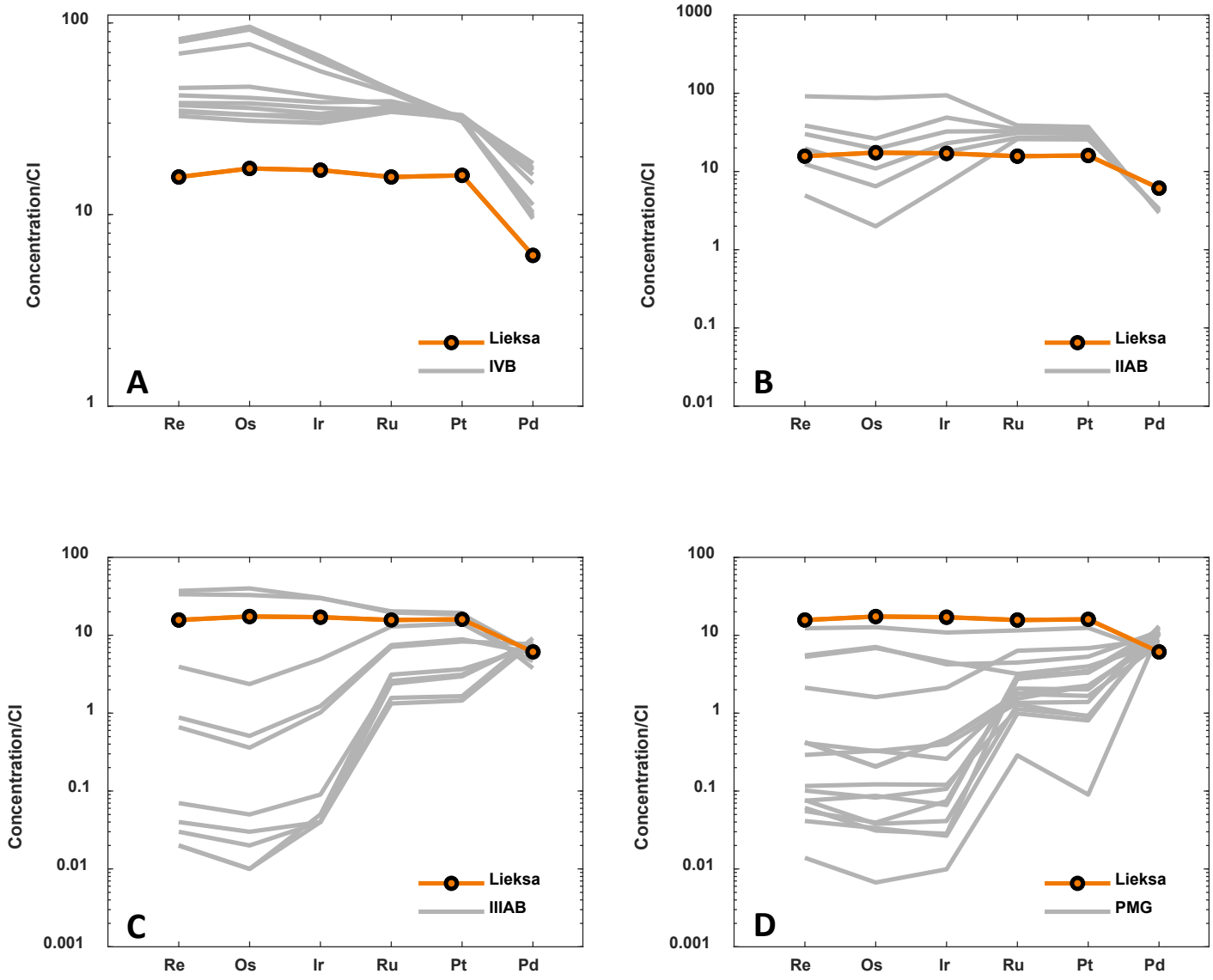

Figure 3.16 CI-chondrite normalized HSE abundances of Lieksa compared to group IVB (a), IIAB (b), and IIIAB (c) iron meteorites and main group pallasites (d). All data were obtained via isotope dilution. Data compiled from Walker et al. (2008), Hilton et al. (2022), and unpublished data. Note differences in scale.

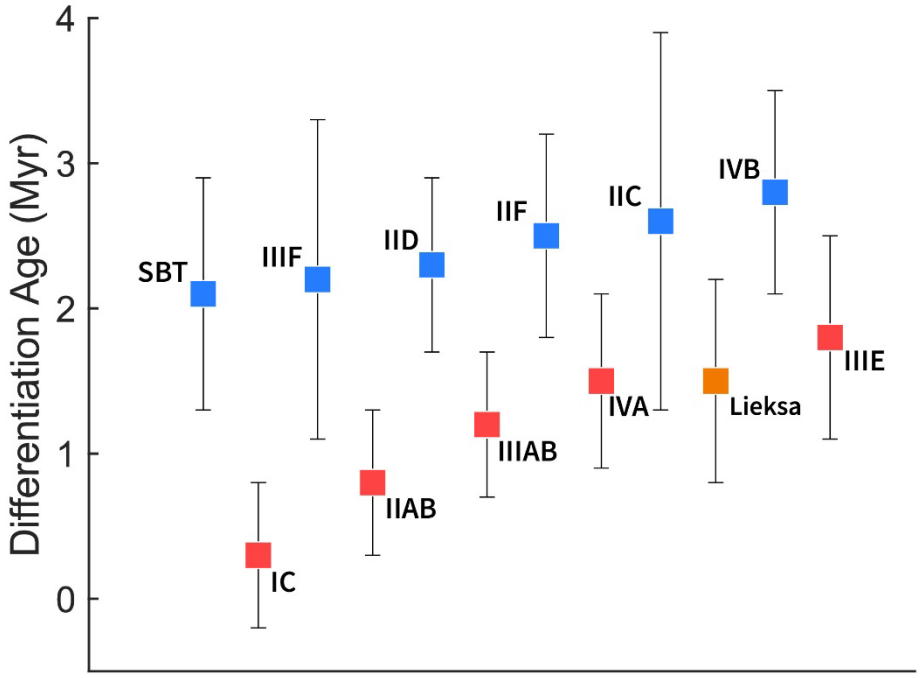

Figure 3.17 Tungsten model core formation ages in Myr relative to CAI formation. Blue symbols represent CC-type iron meteorite parent bodies (South Byron Trio (SBT), IIIF, IID, IIF, IIC, IVB), and red symbols represent NC-type bodies (IC, IIAB, IIIAB, IVA, IIIE). Orange symbol represents Lieksa. All data with the exception of Lieksa are from Kruijer et al. (2017) and Hilton et al. (2019b).

3.5.3 Core Formation Age

The ^{182}Hf-^{182}W ($t_{1/2}$ = 8.9 Myr; Vockenhuber et al., 2004) system is often utilized in the study of iron meteorites in order to assess metal-silicate segregation timescales. Application of the system is based on the moderately siderophile nature of W and the lithophile nature of Hf. Due to their respective partitioning behaviors, as metal-silicate segregation proceeds, Hf will remain in the silicate portion of the melt, while W preferentially partitions into the metallic portion of the melt. At this point, no more ^{182}W can be produced in the core due to the absence of ^{182}Hf, and the ^{182}W isotopic composition

recorded in iron meteorites therefore reflects the ^{182}W composition at time of metal-silicate segregation. A model core formation age can then be calculated using Eq. 3.2, using the present-day chondritic $\mu^{182}W$ value of -191 ± 8 (Kleine et al., 2004), and the $\mu^{182}W$ value of CAI, -349 ± 7, which is used as a proxy for W composition of the initial solar system (Kruijer et al., 2014).

$$\Delta T_{CAI} = -\frac{1}{\lambda} \ln \left[\frac{(\mu^{182}W)_{sample} - (\mu^{182}W)_{chondrite}}{(\mu^{182}W)_{CAI} - (\mu^{182}W)_{chondrite}}\right] \quad \text{Eq. 3.2}$$

The average $\mu^{182}W$ value recorded by Lieksa is -332 ± 6, which corresponds to a model core formation age of 1.5 ± 0.8 Myr after CAI (Figure 3.8). This age falls within the range established by other NC-type iron meteorite parent bodies and overlaps within uncertainties with all other NC- and CC-type bodies (Figure 3.12).

3.6 Conclusions

1) Platinum and Os isotopic compositions indicate that Lieksa underwent minimal cosmic ray exposure, and as such, its genetic isotopic compositions have not been altered and do not require correction.
2) Nucleosynthetic Mo, Ru, and W isotopic compositions indicate that Lieksa is an NC-type meteorite.
3) Radiogenic ^{182}W values indicate that the parent body Lieksa samples underwent metal-silicate segregation at 1.5 ± 0.8 Myr after CAI formation.

4) Lieksa exhibits a remarkably flat siderophile element pattern, with moderate depletions in volatile siderophile elements. The iron also shows a flat HSE pattern, with a slight depletion in Pd, suggesting it to be an early-formed crystallization product from the system it samples. Overall, Lieksa exhibits bulk chemical characteristics that are distinct from groups discussed here, indicating that it does not belong to any of the established iron meteorite groups.
5) The classification of Lieksa as a pallasite cannot be ruled out. Lieksa's genetics are similar to those of the PMG, and it's HSE pattern is similar to that of Pavlodar's. Additional siderophile element and isotopic analyses would be necessary to confirm this relationship.

Chapter 4: Research Conclusions

The focus of this thesis has been on (1) the crystallization sequence, genetics, and age of the group IIIE iron meteorites and their relation to the formation and evolution of the IIIE parent body, and (2) siderophile element characteristics, genetics, age, and classification of the recently found meteorite Lieksa. Overall, this investigation has contributed new chemical and isotopic data to discussion surrounding the chemical composition and evolution of the early solar system.

The siderophile element abundances of ten IIIE irons meteorites have revealed a moderate depletion in volatile siderophile elements, consistent with their group III classification. Bulk HSE concentrations obtained via isotope dilution have revealed additional depletions in Re, Os, and Ir across all samples, suggesting moderate fractionation. Highly siderophile element concentrations also indicate that the anomalous IIIE iron, Aletai, likely does not sample the same crystallization sequence as the other irons examined here. Subsequent fractional crystallization modeling suggests that the remaining nine irons can be related to one another through a common fractional crystallization process, with a parent melt containing initial S, P, and C concentrations of 12 wt.%, 1.8 wt.%, and 0.15 wt.%, respectively, and HSE concentrations approximately 6 times higher than that of average carbonaceous chondrites. Aletai cannot be related to the other irons under the conditions of this model, providing further evidence that it formed via a separate crystallization process.

Cosmic ray exposure-corrected genetic Mo, Ru, and W isotopic compositions indicate that the IIIE irons and Aletai are NC-type meteorites. This is consistent with previously reported isotopic data for the IIIE irons. Genetic data had not been previously

reported for Aletai, but the data reported here indicate that, while Aletai may not sample the same crystallization sequence as the IIIE irons, it does originate from the same nebular domain. Molybdenum, Ru, and W data for Lieksa also indicate that it is an NC-type meteorite, and thus samples the same domain as the IIIE irons and Aletai. Additionally, Hf-W chronology reveals that the IIIE irons, Aletai, and Lieksa underwent metal-silicate segregation on a similar timescale, within ~2 Myr of solar system formation.

The siderophile element data obtained for Lieksa are distinct from that of the established magmatic and nonmagmatic iron meteorite groups. Lieksa exhibits a flat siderophile and highly siderophile element pattern, as well as depletions in the volatile siderophile elements that differs from most other iron meteorite groups. Taken together, Lieksa's siderophile element characteristics and nucleosynthetic history indicate that it does not belong to any of the established iron meteorite groups. Its classification as a pallasite, however, is still up for discussion. Further study of additional ungrouped iron meteorites, as well as pallasites, would provide further insight into the chemical and isotopic characteristics of the protosolar nebula, thereby widening our knowledge of the bulk planetary and nebular heterogeneity of the early solar system.

Bibliography

Allègre, C. J. and Luck, J. M. (1980). Osmium isotopes as petrogenetic and geological tracers. *Earth Planet. Sci. Lett. 48(1)*, 148–154.

Bermingham, K. R., Walker, R. J., and Worsham, E. A. (2016). Refinement of high precision Ru isotope analysis using negative thermal ionization mass spectrometry. *International Journal of Mass Spectrometry*, *403*, 15-26.

Bermingham, K. R., Worsham, E. A., & Walker, R. J. (2018). New insights into Mo and Ru isotope variation in the nebula and terrestrial planet accretionary genetics. *Earth Planet. Sci. Lett.*, ***487***, 221-229.

Birck J. L., Barman M. R. and Capmas F. (1997) Re-Os isotopic measurements at the femtomole level in natural samples. *Geostand. Newslett. 21(1),* 19–27.

Bouvier, A., Gattacceca, J., Agee, C., Grossman, J., Metzler, K. (2017). The Meteoritical Bulletin, No. 105. *Meteorit. Planet. Sci*. 1, 1-250.

Breen, J.P., Rubin, A.E., and Wasson, J.T. (2016). Variations in impact effects among IIIE iron meteorites. *Meteorit. Planet. Sci., 51(9),* 1611-1631.

Buchwald V. F. (1975). Handbook of Iron Meteorites. University of California Press, 1418 pp.

Budde G., Burkhardt C., Brennecka G.A., Fischer-Godde M., Kruijer T.S., Kleine T. (2016). Molybdenum isotopic evidence for the origin of chondrules and a distinct heritage of carbonaceous and non-carbonaceous meteorites. *Earth Planet. Sci. Lett.* 454, 293-303.

Budde, G., Burkhardt, C., Kleine, T. (2019). Molybdenum isotopic evidence for the late accretion of outer Solar System material to Earth. *Nature Astronomy* 3, 736-741.

Burbidge, E.M., Burbidge, G.R., Fowler, W.A., Hoyle, F. (1957). Synthesis of the elements in stars. *Rev. Mod. Phys*. 29, 547-650.

Burkhardt, C., Kleine, T., Oberli, F., Pack, A., Bourdon, B., and Wieler, R. (2011). Molybdenum isotope anomalies in meteorites: constraints on solar nebula evolution and origin of the Earth. *Earth Planet. Sci. Lett.*, *312*(3-4), 390-400.

Chabot, N. L. (2004). Sulfur contents of the parental metallic cores of magmatic iron meteorites. *Geochim*. *Cosmochim*. *Acta*, *68*(17), 3607-3618.

Chabot, N. L., Wollack, E. A., McDonough, W. F., Ash, R. D., & Saslow, S. A. (2017). Experimental determination of partitioning in the Fe-Ni system for applications to modeling meteoritic metals. *Meteorit. Planet. Sci*, *52*(6), 1133-1145.

Chabot, N.L., Zhang, B. (2021). A revised trap melt model for iron meteorites applied to the IIIAB group. *Meteorit. Planet. Sci., 57*, 200-227.

Chen J.H., Papanastassiou D.A., Wasserburg G.J. (2010) Ruthenium endemic isotope effects in chondrites and differentiated meteorites. *Geochim*. *Cosmochim*. *Acta* 74, 3851–3862.

Choi, B.-G., Ouyang, X., and Wasson, J. (1995). Classification and origin of IAB and IIICD iron meteorites. *Geochim. et Cosmochim. Acta*, *59,* 593-612.

Cohen A. S. and Waters F. G. (1996). Separation of osmium from geological materials by solvent extraction for analysis by thermal ionisation mass spectrometry. *Anal. Chim. Acta 332(2–3)*, 269–275.

Dauphas N., Davis A.M., Marty B., Reisberg L. (2004) The cosmic molybdenum-ruthenium isotope correlation. *Earth Planet. Sci. Lett.* 226, 465-475.

Dauphas N., Marty B., Reisberg L. (2002). Molybdenum evidence for inherited planetary scale isotope heterogeneity of the protosolar nebula. *Astrophys*. *Journ*. 565, 640-644.

Dauphas, N., and Schauble, E.A. (2016). Mass fractionation laws, mass-independent effects, and isotopic anomalies. *Annu. Rev. Earth Planet. Sci., 44,* 709-783.

Fischer-Gödde, M., Burkhardt, C., Kruijer, T. S. and Kleine, T. (2015). Ru isotope heterogeneity in the solar protoplanetary disk. *Geochim. et Cosmochim. Acta, 168*, 151–171.

Hellman, J.L., Walker, R.J. (2022), Hafnium-tungsten isotope systematics of bulk chondrites. *Lunar Planet. Sci. Conf.* LIII, 2588 (abst).

Hellmann, J.L., Kruijer, T.S., Van Orman, J.A., Metzler, K., Kleine, T. (2019). Hf-W chronology of ordinary chondrites. *Geochim. Cosmochim. Acta* 258, 290-309.

Hilton, C.D., Walker, R.J. (2019a). Chemical and isotopic compositions of the IIG iron meteorites. *Lunar Planet. Sci. Conf.* L, 1240 (abst.).

Hilton, C.D., Bermingham, K.R., Walker, R.J., McCoy, T.J. (2019b). Genetics, crystallization sequence, and age of the South Byron Trio meteorites: New insights to carbonaceous chondrite (CC) type parent bodies. *Geochim. Cosmochim. Acta* 318, 112-125.

Hilton C. D., Ash R. D. and Walker R. J. (2020) Origin of the Eagle Station Pallasites from the IIF iron meteorite core. *Meteorit. Planet. Sci*. 55, 2570–2586.

Hilton, C.D., Ash, R.D., Walker, R.J. (2022). Chemical characteristics of iron meteorite parent bodies. *Geochim. Cosmochim. Acta 318*, 112-125.

Hirschmann, M.M., Bergin, E.A., Blake, G.A., Ciesla, F.J., Li, J. (2021). Early volatile depletion on planetesimals inferred from C-S systematics of iron meteorite parent bodies. *PNAS, 118 (13).*

Horan M.F., Walker R.J., Morgan J.W., Grossman J.N., Rubin A.E. (2003). Highly

siderophile elements in chondrites. *Chem. Geol.* ***196***, 5-20.

Hunt, A.C., Ek, M., and Schönbächler, M. (2017). Separation of Platinum from Palladium and Iridium in iron meteorites and accurate high-precision determination of platinum isotopes by multi-collector ICP-MS. *Geostandards and Geoanalytical Research, 41(4),* 633-647.

Jones, J. H., & Malvin, D. J. (1990). A nonmetal interaction model for the segregation oftrace metals during solidification of Fe-Ni-S, Fe-Ni-P, and Fe-Ni-SP alloys. *Metallurgical Transactions B*, *21*(4), 697-706.

Kleine, T., Mezger, K., Münker, C., Palme, H., Bischoff, A. (2004). 182Hf–182W isotope systematics of chondrites, eucrites, and Martian meteorites: chronology of core formation and mantle differentiation in Vesta and Mars. *Geochim. Cosmochim. Acta* 68, 2935–2946.

Kleine, T., Rudge, J.F. (2011). Chronometry of meteorites and the formation of the Earth and Moon. *Elements*, 7*,* 41-46.

Kruijer, T. S., Burkhardt, C., Budde, G., and Kleine, T. (2017). Age of Jupiter inferred from the distinct genetics and formation times of meteorites. *Proceedings of the National Academy of Sciences*, 201704461.

Kruijer, T.S., Fischer-Godde, M., Kleine, T., Sprung, P., Leya, I., and Wieler, R. (2013). Neutron capture on Pt isotopes in iron meteorites and the Hf-W chronology of core formation in planetesimals. *Earth Planet. Sci. Lett., 361*, 162-172.

Kruijer, T.S., Kleine, T., Fischer-Gödde, M., Burkhardt, C., Wieler, R. (2014). Nucleosynthetic W isotope anomalies and the Hf-W chronometry of Ca-Al-rich inclusions. *Earth Planet. Sci. Lett.* 403, 317-327.

Kuva, J., Kinnunen, K.A., Pakkanen, L., Lukkari, S., Vuoriainen, S. (2017). Tomographic investigation of a complete iron meteorite. *Geological Survey of Finland (GTK).*

Lodders K., Fegley B. (1998). The Planetary Scientist's Companion. *Oxford Univ Press, New York,* 371 pp.

Lodders, K. (2003). Solar System abundances and condensation temperatures of the elements. *Ap. J.* **591**, 1220-1247.

Lovering J.F., Nichiporuk W., Chodos A. and Brown H. (1957). The distribution of gallium, germanium, cobalt, chromium, and copper in iron and stony-iron meteorites in relation to nickel content and structure. *Geochim. et Cosmochim. Acta, 11*, 263-278.

Lu, Q. and Masuda, A. (1994). The isotopic composition and atomic weight of molybdenum. *Int. J. Mass Spectrom. Ion Process*. 130, 65–72.

Ludwig, K. R. (2003). User's Manual for Isoplot 3.00. Berkeley Geochronology Center Special Publication No. 4, Berkeley, CA, 70 pp.

Malvin, D.J., Wang, D., Wasson, J.T. (1984). Chemical classification of iron meteorites - X. Multielement studies of 43 irons, resolution of group IIIE from IIIAB, and evaluation of Cu as a taxonomic parameter. *Geochim. et Cosmochim. Acta, 48*, 785-804.

Markowski, A., Leya, I., Quitte, G., Ammon, K., Halliday, A.N. and Wieler, R. (2006). Correlated helium-3 and tungsten isotopes in iron meteorites: Quantitative cosmogenic corrections and planetesimal formation times. *Earth Planet. Sci. Lett., 250,* 104-115.

McCoy, T. J., Walker, R. J., Goldstein, J. I., Yang, J., McDonough, W. F., Rumble, D., Chabot, N. L., Ash, R. D., Corrigan, C. M., Michael, J. R., Kotula, P. G. (2011). Group IVA irons: new constraints on the crystallization and cooling history of an asteroidal core with a complex history. *Geochim. et Cosmochim. Acta, 75* (22), 6821–6843.

Moore, C.B., Lewis, C.F., Nava, D. (1969). Superior Analyses of Iron Meteorites. *Meteorite Research, 738-748*

Nagai, Y. and Yokoyama, T. (2014). Chemical separation of Mo and W from terrestrial and extraterrestrial samples via anion exchange chromatography. *Analytical Chemistry, 86*, 4856-4863.

Pernicka, E. and Wasson, J.T. (1987). Ru, Re, Os, Pt and Au in iron meteorites. *Geochim. Cosmochim. Acta* 51, 1717-1726.

Poole, G. M., Rehkamper, M., Coles, B. J., Goldberg, T., & Smith, C. L. (2017). Nucleosynthetic molybdenum isotope anomalies in iron meteorites–new evidence for thermal processing of solar nebula material. *Earth Planet. Sci. Lett.*, ***473***, 215-226.

Regelous, M., Elliott, T., Coath, C.D. (2008). Nickel isotope heterogeneity in the early solar system. *Earth Planet. Sci. Lett.* 272, 330-338.

Rehkämper, M., and Halliday, A. N. (1997). Development and application of new ion-exchange techniques for the separation of the platinum group and other siderophile elements from geological samples. *Talanta*, *44*(4), 663-672.

Rusk B. (2009). Laser ablation ICP-MS in the earth sciences: Current practices and outstanding issues. *Econ. Geol. 104(4)*, 601–602.

Schaudy, R. and Wasson, J.T. (1972). The chemical classification of iron meteorites. VI. A reinvestigation of irons with Ge concentrations lower than 1 ppm. *Icarus* 17, 174-192.

Scott, E. R., and Wasson, J. T. (1973). The chemical classification of iron meteorites - VII. A reinvestigation of irons with Ge concentrations between 25 and 80 ppm. *Geochim. et Cosmochim. Acta, 37,*1957-1983.

Scott, E. R., and Wasson, J. T. (1975). Classification and properties of iron meteorites. *Reviews of Geophysics*, *13*(4), 527-546.

Scott, E.R.D. (1972). Chemical fractionation in iron meteorites and its interpretation. *Geochim. Cosmochim. Acta* 36, 1205-1236.

Scott, E.R.D. and Wasson, J.T. (1976). Chemical classification of iron meteorites-VIII. Groups IC, IIE, IIIF and 97 other irons. *Geochim. Cosmochim. Acta* 40, 103-115.

Shen, J.J., Papanastassiou, D.A., Wasserburg, G.J. (1996). Precise Re–Os determinations and systematics in iron meteorites. *Geochim. Cosmochim. Acta 60*, 2887–2900.

Smoliar, M.I, Walker, R.J., Morgan J.W. (1996). Re–Os ages of group IIA, IIIA, IVA, and IVB iron meteorites. *Science 271*, 1099–1102.

Spitzer, F., Burkhardt, C., Budde, G., Kruijer, T.S., Morbidelli, A., Kleine, T. (2020). Isotopic evolution of the inner solar system inferred from molybdenum isotopes in meteorites. *Astrophys. Journ. 898*, 10pp.

Sugiura, N., Ikeda, Y., Zashu, S., Wasson, J.T. (2000). Nitrogen-isotopic compositions of IIIE iron meteorites. *Meteorit. Planet. Sci*. 35, 749-756.

Tornabene, H.A., Hilton, C.D., Bermingham, K.R., Ash, R.D. and Walker, R.J. (2020). Genetics, age, and crystallization history of group IIC iron meteorites. *Geochim. et Cosmochim. Acta, 288,* 36-50.

Trinquier, A., Birck, J.-L., Allégre, C.J. (2007). Widespread 54Cr heterogeneity in the inner solar system. *Astrophys*. *J*. 655, 1179-1185.

Trinquier, A., Elliot, T., Ulfbeck, D., Coath, C., Krot, A.N., Bizzarro, M. (2009). Origin of nucleosynthetic isotope heterogeneity in the solar protoplanetary disk. *Science* 324, 374-376.

Vockenhuber, C., Oberli, F., Bichler, M., Ahmad, I., Quittem, G., Meier, M., Halliday, A.N., Lee, D.-C., Kutschera, W., Steier, P., Gehrke, R.J., Helmer R.G. (2004). New half-life measurement of 182Hf: Improved chronometer for the early solar system. *Physical Review Lette*rs 93, 172501-1-172501-4.

Volkening, J., Köppe, M., Heumann, K.G. (1991). Tungsten isotope ratio determinations by negative thermal ionization mass spectrometry. *Int. J. Mass Spectrom*. 107, 361–368.

Walker, R. J., McDonough, W. F., Honesto, J., Chabot, N. L., McCoy, T. J., Ash, R. D. and Bellucci, J. J. (2008). Modeling fractional crystallization of group IVB iron meteorites. *Geochim. et Cosmochim. Acta*, *72*(8), 2198-2216.

Walker, R.J. (2016). Siderophile elements in tracing planetary formation and evolution. *Geochemical Perspectives, 5(1),* 1-145.

Warren, P. H. (2011). Stable-isotopic anomalies and the accretionary assemblage of the Earth and Mars: A subordinate role for carbonaceous chondrites. *Earth Planet. Sci. Lett.*, *311*(1-2), 93-100.

Wasson, J.T. and Choe, W.-H. (2009). The IIG iron meteorites: Probable formation in the IIAB core. *Geochim. Cosmochim. Acta* 73, 4879-4890.

Wasson, J.T. and Huber, H. (2006). Compositional trends among IID irons; their possible formation from the P-rich lower magma in a two-layer core. *Geochim. Cosmochim. Acta* 70, 6153-6167.

Wasson, J.T., and Kallemeyn, G.W. (2002). The IAB iron meteorite complex: A group, five subgroups, numerous grouplets, closely related, mainly formed by crystal segregation in rapidly cooling melts. *Geochim. et Cosmochim. Acta*, *66*(13), 2445-2473.

Wasson, J.T., Huber, H., Malvin, D.J. (2007). Formation of IIAB iron meteorites. *Geochim. Cosmochim. Acta* 71, 760-781.

Wasson, J.T. (1999). Trapped melt in IIIAB irons: Solid/liquid elemental partitioning during the fractionation of the IIIAB magma. *Geochim. et Cosmochim. Acta, 63*, 2875– 2889.

Wasson, J.T., Richardson, J.W. (2001). Fractionation trends among IVA iron meteorites: Contrasts with IIIAB trends. *Geochim. et Cosmochim. Acta, 65*, 951–970.

Wasson, J.T., Wai, C.M. (1976). Explanation for the very low Ga and Ge concentration in some iron meteorite groups. *Nature, 261,* 114-116.

Wasson, J.T., Wai, C.M., and Kracher, A. (1980). Origin of iron meteorite groups IAB and IIICD. *Z. Naturforsch, 35a*, 781-795.

Wittig, N., Humayun, M., Brandon, A.D., Huang, S., Leya I. (2013). Coupled W-Os-Pt isotope systematics in IVB iron meteorites: In situ neutron dosimetry for W isotope chronology. *Earth Planet. Sci. Lett.* 361, 152-161.

Worsham, E.A., Burkhardt, C., Budde, G., Fischer-Gödde, M., Kruijer, T.S., and Kleine, T. (2019). Distinct evolution of the carbonaceous and non-carbonaceous reservoirs: insights from Ru. Mo, and W isotopes. *Earth Planet. Sci. Lett,*, *521*, 103-112.

Worsham, E.A., Walker, R.J., and Bermingham, K.R. (2016a). High-precision molybdenum isotope analysis by negative thermal ionization mass spectrometry. *Int. Journal of Mass Spectrometry*, *407*, 51-61.

Worsham, E.A., Bermingham, K.R., Walker, R.J. (2016b). Siderophile element systematics of IAB complex iron meteorites: new insights into the formation of an enigmatic group. *Geochim. Cosmochim*. *Acta* 188, 261-283.

Zhang, B., Chabot, N.L., Rubin, A.E., Humayun, M., Boesenberg, J.S., van Niekerk, D. (2022). Chemical study of group IIIF iron meteorites and the potentially related pallasites Zinder and Northwest Africa 1911. *Geochim. Cosmochim. Acta, 323,* 202-219.